Spontaneous Emission of an Atom Placed near the Aperture of a Scanning Microscope

V. V. Klimov

Lebedev Physical Institute, Russian Academy of Sciences, Leninskiǐ pr. 53, Moscow, 119991 Russia
e-mail: vklim@sci.lebedev.ru
Received August 7, 2003

Analytic expressions in the quasi-static approximation are obtained for the spontaneous decay rates of an atom placed near the circular aperture of a scanning microscope. The results obtained show not only that the spontaneous decay rates increase substantially near the aperture edge but also that the atomic decay appreciably slows down near the aperture center if the vector of dipole transition moment lies in the aperture plane. © *2003 MAIK "Nauka/Interperiodica".*

PACS numbers: 32.50.+d; 32.30.-r; 07.79.Fc; 68.37.Uv

At present, optical scanning microscopy is actively used in studying not only nanometer-sized objects but also single molecules [1–4]. Most recently, experiments aimed at revealing the effect of molecular dipole-moment orientation on the scanning microscope image of a molecule have been carried out [5–8]. The geometry of such experiments is illustrated in Fig. 1. The results obtained in the cited works are difficult to interpret, because the theory of light emission and absorption by a molecule near the scanning microscope tip is rather complicated. In this work, the problem of spontaneous emission rate is considered for an atom placed near the aperture of a scanning microscope. The atomic position and the orientation of its dipole moment are assumed to be arbitrary. The aperture is modeled by a circular hole with radius $a \ll \lambda$ (λ is the emission wavelength) in an ideally conducting screen (Fig. 2).

In the case of weak interaction of an atom or molecule with any nanoobject, the spontaneous transition rate γ can be written as [9, 10]

$$\frac{\gamma}{\gamma_0} = 1 + \frac{3}{2}\mathrm{Im}\frac{\mathbf{d}_0 \cdot \mathbf{E}^R(\mathbf{r'}, \mathbf{r'}, \omega_0)}{d_0^2 k^3}, \qquad (1)$$

where $\mathbf{E}^R(\mathbf{r'}, \mathbf{r'}, \omega_0)$ describes the reflected field of dipole $\mathbf{d}_0$ at the atomic emission frequency ω_0 in atomic position $\mathbf{r'}$ near the nanoobject and can be found from the solutions to the Maxwell equations with a dipole source, γ_0 is the decay rate in vacuum, and $k = \omega_0/c$.

For the incident plane wave, the problem of reflected field near an aperture is a classical diffraction problem, which has a relatively simple solution if the aperture is much smaller than the wavelength [11, 12]. The field structure near the aperture is quite intriguing even in this case and can be used for the control of atomic motion with a nanometric accuracy [13].

For a point source (the molecular dipole moment can be considered as a point dipole source), the problem is much more complicated. Nevertheless, for a nanoaperture, i.e., an aperture whose size is much smaller than the emission wavelength, spontaneous decay rate (1) can be represented in the form [10]

$$\left(\frac{\gamma}{\gamma_0}\right)^{\mathrm{radiative}} = \frac{|\mathbf{d}_{\mathrm{total}}|^2}{|\mathbf{d}_0|^2}, \qquad (2)$$

where $\mathbf{d}_{\mathrm{total}}$ is the total dipole moment of the system atom + nanoobject. In this case, the problem reduces to
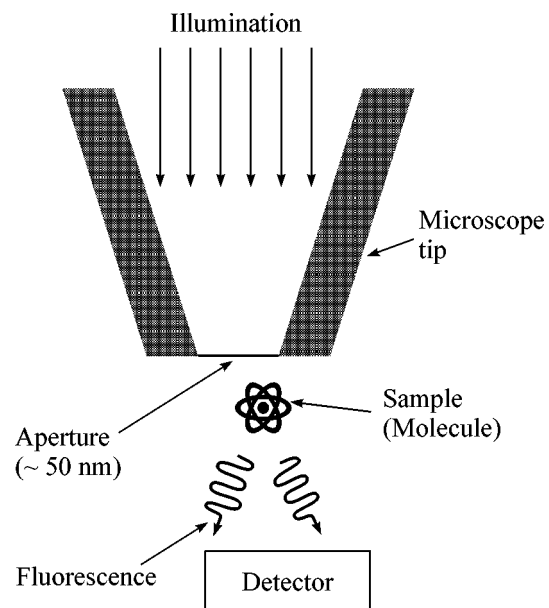

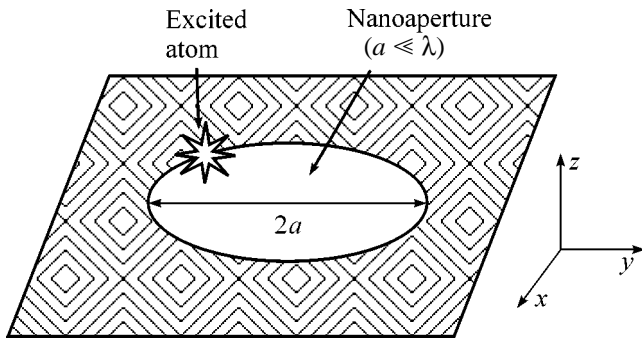**Fig. 1.** Operation of a scanning microscope with an aperture.

Fig. 2. Geometry of the problem of spontaneous atomic emission near the aperture.

the calculation of the total dipole moment of the system in the quasi-static approximation.

To find the total dipole moment of the system atom + aperture, one should solve the quasi-static problem

$$\text{curl}\mathbf{E} = 0, \quad \text{div}\mathbf{D} = 4\pi\rho, \tag{3}$$

where the dipole charge density is determined by the usual expression

$$\rho = (\mathbf{d}_0\nabla')\delta^{(3)}(\mathbf{r} - \mathbf{r}')e^{-i\omega t}. \tag{4}$$

In Eq. (4), δ is the Dirac delta function; ∇' stands for the gradient with respect to the atomic position $\mathbf{r}'$; and $\mathbf{d}_0$ is the dipole transition moment. Hereafter, the time dependence of fields will not be indicated explicitly.

By introducing the potential $\tilde{\varphi}$

$$\mathbf{E} = -\nabla(\mathbf{d}_0\nabla')\tilde{\varphi}(\mathbf{r}, \mathbf{r}'), \tag{5}$$

we obtain the usual Poisson equation

$$-\nabla^2\tilde{\varphi} = 4\pi\delta^{(3)}(\mathbf{r} - \mathbf{r}') \tag{6}$$

which should be supplemented by the condition that the potential (or the field tangential component) is zero at the screen surface.

The solution to Eq. (6) can suitably be represented in the form

$$\tilde{\varphi} = \varphi_0 + \delta\varphi, \tag{7}$$

where φ_0 is the potential of a unit charge in free space:

$$\varphi_0 = 1/|\mathbf{r} - \mathbf{r}'|. \tag{8}$$

When solving the quasi-static problem (6) and (7), it is natural to bring the symmetry axis (z axis) of the system into coincidence with the axis of the toroidal coordinate system (Fig. 2) [14]. The coordinate sur-

faces in this system ($0 \le \eta \le \infty$, $0 \le \xi \le 2\pi$, $0 \le \psi \le 2\pi$) consist of toroids ($\eta = $ const), spheres ($\xi = $ const), and planes

$$y = x\tan\psi. \tag{9}$$

The Cartesian coordinates are related to the toroidal coordinates by

$$x = a\frac{\sinh\eta}{\cosh\eta - \cos\xi}\cos\psi,$$

$$y = a\frac{\sinh\eta}{\cosh\eta - \sin\xi}\sin\psi, \tag{10}$$

$$z = a\frac{\sin\xi}{\cosh\eta - \cos\xi}.$$

The Lame coefficients of the toroidal coordinate system have the form

$$h_\xi = h_\eta = \frac{a}{\cosh\eta - \cos\xi}; \quad h_\psi = \frac{a\sinh\eta}{\cosh\eta - \cos\xi}. \tag{11}$$

The Green's function (8) of free space can be represented as

$$\varphi_0 = \frac{1}{|\mathbf{r} - \mathbf{r}'|}$$
$$= \frac{1}{a}\sqrt{\frac{(\cosh\eta - \cos\xi)(\cosh\eta' - \cos\xi')}{2(\cos\Omega - \cos(\xi - \xi'))}}, \tag{12}$$

$$\cosh\Omega = \cosh\eta\cosh\eta' - \sinh\eta\sinh\eta'\cos(\psi - \psi').$$

Expression (12) can be written in the integral form:

$$\varphi_0 = \frac{1}{|\mathbf{r} - \mathbf{r}'|}$$
$$= \frac{1}{a}\sqrt{(\cosh\eta - \cos\xi)(\cosh\eta' - \cos\xi')}I, \tag{13}$$

$$I = \int_0^\infty d\tau P_{-1/2 + i\tau}(\cosh\Omega)\frac{\cosh(\tau(\pi - |\xi - \xi'|))}{\cosh(\tau\pi)}.$$

The solution for the reflected-field potential $\delta\varphi$ is sought in the form

$$\delta\varphi = \frac{1}{a}\sqrt{(\cosh\eta - \cos\xi)(\cosh\eta' - \cos\xi')}R,$$

$$R = \int_0^\infty d\tau \frac{P_{-1/2 + i\tau}(\cosh\Omega)}{\cosh(\tau\pi)}(A_1 e^{\tau\xi} + A_2 e^{-\tau\xi}). \tag{14}$$

After finding the coefficients A_1 and A_2 from the condition that the potential at the screen surface is zero ($\xi = $

0, 2π), one obtains the following expression for the total potential (7):

$$\tilde{\varphi}(\mathbf{r}, \mathbf{r}') = \frac{1}{a}$$

$$\times \sqrt{(\cosh\eta - \cos\xi)(\cosh\eta' - \cos\xi')}(I + R),$$

$$I + R = \int_0^\infty d\tau \frac{P_{-1/2+i\tau}(\cosh\Omega)}{\cosh^2(\tau\pi)} \qquad (15)$$

$$\times \begin{cases} \sinh\tau(2\pi - \xi)\sinh\tau\xi', & \xi > \xi' \\ \sinh\tau(2\pi - \xi')\sinh\tau\xi, & \xi' > \xi. \end{cases}$$

The obtained integral representation of the solution is valid for arbitrary parameters.

To evaluate the integrals in Eq. (15), we use integral representation of the Legendre function

$$P_{-1/2+i\tau}(\cosh\Omega)$$

$$= \frac{2}{\pi}\cosh\pi\tau \int_0^\infty \frac{ds\cos\tau s}{\sqrt{2(\cosh\Omega + \cosh s)}}, \qquad (16)$$

after which the final expression for the point-charge potential in the presence of aperture in an ideally conducting plane takes the form

$$\tilde{\varphi}(\mathbf{r} - \mathbf{r}') = \frac{\sqrt{(\cosh\eta - \cos\xi)(\cosh\eta' - \cos\xi')}}{\pi a \sqrt{2}}$$

$$\times \left[\frac{\frac{\pi}{2} + \arcsin\frac{\cos((\xi - \xi')/2)}{\cosh(\Omega/2)}}{\sqrt{\cosh\Omega - \cos(\xi - \xi')}} \right.$$

$$\left. - \frac{\frac{\pi}{2} + \arcsin\frac{\cos((\xi + \xi')/2)}{\cosh(\Omega/2)}}{\sqrt{\cos\Omega - \cos(\xi + \xi')}} \right]. \qquad (17)$$

Knowing the potential in the presence of the aperture, one can determine the total dipole moment of the system and, then, using Eq. (2), obtain the expressions for the spontaneous transition rates for an arbitrary position and orientation of the dipole moment.

To find the total dipole moment of the system, one should obtain the expressions for the potential at large distances $R = \sqrt{x^2 + y^2 + z^2}$ from the nanoaperture. The corresponding asymptotic expressions are

$$\tilde{\varphi}(\mathbf{r}, \mathbf{r}') \approx \begin{cases} \dfrac{az}{\pi\sqrt{2}R^3}f^+(\xi', \eta'), & z > 0 \\[2mm] \dfrac{az}{\pi\sqrt{2}R^3}f^-(\xi', \eta'), & z < 0 \end{cases} \qquad (18)$$

where

$$f^\pm(\xi', \eta') = \pm\frac{4\sin(\xi'/2)}{\sqrt{\cosh\eta' - \cos\xi'}}$$

$$+ \frac{2\sqrt{2}\sin(\xi')(\pi/2 \pm \arcsin(\cos(\xi'/2)/\cosh(\eta'/2)))}{\cosh\eta' - \cos\xi'}. \qquad (19)$$

Expressions (18) and (19) demonstrate that the potential has the dipolar character in both upper and lower halfspaces, with only the dipole-moment z component being nonzero to a first approximation. Using Eqs. (18) and (19), one can easily find the expressions for the dipole moments responsible for the emission into the upper and lower halfspace, respectively:

$$d_{z,\text{tot}}^\pm = \frac{a}{\pi\sqrt{2}}(\mathbf{d}_0\nabla')f^\pm(\xi', \eta')$$

$$= \frac{a}{\pi\sqrt{2}}\left(\frac{d_{0,\xi'}}{h_{\xi'}}\frac{\partial}{\partial\xi'} + \frac{d_{0,\eta'}}{h_{\eta'}}\frac{\partial}{\partial\eta'}\right)f^\pm(\xi', \eta'). \qquad (20)$$

For the total spontaneous decay rate, one has

$$\frac{\gamma}{\gamma_0} = \frac{1}{2}\left(\frac{d_{z,\text{tot}}^{+2}}{d_0^2} + \frac{d_{z,\text{tot}}^{-2}}{d_0^2}\right). \qquad (21)$$

In Eq. (21), the first term allows for the emission into the upper halfspace, while the second term describes the emission into the lower halfspace. An important feature of this approximation is that the spontaneous emission is strongly suppressed for the φ-oriented dipole moment in any atomic position and is described by the terms on the order of $(ka)^2$ (magnetic dipole and quadrupole emission), i.e., by higher-order small terms than in Eq. (21). In what follows, the coordinates of atomic position will be unprimed.

Therefore, the spontaneous emission of an atom placed near the nanoaperture can be described in terms of relatively simple analytic expressions (19)–(21).

In some particular cases, expressions (19)–(21) become quite simple. For example, if the atom is situated on the axis $\rho = 0$ of the system, the emission is possible only for the z-oriented dipole moment. The corresponding total dipole moments responsible for the emission into the upper and lower halfspaces are

$$\frac{d_{\text{tot},z}^\pm}{d_0} = 1$$

$$\pm\left(\frac{2}{\pi}\arctan\left(\frac{z}{a}\right) + \frac{2az}{\pi(a^2 + z^2)}\right). \qquad (22)$$

At $z = 0$, one has $d_{\text{tot},z}^+/d_0 = d_{\text{tot},z}^-/d_0 = 1$; i.e., an atom placed in the aperture center emits as if it emit in the free space. At $z \gg a$, $d_{\text{tot},z}^+/d_0 = 2$ and $d_{\text{tot},z}^-/d_0 = 0$, so that the system emits with a doubled dipole moment into the upper halfspace. Clearly, the limit $z \gg a$ implies
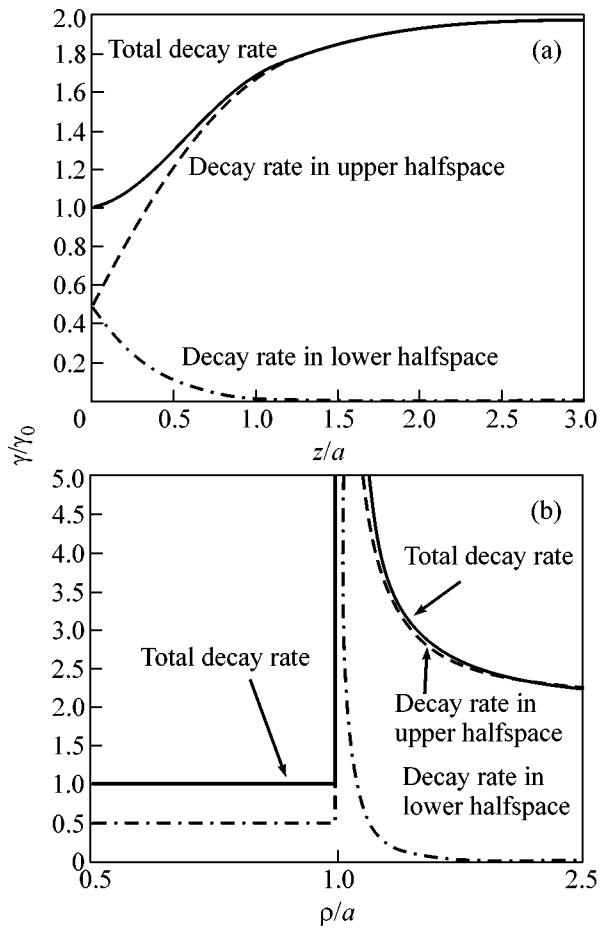
Fig. 3. Spontaneous decay rates for the z-oriented atomic dipole moment: (a) atom is on the system axis and (b) atom is in the aperture plane.
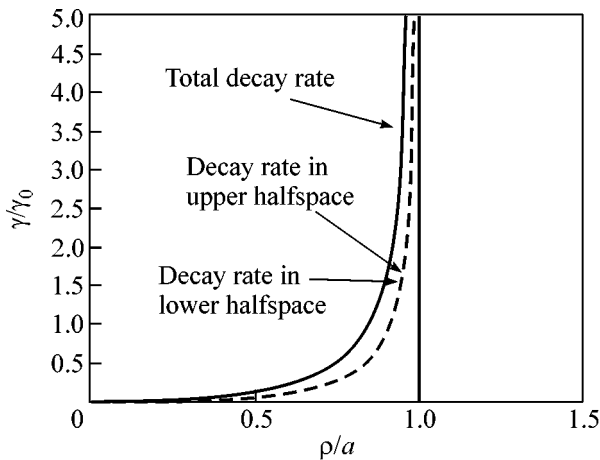

Fig. 4. Spontaneous decay rates of an atom having ρ-oriented dipole moment and placed in the aperture plane.

$\lambda \gg z \gg a$. As the distance between the atom and aperture becomes comparable with the emission wavelength, the nanoaperture ceases to influence the emission, and one should use expressions for the spontane-

ous decay rate in the presence of a plane without a hole in it [10]:

$$\frac{\gamma}{\gamma_0} = \left(1 + 3\left(\frac{\sin(2kz)}{(2kz)^3} - \frac{\cos(2kz)}{(2kz)^2}\right)\right),$$

$$\frac{z}{a} \gg 1. \tag{23}$$

In Fig. 3a, the total decay rate and the decay rates into the upper and lower halfspaces are shown for the z-oriented dipole situated on the axis.

We now consider the decay rates for an atom having a z-oriented dipole moment and placed in the $z = 0$ plane. In such a situation, the atomic decay rates in the very aperture do not change in any atomic position, as compared to the free-space case: $d_{\text{tot},z}^+/d_0 = d_{\text{tot},z}^-/d_0 = 1$. For an atom placed near the screen ($z \longrightarrow +0$, $\rho > a$), the dipole moments for the emission into the upper and lower halfspaces take the form

$$\frac{d_{\text{tot},z}^\pm}{d_0} = 1$$

$$\pm\left(\frac{a}{\sqrt{\rho^2 - a^2}} + \arcsin\frac{\sqrt{\rho^2 - a^2}}{a\rho}\right), \quad \rho > a. \tag{24}$$

In Fig. 3b, the total decay rate and the decay rates into the upper and lower halfspaces are shown for an atom having a z-oriented dipole moment and placed at any point in the $z = 0$ plane. One can see from Eq. (24) and Fig. 3b that the decay rates strongly (infinitely) increase in the vicinity of the aperture edge and that the emission propagates into both upper and lower halfspaces. If one takes into account that the thickness and conductivity of screen are finite, the spontaneous decay rate of an atom near the aperture edge also becomes finite.

As one more particular example of Eqs. (19)–(21), we consider the decay rates for an atom having ρ-oriented dipole moment and placed in the $z = 0$ plane (in our approximation, the decay rates for an atom with a φ-oriented dipole moment are equal to zero). At $\rho < a$, the dipole moments responsible for the emission into the upper and lower halfspaces are

$$\frac{d_{\text{tot},z}^\pm}{d_0} = \mp\frac{2}{\pi}\frac{\rho}{\sqrt{a^2 - \rho^2}}, \quad \rho < a. \tag{25}$$

Outside the aperture, $\rho > a$, the total dipole moment is zero because of the boundary conditions on the ideally conducting plane. In Fig. 4, the total decay rate and the decay rates into the upper and lower halfspaces are shown for an atom placed in any point of the $z = 0$ plane and having a dipole moment oriented along the radius. One can see from Eq. (25) and Fig. 4 that the decay rates strongly (infinitely) increase in the vicinity of the aperture edge and that the emission propagates into both upper and lower halfspaces. If one takes into

account that the thickness and conductivity of the screen are finite, the spontaneous decay rates of an atom near the aperture edge again become finite.

The spontaneous decay rates of an atom inside the aperture, with the dipole-moment vector lying in the aperture plane, were also considered in works [15, 16], where the corresponding rates proved to be of a higher-order smallness ($\propto(ka)^2$) than in Eq. (21). It is conceivable that the main decay channel (dipole emission with a z-oriented total dipole moment) was not taken into account in [15], while the results of [15] describe only partially the contribution of high-order multipoles (magnetic dipole and electric quadrupole) to the spontaneous decay rate.

In summary, analytic expressions allowing relatively simple estimates to be made for the spontaneous decay rates near the aperture (nanoaperture) of a scanning microscope have been derived in this work. The results can also be used to determine the atomic frequency shifts caused by the presence of a nanoaperture and to interpret the results obtained by scanning microscopes with an aperture and single molecule as an object [17].

REFERENCES

1. *Near Field Optics*, Ed. by D. W. Pohl and D. Courjon (Kluwer Academic, Dordrecht, 1992).

2. *Near Field Nano/Atom Optics and Technology*, Ed. by M. Ohtsu (Springer, Berlin, 1998).

3. J. P. Fillard, *Near Field Optics and Nanoscopy* (World Sci., Singapore, 1998).

4. *Nano-Optics*, Ed. by S. Kawata, Motoichi Ohtsu, and Masahiro Irie (Springer, Berlin, 2002).

5. H. Gersen, M. F. Garcia-Parajó, L. Novotny, *et al.*, Phys. Rev. Lett. **85**, 5312 (2000).

6. H. Gersen, M. F. Garcia-Parajó, L. Novotny, *et al.*, J. Microsc. **202**, 374 (2001).

7. J. A. Veerman, M. F. Garcia-Parajo, L. Kuipers, *et al.*, J. Microsc. **194**, 477 (1999).

8. B. Sick, B. Hecht, U. P. Wild, and L. Novotny, J. Microsc. **202**, 365 (2001).

9. R. R. Chance, A. Prock, and R. Silbey, Adv. Chem. Phys. **37**, 1 (1978).

10. V. V. Klimov, M. Ducloy, and V. S. Letokhov, Kvantovaya Élektron. (Moscow) **31**, 569 (2001); V. V. Klimov, Usp. Fiz. Nauk **173**, 1008 (2003).

11. H. A. Bethe, Phys. Rev. **66**, 163 (1944).

12. C. J. Bouwkamp, Philips Res. Rep. **5**, 401 (1950).

13. V. I. Balykin, V. V. Klimov, and V. S. Letokhov, Pis'ma Zh. Éksp. Teor. Fiz. **78**, 11 (2003) [JETP Lett. **78**, 8 (2003)].

14. G. Korn and T. Korn, *Mathematical Handbook for Scientists and Engineers*, 2nd ed. (McGraw-Hill, New York, 1968; Nauka, Moscow, 1974).

15. T. V. Plakhotnik, Opt. Spektrosk. **79**, 747 (1995) [Opt. Spectrosc. **79**, 688 (1995)].

16. P. T. Leung, Opt. Commun. **136**, 360 (1997).

17. V. V. Klimov, *Emission Properties of a Single Molecule Placed Near an Aperture of an Optical Scanning Microscope* (in press).

Translated by V. Sakun

From Dendrites and S-Shaped Growth Curves to the Maximum Entropy Production Principle[¶]

L. M. Martyushev* and E. G. Axelrod

Institute of Industrial Ecology, Russian Academy of Sciences, Yekaterinburg, 620219 Russia
**e-mail: mlm@ecko.uran.ru*

S-shaped kinetic curves are very frequent in nature. Based on our own experimental evidence on the growth of single dendrites and analysis of literature data, we have demonstrated that such curves may result from the maximum entropy production principle. The proposed approach also explains other prevalent laws of relaxation in nonequilibrium systems (exponential, Kohlrausch, etc.). © 2003 MAIK "Nauka/Interperiodica".

PACS numbers: 68.70.+w; 81.10.Aj; 05.65.+b

The dendrite growth is a typical example of self-organization. It occurs both in animate (e.g., trees) and inanimate nature (e.g., snowflakes) [1–3]. The shape similarity of such different objects may suggest certain laws common to their evolution. Indeed, dendrites are formed in a nonequilibrium environment with relatively large gradients of concentrations, temperature, sunlight, etc. Therefore, some protuberances (formed, e.g., by chance) may grow faster in this inhomogeneous medium, and a treelike structure appears [1–3]. One more startling similarity is true of the nonequilibrium evolution. This is the resemblance of sigmoidal kinetic growth curves (S-shaped growth curves). However, this issue has received little attention. This question and its consequences are considered in the present paper.

Crystallization of ammonium chloride (NH_4Cl) from an aqueous solution was studied. The experimental conditions were considerably nonequilibrium: a solution saturated at 30–40°C was cooled down quickly to 10–20°C to form dendrites (Fig. 1). They were grown in quasi-two-dimensional conditions (a flat capillary whose thickness was much smaller than the diffusion length ~400 μm was used) [4]. Consequently, the mass of the growing dendrite changed in proportion to its surface area in the plane of the experimental cell. A microscope with a photometry sensor built into the eyeglass was used. The integral light flux penetrating through the sample and hitting the photodetector was proportional to the surface area ratio of the solution and the crystal. The sensor signal was registered in the digital format (sampling frequency was 1 kHz). The mass was measured on a freely growing dendrite spaced at least as far as the diffusion length from neighboring dendrites. Other experimental details have been published elsewhere [5, 6].

The time-mass dependence had a specific S-shape at all the supersaturations and saturation temperatures (Fig. 2). The growth time only changed from several tens of seconds to several minutes. Measurements were performed on over fifty growing crystals. The normal-
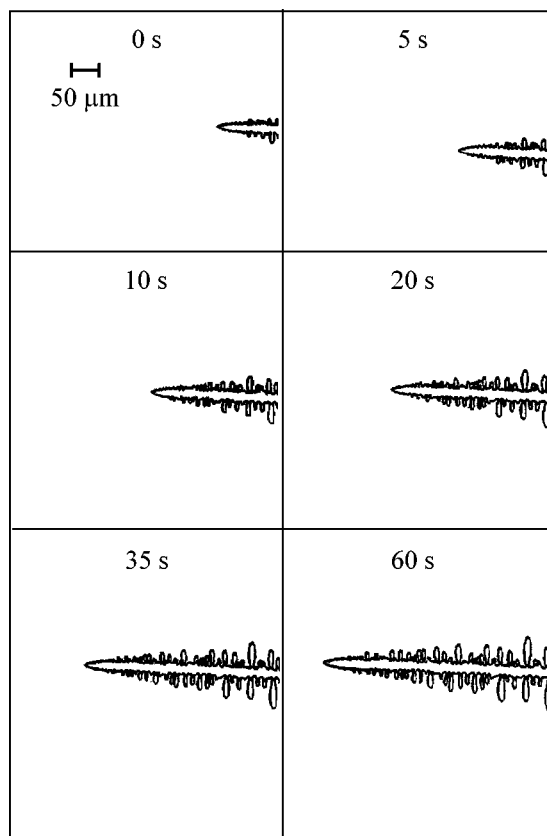

Fig. 1. Growth of an NH_4Cl dendrite from an aqueous solution with time.

[¶] This article was submitted by the authors in English.

ized data was subject to a regression analysis by the Levenberg–Marquardt method [7, 8] using CurveExpert statistical software. A feature of the software was a large number of nonlinear regression models, which are most commonly used in applications. The aim of the analysis was to determine equations best fitting the data (the standard error of the estimate (E) and correlation coefficient (R) served as the "goodness of fit" [7, 8]). According to the calculations, the degree of supersaturation and saturation temperatures did not influence (within the experimental error) the regression models and their parameters. Therefore, all the data were integrated into one sample whose analysis yielded the following results.

The best fits (from the aforementioned criterion) provided were the Weibull model $M(t) = a - b\exp(-ct^d)$ scoring 86 points (inset of Fig. 2 is an additional argument for this model), the Richards model $M(t) = a/(1 + \exp(b - ct))^{1/d}$ scoring 122 points, and the MMF model $M(t) = (ab + ct^d)/(b + t^d)$ scoring 133 points. Some additional comments are necessary: (1) models having not more than four parameters (a, b, c, and d) were selected; (2) the points were equal to the sum of places (the place is higher if E is less and R is more) taken by a model fitting each experimental curve. This classification is very arbitrary and may provoke objections. Indeed, the correlation coefficients of the given models generally differ little (e.g., 0.993 and 0.994). With such "difference," the physical interpretation of each model is most important. In this case, the Weibull model is well grounded theoretically as will be shown below.

The calculated Weibull model parameters were $a = 1.01 \pm 0.02$, $b = 1.00 \pm 0.02$, $c = 0.003 \pm 0.001$, and $d = 2.0 \pm 0.1$. Then, the normalized experimental kinetic curves (see Fig. 2) fit the model $M(t) = 1 - \exp(-ct^2)$ (the relative error of c is over 30%, and this value is not substituted to the formula). Thanks to a greater body of data and a larger sampling frequency of signal digitizing, these data considerably refine those obtained earlier [5, 6].

The computed regression model agrees to within the denotation with the equation in the Kolmogorov–Avrami theory (KAT) for the time variation of the solid phase volume during mass crystallization [9–11]. This fact allows hypothesizing the applicability of this phenomenological stochastic–geometrical theory (used only in studies of mass crystallization of metals, polymers, etc. [9–11]) to describe of the growth of single dendrites. Indeed, a particular case of this theory is the uniform nucleation of new phase nuclei in time and space, when the growth of each nucleus is diffusion limited (its linear size increase proportionally to the square root of time) [10]. Such nuclei may be secondary branches formed during the dendrite growth. These branches appear regularly on a growing primary branch, and their growth is diffusion limited [1, 4]. They ("nuclei") are nearly ellipsoidal in shape. According to KAT, at this two-dimensional growth, d must be
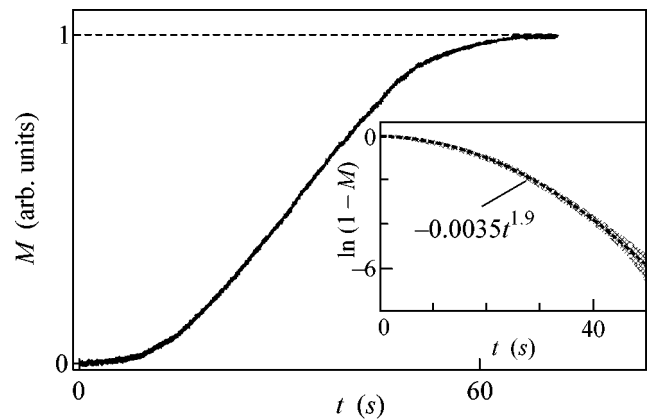

Fig. 2. Typical experimental S-shaped kinetic curve: dendrite mass (M) vs. time (t). In the inset, gray curve represents $\ln(1 - M)$ vs. time; the broken curve is their fit using the power function.

equal to two [10], which agrees fairly well with the experimental d value. In terms of KAT, it is possible to explain the dispersion of c values observed in experiments. This parameter (unlike d, which is controlled by the growth morphology) depends primarily on the occurrence rate of new nuclei and is very sensitive both to the growth time and initial conditions. Therefore, the correct determination of c calls for additional experiments with another experimental setup.

The modified KAT substantiates the choice of the Weibull model for fitting. This model should be preferred for one more important reason. Let us make two comments first.

(1) The growth rate passes a maximum and approaches zero asymptotically during mass crystallization because crystals gradually fill all the vacant volume (adjacent nuclei collide and stop growing in the collision direction). This interpretation is incorrect for dendrite growth, which is decelerated due to the disappearance of solution supersaturation around a dendrite (the solution areas around dendrite branches "collide").

(2) $M(t)$ is the fraction of the solid phase during mass crystallization. Since nucleation sites are random, $M(t)$ may be taken as the probability that a random site crystallizes by the time t. In case of the dendrite growth, the whole area is divided into two parts: (1) a crystal and a saturated (equilibrium) solution and (2) a supersaturated solution. These parts do not have a well-defined boundary. However, one may unambiguously distinguish the areas and watch their transition with time by setting a priori a concentration threshold slightly above the equilibrium. From the above reasoning, $M(t)$ may also be related to some area where supersaturation is removed and the chemical potential is nearly the same. Therefore, fraction $M(t)$ may be viewed (similarly to mass crystallization) as the probability of a transition at a random space site by the time

t (the probability that the chemical potential of the site is equal to chemical potential of the dendrite crystal).

With this in mind, discuss Fig. 2 again. Consider a random solution site. Let the time T of the transition at this site be a random variable. Then, the probability that the transition occurs in a time T less than t equals $M(t)$ (which may be considered as a cumulative distribution function). Therefore, T obeys the Weibull distribution (since $d = 2$, it is also called the Rayleigh distribution) [12]. On the other hand, the mathematical statistics [13, 14] suggests that minimums of random and bounded below variable have this distribution, i.e., if $T = \min\{T_1, T_2, \ldots, T_n\}$ and $n \longrightarrow \infty$ ($T_1, \ldots, T_n$ being identically distributed random variables equal to zero or larger), T will obey the Weibull distribution function. Therefore, one may hypothesize that the transition occurs in a minimum possible time or, in other words, mass or dendrite crystallization is realized at a maximum possible rate.

As is known, the crystallization rate is directly proportional to the entropy production in a system [15, 16]. This brings us to a notion known as the maximum entropy production principle (MEPP) [17–24]. It is used sometimes as the basis of the entire nonequilibrium thermodynamics (specifically, Prigogine's principle [15] was shown to be its corollary) [17, 18]. MEPP is widely used in natural sciences [17–20, 23], including crystallization [21–24]. However, earlier this principle was used theoretically and verified experimentally only in selection of solutions at bifurcation points (e.g., structures with a maximum rate (entropy production) were observed during nonequilibrium crystallization after morphological transitions) [19–24]. The foregoing suggests that the principle also holds for growth without sharp nonequilibrium transitions. A limitation of the proposed approach, as compared to KAT, is the impossibility to predict distribution parameters numerically. However, this problem is typical of every general theory (e.g., thermodynamics).

Our approach, which relates S-shaped growth curves, distribution of extreme values and MEPP, provides a unified viewpoint on numerous data about nonequilibrium kinetics and relaxation. Let us dwell on two points only.

(1) S-shaped kinetic growth curves are observed in chemistry (the mass of reaction products vs. time) [25] and biology (number of bacteria and organism weight vs. time) [26, 27]. Although such curves have particular explanations, they may result from MEPP too, especially if arguments are controversial. For example, S-shaped empirical kinetic curves in biology are frequently described by the logistic model (Richards model with $a = d = 1$) [27]. However, this approach does not have solid theoretical grounds and has come under a storm of criticism [27]. Certainly, kinetic curves may be other than S-shaped (e.g., oscillation chemical reactions) [15]. This fact does not disprove our approach or MEPP. Several simultaneous processes (each following MEPP) mutually interact and, therefore, kinetic curves change their shape [18].

(2) Various relaxation phenomena in physics are considered using the exponential ($\sim\exp(-ct)$) and Kohlrausch ($\sim\exp(-ct^d)$) laws [28, 29]. These laws of the time perturbation dissipation are related to various physical mechanisms and are described by different models. However, they may also be viewed as the manifestation of a general law, namely MEPP. Indeed, relaxation may be considered either as disappearance of some parameter or its replacement by another parameter. In the latter case, normalized relaxation laws are $(1 - \exp(-ct))$ and $(1 - \exp(-ct^d))$, respectively. Consequently, the perturbation evolution laws follow the Weibull distribution and, therefore, may be considered as the MEPP corollary in the context of our approach.

In conclusion, we shall emphasize that the proposed approach should not be considered as an antithesis to existing theories. Our approach provides a unified MEPP interpretation of many nonequilibrium natural phenomena (in turn, they can be viewed as indirect confirmation of MEPP).

REFERENCES

1. J. S. Langer, Rev. Mod. Phys. **52**, 1 (1980).
2. E. Ben-Jacob, Contemp. Phys. **34**, 247 (1993).
3. J. Feder, *Fractals* (Plenum, New York, 1988; Mir, Moscow, 1991).
4. T. Sawada, K. Takemura, K. Shigematsu, *et al.*, J. Cryst. Growth **191**, 225 (1998).
5. E. G. Aksel'rod, L. M. Martyushev, and E. V. Levkina, Tech. Phys. Lett. **25**, 830 (1999).
6. E. G. Axelrod, L. M. Martiouchev, and Y. V. Lyovkina, Phys. Status Solidi A **182**, 687 (2000).
7. P. R. Bevington, *Data Reduction and Error Analysis for the Physical Sciences* (McGray-Hill, New York, 1969).
8. W. H. Press *et al.*, in *Numerical Recipes in C; The Art of Scientific Computing* (Cambridge Univ. Press, Cambridge, 1992).
9. V. Z. Belen'kii, *Geometric and Probabilistic Models of a Crystallization. Phenomenological Approach* (Nauka, Moscow, 1980).
10. L. Mandelkem, *Crystallization of Polymers* (McGray-Hill, New York, 1964).
11. J. W. Christian, in *Physical Metallurgy*, Ed. by R. W. Cahn (North-Holland, Amsterdam, 1965; Mir, Moscow, 1968).
12. G. J. Hahn and S. S. Shapiro, *Statistical Models in Engineering* (Wiley, New York, 1967).
13. E. J. Gumbel, *Statistics of Extremes* (Columbia Univ. Press, New York, 1962; Mir, Moscow, 1965).
14. M. R. Leadbetter, G. Lindgren, and H. Rootzen, *Extremes and Related Properties of Random Sequences and Processes* (Springer, New York, 1987).
15. I. Prigogine, *Introduction to Thermodynamics of Irreversible Processes*, 3rd ed. (Interscience, New York, 1968; Inostrannaya Literatura, Moscow, 1961).

16. B. Y. Lubov, *Theory of Crystallization in Large Volumes* (Nauka, Moscow, 1975).

17. H. Ziegler, *Some Extremum Principles in Irreversible Thermodynamics with Application to Continuum Mechanics* (North-Holland, New York, 1963; Mir, Moscow, 1966), Prog. Solid Mech., Vol. 4.

18. H. Ziegler, *An Introduction to Thermomechanics* (North-Holland, Amsterdam, 1983).

19. Y. A. Sawada, J. Stat. Phys. **34**, 1039 (1984).

20. G. W. Paltridge, Nature **279**, 630 (1979).

21. E. Ben-Jacob and P. Garik, Nature **343**, 523 (1990).

22. A. Hill, Nature **348**, 426 (1990).

23. L. M. Martiouchev and V. D. Seleznev, Dokl. Phys. **45**, 129 (2000).

24. L. M. Martiouchev, V. D. Seleznev, and I. E. Kuznetsova, JETP **91**, 132 (2000).

25. N. M. Emanuel and D. F. Knorre, *Chemical Kinetics; Homogeneous Reactions*, 2nd ed. (Visshaya Shkola, Moscow, 1984; Wiley, New York, 1973).

26. N. S. Pechurkin and L. A. Terskov, *Analysis of Growth Kinetics and Evolution of Microbe Populations* (Nauka, Novosibirsk, 1975).

27. W. Feller, *An Introduction to Probability Theory and Its Application*, 4th ed. (Wiley, New York, 1971; Mir, Moscow, 1964), Vol. 2.

28. L. D. Landau and E. M. Lifshitz, *Course of Theoretical Physics*, Vol. 5: *Statistical Physics*, 4th ed. (Nauka, Moscow, 1995; Pergamon Press, Oxford, 1980).

29. M. F. Shlesinger and J. Klafter, in *Fractals in Physics*, Ed. by L. Pietronero and E. Tosatti (North-Holland, Amsterdam, 1986; Mir, Moscow, 1988).

Magnetization Stochastic Dynamics in Exchange-Coupled Layered Structure

A. M. Shutyĭ and D. I. Sementsov

Ulyanovsk State University, ul. L'va Tolstogo 42, Ulyanovsk, 432700 Russia

Received August 25, 2003

The stochastic and self-oscillation regimes established under the action of a longitudinal high-frequency magnetic field in a multilayer magnetic structure with antiferromagnetic exchange coupling are considered. A bifurcation diagram revealing the types of magnetization dynamic states is constructed in various frequency intervals. Poincaré diagrams are constructed for the stochastic regimes. © *2003 MAIK "Nauka/Interperiodica".*

PACS numbers: 75.70.Cn

1. In many cases, the stability and attainable amplitudes of magnetic oscillations, as well as the presence of static and dynamic magnetic states in a magnetic subsystem play the decisive role in the practical use of magnetically coupled multilayer structures [1–3]. The magnetization self-organization processes induced by external fields in such structures are also significant, because these structures serve as good objects for studying various nonlinear dynamic regimes, stochastic oscillations, and synergistic processes. However, the available works, as a rule, deal with overly simplified models [4, 5], so that the nonlinear dynamics of real structures are not always reflected adequately. In this work, the stochastic oscillations of magnetic moments and the conditions for appearance of self-oscillation regimes in the exchange-coupled film nanostructures are investigated. Their static and dynamic properties are greatly determined by the coupling character between neighboring layers. This coupling is due to a strong indirect exchange interaction and, depending on the thickness of a nonmagnetic spacer, can give rise to the ferromagnetic, antiferromagnetic, or noncollinear ordering of magnetic moments in the neighboring layers [6, 7]. The possibility to implement a variety of equilibrium states and nonlinear dynamic regimes renders the antiferromagnetic coupling type most preferential, and it will be discussed in this work.

2. Consider the structure consisting of a sufficiently large number ($n \gg 1$) of identical magnetic metal layers separated by the spacers that provide the antiferromagnetic type of initial magnetic-moment ordering for the nearest-neighboring layers. In this case, all magnetic layers are divided into two subsystems ($j = 1, 2$) with identical behavior of magnetic moments in the layers of each subsystem. In accordance with the experimental data on the structures of this type [8], we assume that the layer magnetic anisotropy is combined from the uniaxial induced anisotropy of the easy axis type and the crystallographic cubic anisotropy, with the crystallographic [100] and [010] axes lying in the layer planes and the easy magnetic axis of induced anisotropy being oriented perpendicular to the layers. In this case, the free energy per unit area of the system is given by the expression

$$
E = d\frac{n}{2} \sum_{j=1,2} \left[-\mathbf{H}\mathbf{M}_j + \frac{K_1}{4}(\sin^2 2\psi_j + \cos^4\psi_j \sin^2 2\varphi_j) \right.
$$
$$
\left. + (K_u - 2\pi M^2)\cos^2\psi_j \right] + Jn\frac{\mathbf{M}_1\mathbf{M}_2}{M^2}, \tag{1}
$$

where d is the thickness of magnetic layers; $\mathbf{M}_j$ is the magnetization of the layers in the jth subsystem; J is the bilinear exchange-coupling constant between the magnetic moments of the nearest-neighboring layers, which depends, in the general case, on the thickness, type of material, and the structural properties of the spacers; K_1 and K_u are the constants of cubic and growth anisotropy, respectively; $\mathbf{H}$ is the static magnetizing field; φ_j is the azimuthal angle measured from the [100] axis and determining the in-plane orientation of magnetic moment; and ψ_j is the angle of $\mathbf{M}_j$ departure from the film plane. Taking into account that the demagnetizing fields are high ($4\pi M \gg 2K_u/M, JM$) in the structures with metallic magnetic layers, the magnetic moments in the case of in-plane magnetizing field $\mathbf{H}$ lie in the layer planes, so that the equilibrium angles $\psi_{0j} = 0$. To determine the equilibrium azimuthal angles $\varphi_{0j}(H)$, we

use the equilibrium condition $\partial E/\partial \varphi_j = 0$, $\partial^2 E/\partial \varphi_j^2 > 0$ and Eq. (1) to obtain the system of equations

$$2HM\sin(\varphi_{0j} - \varphi_H) + K_1\sin 4\varphi_{0j}$$
$$- 2\bar{J}\sin(\varphi_{0j} - \varphi_{03-j}) = 0,$$
$$HM\cos(\varphi_{0j} - \varphi_H) + 2K_1\cos 4\varphi_{0j}$$
$$- \bar{J}\cos(\varphi_{0j} - \varphi_{03-j}) > 0,$$

(2)

where the angle φ_H is measured from the [100] axis and determines the **H** field direction, and $\bar{J} = 2J/d$.

The equations of motion for the magnetization vectors of each layer in the spherical coordinate system is written as

$$\dot{\varphi}_j Md\cos\psi_j = \gamma\frac{\partial E}{\partial \psi_j} + \frac{\lambda}{M}\frac{1}{\cos\psi_j}\frac{\partial E}{\partial \varphi_j},$$
$$\dot{\psi}_j Md = \frac{\lambda}{M}\frac{\partial E}{\partial \psi_j} - \gamma\frac{1}{\cos\psi_j}\frac{\partial E}{\partial \varphi_j},$$

(3)

where γ is the gyromagnetic ratio and λ are the damping parameters. In our numerical analysis, we will use the parameters corresponding to the parameters of a real (Fe/Cr)$_n$ structure. For the iron layers, the magnetization $M = 1620$ G; the anisotropy parameters $K_1 = 4.6 \times 10^5$ erg/cm^3, $K_2 = 1.5 \times 10^5$ erg/cm^3, and $K_u = 2.06 \times 10^6$ erg/cm^3; the thickness $d = 21.2 \times 10^{-8}$ cm; $\lambda = 5 \times 10^7$ s^{-1}; and $\gamma = 1.76 \times 10^7$ (Oe s)$^{-1}$; although the chromium parameters do not enter explicitly in Eq. (1), they determine the coupling constant J [9]. In the films under study, the oscillation amplitude of the polar angle is always much smaller than for the azimuthal angle.

3. Analysis of equilibrium condition (2) shows that a change in the magnitude of the magnetizing field in the systems considered is accompanied by orientational hysteresis loops and attendant bistability states. In Fig. 1, field dependences of the equilibrium azimuthal angles of magnetic moments of the first (solid curves) and second (dashed curves) subsystems are shown for the coupling constants $J = 0.1$, 0.17, and 0.24 erg/cm^2 (curves *1–3*). In the case of initial orientations $\varphi_{0j} = \pm\pi/2$ and $\varphi_H = 0$, the equilibrium orientation of magnetic moments of the neighboring layers in the interval $0 < H \leq H_a$ is noncollinear. With an increase in field, the angle $\Delta\varphi_0 = \varphi_{01} - \varphi_{02}$ between the magnetization vectors of the neighboring films decreases. As the field achieves the critical value H_a, this angle achieves its minimal value

$$\Delta\varphi_0 = 2\varphi_a = 2\arccos\sqrt{\frac{\bar{J} + K_1}{6K_1}},$$

(4)

which decreases with increasing coupling constant, whereupon phase transition occurs to establish a collinear magnetic-moment orientation that is aligned with the field. As the magnetizing field decreases from the
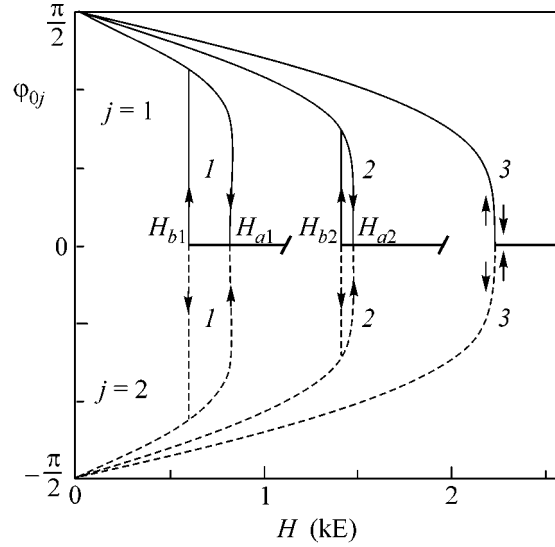

Fig. 1. Field dependences of the equilibrium azimuthal angles of magnetic moment obtained for the structures with $J = 0.1$, 0.17, and 0.24 erg/cm^2 (curves *1*, *2*, and *3*, respectively).

values $H > H_a$, the state with the co-directed orientation of the film magnetic moments is retained down to the field H_b. At $H = H_b$, the reverse phase transition occurs, which is accompanied by the orientational misalignment of the vectors **M**$_1$ and **M**$_2$ and the jumpwise achievement of angles $\varphi_{01}(H_b) = -\varphi_{02}(H_b)$. On further decrease in the demagnetizing field, the angle between the magnetizations increases smoothly, and again becomes equal to π at $H = 0$. Therefore, at small coupling constants, the boundaries of the orientational hysteresis loop are

$$H_a = \frac{4}{3M}\sqrt{\frac{\bar{J} + K_1}{6K_1}}(\bar{J} + K_1), \quad H_b = \frac{2}{M}(\bar{J} - K_1). \quad (5)$$

With an increase in the coupling constant, the hysteresis loop narrows to disappear at $J \geq J_{ab}$, where J_{ab} is determined from the equality $H_b = H_a$.

4. For the implementation of various dynamic regimes, the systems with narrow hysteresis loops are of special interest. At fields H corresponding to the middle of the hysteresis loop, various high-amplitude self-oscillation and stochastic regimes are induced by a longitudinal high-frequency field (**h** ∥ **H**) with an amplitude close to the loop width ($h \geq H_a - H_b$) in the layered system of magnetic moments. The most complete pattern of dynamic regimes in the structure considered can be obtained over a broad frequency range from the bifurcation diagram. For the exchange-coupling constant $J = 0.24$ erg/cm^2 (close to $J_{ab} \approx 0.244$ erg/cm^2), the magnetizing field $H = 2227.4$ Oe, the microwave amplitude $h = 0.2$ Oe ($H_a - H_b \approx 0.144$ Oe), and zero initial azimuthal angles of magnetic moments,
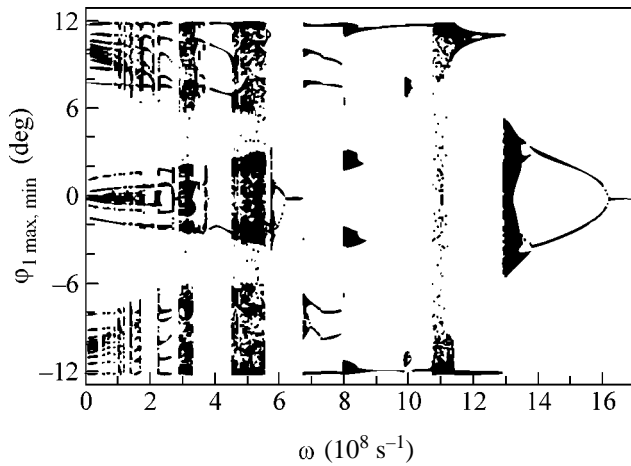
Fig. 2. Bifurcation diagram of the frequency-dependent maximal and minimal angles φ_1, as obtained for the structure with a narrow hysteresis loop ($H_a - H_b \approx 0.144$ Oe), $J = 0.24$ erg/cm^2, $H = 2227.4$ Oe, and $h = 0.2$ Oe.

the bifurcation diagram is shown in Fig. 2, where the microwave frequency is laid off as abscissa and the maximal and minimal angles of the magnetic moment of one of the layer subsystems are laid off as ordinate. The magnetic-moment oscillations of both subsystems are always in antiphase, and the equality $\varphi_2(t) = -\varphi_1(t)$ is fulfilled with a high accuracy in both regular and stochastic regimes.

Zero point on the ordinate axis is the only point where the oscillations are absent; two points correspond to the oscillation regime with one maximum and one minimum; a larger denumerable set of points corresponds to a more complex oscillation; and the set of closely spaced points correspond to the stochastic magnetic-moment dynamics. One can see in Fig. 2 that, upon changing the microwave frequency, one of the regular oscillation regimes, as a rule, transforms into the other after passing through the frequency intervals corresponding to the stochastic dynamics. Both symmetric and asymmetric regular regimes are present. When tracing the diagram from the high-frequency side, one can see that the system is initially insensitive to the action of a microwave field. Then, after the Hopf bifurcation [10], a limit cycle arises with the amplitude increasing as the frequency decreases. Next, after the period-doubling cascade, the system arrives at the stochastic behavior. As the amplitude of stochastic oscillations becomes sufficiently large, the magnetic moments appear in the attraction zone of an attractor representing a high-amplitude limit cycle. This results in new bifurcation with establishing the self-oscillation regime.

High-amplitude oscillations can be established at high frequencies as well, but only after changing the initial orientations of magnetic moments. In other words, dynamic bistability occurs in some frequency interval. The amplitude in the self-oscillation regime
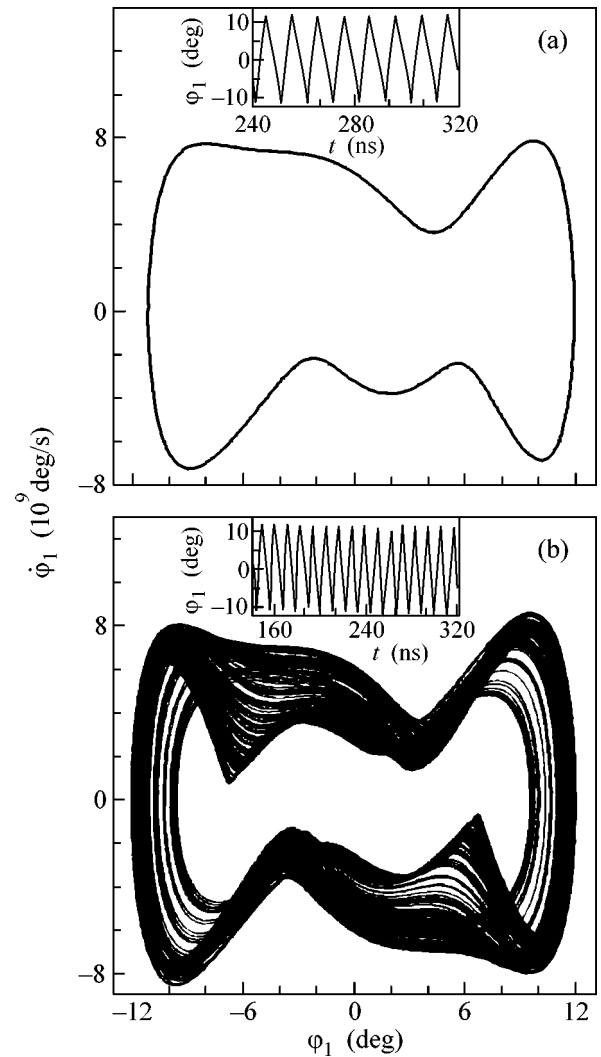

Fig. 3. Phase trajectories in the (a) regular and stochastic and (b) dynamic regimes. Insets: $\varphi_1(t)$ curves.

shows weak frequency dependence and is invariably much larger than the difference between the angles of magnetic moments in the hysteresis loop ($\varphi_a \approx 6°$). The oscillation amplitude depends on h, though weakly. For instance, as h increases fivefold, the amplitude of angle φ_1 increases only by one third.

With a decrease in frequency, the regular oscillations again become stochastic. In Fig. 3, the phase portraits of magnetic-moment dynamics of the first layer are shown for the microwave frequencies $\omega = $ (a) 12.5 and (b) 11.3×10^8 s^{-1} corresponding to the regular and stochastic dynamics, respectively. The corresponding time dependences of $\varphi_1(t)$ are shown in the insets. Near the frequencies corresponding to the regular dynamics, the oscillation amplitude is confined in a certain angular interval, as a result of which the boundary of the cycle phase trajectory spreads out. On further decrease in microwave frequency, the stochasticity becomes

more pronounced and the oscillation attractor is thickened. At frequency $\omega = 11 \times 10^8$ s^{-1}, the attractor covers the entire range of angular oscillations of magnetic moment, and the stochastic regime has a laminar phase alternating with the splashes of turbulence [11] and oscillation amplitudes characterized by a certain angular scatter. Strange attractor (b) corresponds to the stochastic dynamics and has the sections of strong contraction or folding and the expansion sections. Because of this, the phase trajectories are sensitive to the initial conditions. The separation between two closely spaced phase trajectories first increases following, on average, the exponential low $\delta = \delta_0 \exp(\zeta t)$, where ζ is the largest Lyapunov coefficient (equal to the slope of the curve approximating the divergence of phase trajectories). Numerical analysis showed that $\zeta \approx 6.2 \times 10^7$ s^{-1} for the case in hand. After the divergence achieves the attractor scale, the separation between phase trajectories starts to oscillate about the value determined by the attractor size.

For clarity, the complex phase trajectories can suitably be represented as a set of points calculated at time intervals equal to the period of the microwave field (in the case of many regular oscillations, this results in the Poincaré diagram). In Fig. 4, a discrete-time representation of the phase portraits of magnetic-moment dynamics is shown on the $(\varphi_1, \dot{\varphi}_1)$ plane for the microwave frequencies $\omega =$ (a) 13.1, (b) 8.2, and (c) 5.0 $\times$ 10^8 s^{-1}; the corresponding $\varphi_1(t)$ curves are shown in the insets. In the case (a), the stochastic dynamics developed as a result of the period-doubling cascade and after the reverse cascade [11] corresponding to the coalescence of the noiselike intervals of angle φ_1; for this reason, the stochasticity in this case covers the entire angular range of magnetic-moment oscillations. As for case (b), the stochasticity appears only for a certain angle of magnetic moment. The dynamic regime (c) near the frequency $\omega = 5.0 \times 10^8$ s^{-1} appears through the alternation, although the laminar phases (high-amplitude angular oscillations either in the positive or negative halfplane) have only few periods. The phase portrait of this regime represents the combination of two funnel-shaped attractors, with the transitions between them occurring at small azimuthal angles. The Lyapunov coefficients corresponding to the stochastic regimes (a), (b), and (c) are $\zeta \approx$ (a) 1.6, (b) 0.8, and (c) 1.2×10^8 s^{-1}.

In the low-frequency range $\omega \sim 10^7$ s^{-1} (Fig. 2), the regular dynamic regimes are characterized by the presence of time intervals on which the angle is zero and fast oscillations occur due to the magnetization reversal. The asymmetric regimes with the oscillation period equal to the microwave period occur at some frequencies, and the symmetric regimes with the alternating sign of high-amplitude angular oscillations of magnetic moment and, hence, with a doubled period, occur at the other frequencies.
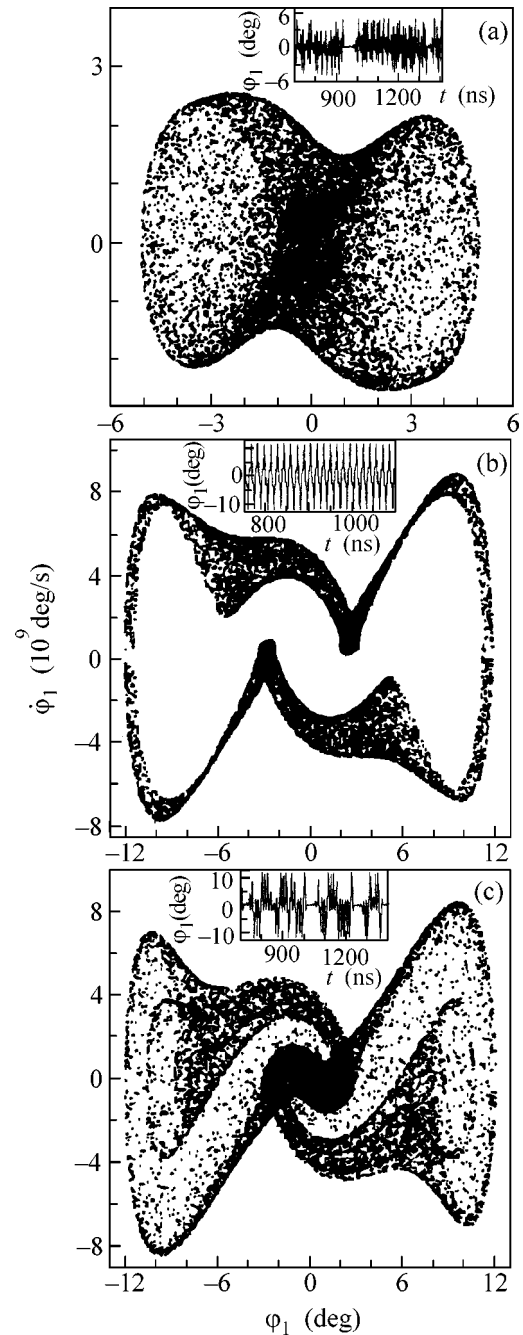

Fig. 4. Discrete-time (with step $\Delta t = 2\pi/\omega$) representation obtained for the phase trajectories of magnetic moment at $\omega =$ (a) 13.1, (b) 8.2, and (c) 5.0 $\times 10^8$ s^{-1}. Insets: $\varphi_1(t)$ curves.

It follows from the above analysis that, depending on the parameters of the magnetic subsystem, the magnitude of magnetizing field, and the frequency of a longitudinal variable magnetic field, various types of stochasticity and high-amplitude regimes are established under the action of the variable field on the structure with the type of antiferromagnetic coupling considered in this work. The diversity of possible dynamic regimes

renders such systems quite valuable for the practical use and experimental study of nonlinear oscillations.

REFERENCES

1. V. V. Ustinov, M. M. Kirilova, I. V. Lobov, *et al.*, Zh. Éksp. Teor. Fiz. **109**, 477 (1996) [JETP **82**, 253 (1996)].

2. V. V. Kostyuchenko and A. K. Zvezdin, Phys. Rev. B **57**, 5951 (1998).

3. D. I. Sementsov and A. M. Shutyĭ, Pis'ma Zh. Éksp. Teor. Fiz. **75**, 287 (2002) [JETP Lett. **75**, 242 (2002)].

4. F. V. Lisovskiĭ and O. P. Polyakov, Pis'ma Zh. Éksp. Teor. Fiz. **68**, 643 (1998) [JETP Lett. **68**, 679 (1998)].

5. F. V. Lisovskiĭ and O. P. Polyakov, Pis'ma Zh. Éksp. Teor. Fiz. **73**, 546 (2001) [JETP Lett. **73**, 483 (2001)].

6. A. Scheyer, J. F. Ankner, Th. Zeidder, *et al.*, Phys. Rev. B **52**, 16066 (1995).

7. G. S. Patrin, N. V. Volkov, and V. P. Kononov, Pis'ma Zh. Éksp. Teor. Fiz. **68**, 287 (1998) [JETP Lett. **68**, 307 (1998)].

8. M. A. Milyaev, L. N. Romashev, V. V. Ustinov, *et al.*, in *Abstracts of XVIII International School–Seminar on New Magnetic Materials of Microelectronics* (Mosk. Gos. Univ., Moscow, 2002), Part 1, p. 102.

9. N. G. Bebenin and V. V. Ustinov, Fiz. Met. Metalloved. **84**, 29 (1997).

10. G. G. Malinetskiĭ and A. B. Potapov, *Modern Problems in Nonlinear Dynamics* (Editorial URSS, Moscow, 2002).

11. P. Berge, Y. Pomeau, and C. Vidal, *L'Ordre dans le Chaos. Vers une Approche Deterministe de la Turbulence* (Hermann, Paris, 1988; Mir, Moscow, 1991).

Translated by V. Sakun

N-Shaped Voltage–Current Characteristic and Current Oscillations in $Sm_{1-x}Sr_xMnO_3$ Manganite

I. K. Kamilov*, K. M. Aliev, Kh. O. Ibragimov, and N. S. Abakarova

Institute of Physics, Dagestan Scientific Center, Russian Academy of Sciences, Makhachkala, 367003 Dagestan, Russia
*e-mail: kamilov@datacom.ru
Received September 8, 2003

The voltage–current characteristics (VCC) of $Sm_{1-x}Sr_xMnO_3$ samples with $x = 0.425$ and $x = 0.450$ were experimentally studied at a temperature of 77 K in pulsed and constant electric (E) and magnetic (H) fields up to 10 kOe for the $H \parallel E$ and $H \perp E$ orientations. N-shaped VCCs and high-frequency (up to 3 MHz) current oscillations were observed. It was found that the effect of colossal magnetoresistance had a threshold character and was smoothly reduced to zero with $E \longrightarrow 0$. © 2003 MAIK "Nauka/Interperiodica".

PACS numbers: 72.20.Ht; 72.80.Ga; 75.47.Gk

The discovery of colossal magnetoresistance (CMR) in manganites stimulated research into the charge-transfer processes in systems with strong interaction between the magnetic, lattice, and electron subsystems. It has been found that the magnetoresistive effect decreases with increasing voltage and that the magnitude of the effect strongly depends on the barrier structure [1–7].

Nonlinear voltage–current characteristics (VCCs) of manganites and manganite-based heterostructures, as well as the relaxation processes of current steady-state transition under the action of voltage, were studied in [8–11]. Nonlinear VCCs exhibiting sublinear or superlinear behavior [8–10] and S-shaped VCCs [9, 10] were observed. It was shown in [12] that the transition of current to its steady-state value corresponding to the applied voltage has the character of a relaxation process with long characteristic times (up to 10 min). It should be noted that the majority of studied VCCs exhibit hysteresis; i.e., the ascending and descending VCC branches do not coincide. The nonlinearity can be caused by such physical mechanisms as the current effect on the magnetic homogeneity of the system [13], inelastic charge-carrier scattering in magnetoactive layers by the contact [6, 9], or electric modulation of the double-exchange processes in ferromagnetic systems [8].

The goal of this work was to study the effect of electric field on the CMR magnitude in manganites. Measurements were made in $Sm_{1-x}Sr_xMnO_3$ manganites with $x = 0.425$ and $x = 0.450$ at a temperature of 77 K in magnetic fields up to 10 kOe for $H \parallel E$ and $H \perp E$.

X-ray diffraction showed that the ceramic $Sm_{1-x}Sr_xMnO_3$ samples under study were orthorhombic perofskites with a homogeneous granulometric composition, good cleavage, and a porosity of ~20%. The results of a thorough experimental study of heat capacity and electrical resistance of the samples with $x = 0.450$ over a wide temperature range are reported in [14]. The sizes of the samples with $x = 0.425$ and $x = 0.450$ were $6 \times 1.7 \times 0.7$ mm and $2.5 \times 1.2 \times 0.7$ mm, respectively. Current contacts were applied to the ends of the samples by silver paste. All measurements were performed at a temperature of 77 K. The sample temperature was monitored by a copper–constantan thermocouple.

The VCCs of the samples were measured both in the dc mode and in the pulse operation mode of the voltage generator; $R_{smp} \gg R_i$, where R_{smp} is the sample resistance and R_i is the current-collecting resistor connected in series with the sample. The duration of a triangular pulse used in VCC measurements did not exceed 120 μs; the duration of rectangular pulses did not exceed 80 μs with 0.1-μs leading edges or shorter.

The ascending and descending VCC branches measured for the sample with $x = 0.425$ in the pulse mode are shown in Fig. 1a. The ohmic segments at the beginning of VCC goes smoothly to the superlinear segments with the characteristic slope $I \sim V^n$, where $n = 1.4$–1.6. Then, at voltages $V \approx 1.5$ V, the VCC has an N-shaped segment. As the voltage increases, this segment shifts again to a positive branch ($dI/dU > 0$).

The ascending and descending VCC branches measured for various maximal applied voltages do not coincide; i.e., the VCCs exhibit hysteresis whose magnitude depends both on the voltage and on the load resistance. For an appropriately chosen load resistance, oscillations appear in the current pulse (Fig. 1b). The amplitude and frequency of these oscillations depend on the applied voltage. In a field E, these oscillations show the following characteristic features: (1) the frequency decreases and the amplitude increases with increasing field; (2) the second positive VCC branch also exhibits
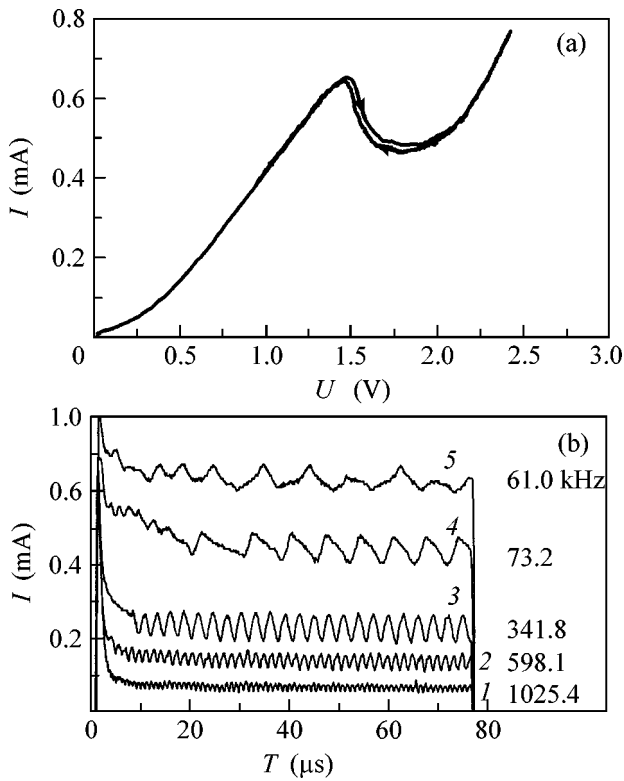
Fig. 1. (a) Ascending and descending VCC branches; (b) oscillations in current pulse at different voltages U: (*1*) 2.48, (*2*) 2.64, (*3*) 2.72, (*4*) 2.8, and (*5*) 3.02 V. The curves were measured in a $Sm_{1-x}Sr_xMnO_3$ sample with $x = -0.425$ at a temperature of 77 K.
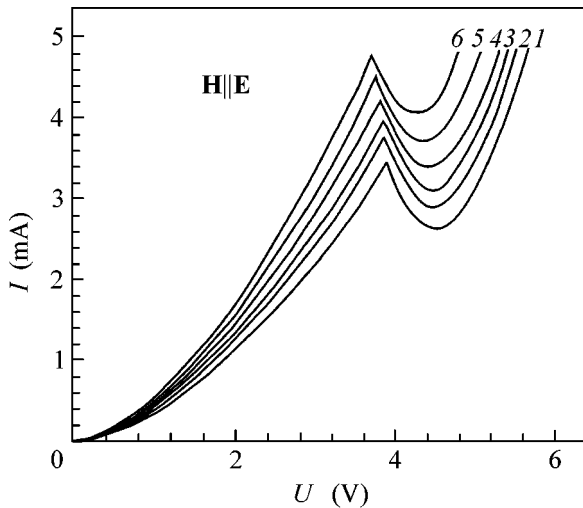

Fig. 2. VCCs for a $Sm_{1-x}Sr_xMnO_3$ sample with $x = 0.450$ measured at different values of longitudinal magnetic field H: (*1*) 0, (*2*) 1.38, (*3*) 2.25, (*4*) 4.5, (*5*) 6.7, and (*6*) 8.5 kOe at a temperature of 77 K.

oscillations after the *N*-shaped segment up to high voltages U (20–30 V); the properties of these oscillations (period doubling, quasi-periodicity, alternation, stochastic behavior, etc.) are typical of chaotic systems. The frequencies corresponding to maximal amplitudes were determined from the Fourier analysis and are given in Fig. 1b together with the pulse. The reversal of current direction through the sample has no effect on the VCC (VCCs are absolutely identical for both directions). Although the current reversal slightly changes the shape of current oscillations, the main oscillation properties remain the same, independently of the voltage U. For the *N*-shaped segment at the beginning of the current pulse, the current decreases with a characteristic time on the order of several microseconds.

In the longitudinal ($H \parallel E$) and transverse ($H \perp E$) pulsed electric fields, the CMR effect calculated by the formula $(\rho_H - \rho_0)/\rho_H$ reached 35%. It was found that the exposure to a magnetic field reduced the oscillation amplitude and shifted the threshold of *N*-shaped segment toward lower electric fields.

The VCCs for a sample with $x = 0.450$ measured in longitudinal magnetic fields $H \parallel E$ and constant electric fields are shown in Fig. 2. It should be noted that all measurements were performed at a constant temperature $T = $ const (77 K). The temperature was monitored by a thermocouple to make sure that the power dissipation on the sample did not lead to Joule heating of the sample. As in the case of $x = 0.425$, the VCCs measured for the samples with $x = 0.450$ in a magnetic field show that the CMR reaches 35% and the threshold of *N*-shaped segment slightly decreases with increasing magnetic field. As is seen from Fig. 2, the CMR is slightly reduced at the *N*-shaped segment. However, at the minimum point and on the second ascending VCC branch, the CMR effect is on the same or even higher order than before the *N*-shaped segment. The VCC behavior in the transverse magnetic fields $H \parallel E$ is absolutely identical with its behavior in the longitudinal magnetic fields $H \perp E$. It should be noted that there is a slight anisotropy of the CMR; the effect of longitudinal field is stronger, so that the CMR effect is more pronounced in the longitudinal fields on all VCC segments. On the VCC segments obeying the law $I \sim V^{1.6}$, the CMR magnitude is constant or slightly decreases (~3%) with increasing voltage up to the appearance of the *N*-shaped segment.

The CMR effect was thoroughly studied under conditions where the voltage bias U was reduced to zero ($U \longrightarrow 0$). It was found that the CMR effect had an electric-field threshold (!). As the applied voltage was reduced, the CMR gradually decreased on the linear segment and disappeared at $U = 1$–2 mV for the samples of both compositions in a magnetic field $H = 10$ kOe. It was also found that the CMR on the linear VCC segment was always greater at $H \parallel E$ than at $H \perp E$ (up to the complete disappearance of the CMR).

If a sample does not contain any built-in hetero-structures or sandwich structures, point contacts, or other types of contacts with nonequilibrium properties [8–12], the results of measuring *N*-shaped VCCs in manganites can be interpreted using the $\Delta m\tau$ model suggested in [15]. In this model, the resistivity is calculated using the Drude formula:

$$\rho = m^*/e^2 n\tau, \qquad (1)$$

where e is the electron charge, m^* is the effective mass, n is the concentration of charge carriers, and the relaxation time τ is the sum $\tau^{-1} = \tau_{st}^{-1} + \tau_{ph}^{-1} + \tau_m^{-1}$, where τ_{st}, τ_{ph}, and τ_m are the characteristic times of scattering by the static breakings of translational symmetry, by phonons, and by local magnetic-moment fluctuations, respectively. The resultant expression with allowance for the activation energy Δ is

$$\rho = e^{2\Delta/3T}(\rho_{st} + \rho_{ph} + \rho_m). \qquad (2)$$

Strongly inelastic charge-carrier scattering at certain values of the threshold electric field can lead to a sharp increase in the resistance as a result of a decrease in the scattering time, especially for the second (polaron) and third (spin disorder) terms in brackets in Eq. (2). This can lead to the appearance of an *N*-shaped segment in the VCC.

A further rise in the voltage increases the energy of charge carriers for overcoming the polaron and spin barriers. Thus, a new increase in the current is observed in the VCC. The current effect on the magnetic homogeneity of the systems under consideration or some other mechanism causing a sharp change in the concentration of charge carriers also cannot be excluded [12]. As to the threshold character of the CMR with respect to the electric field, it obviously requires further investigation in many systems with various compositions.

REFERENCES

1. L. P. Shelp, A. Fert, F. Fettar, *et al.*, Phys. Rev. B **56**, R5747 (1997).

2. J. S. Moodera, L. R. Kinder, T. M. Wong, *et al.*, Phys. Rev. Lett. **74**, 3273 (1995).

3. A. M. Bratkovsky, Phys. Rev. B **56**, 2344 (1997).

4. X. Zhang, B. Z. Li, J. Z. Sun, *et al.*, Phys. Rev. B **56**, 5484 (1997).

5. S. Zhang, P. M. Levy, A. C. Marley, *et al.*, Phys. Rev. Lett. **80**, 2941 (1998).

6. M. A. Belogolovskiĭ, Yu. F. Revenko, A. Yu. Gerasimenko, *et al.*, Fiz. Nizk. Temp. **29**, 889 (2003) [Low Temp. Phys. **29**, 666 (2003)].

7. Yu. F. Popov, A. M. Kadomtseva, K. I. Kamilov, *et al.*, Fiz. Tverd. Tela (St. Petersburg) **45**, 1221 (2003) [Phys. Solid State **45**, 1280 (2003)].

8. M. Tanaka, J. Zhang, and T. Kawai, Phys. Rev. Lett. **88**, 027204 (2002); C. Martin, A. Maignan, M. Hervien, *et al.*, Phys. Rev. B **60**, 12191 (1999).

9. M. A. Belogolovskiĭ, Yu. F. Revenko, A. Yu. Gerasimenko, *et al.*, Fiz. Nizk. Temp. **28**, 553 (2002) [Low Temp. Phys. **28**, 391 (2002)].

10. A. Guha, N. Khare, A. K. Raichaudhuri, *et al.*, Phys. Rev. B **62**, R11941 (2000).

11. J. Z. Sun, J. Magn. Magn. Mater. **202**, 157 (1999).

12. M. K. Gubkin, T. M. Pereklina, A. M. Balbashev, *et al.*, Fiz. Tverd. Tela (St. Petersburg) **43**, 293 (2001) [Phys. Solid State **43**, 305 (2001)].

13. S. Heim, T. Nachtrab, M. Moble, *et al.*, Physica C (Amsterdam) **367**, 348 (2002).

14. Sh. B. Abdulvagidov, I. K. Kamilov, A. M. Aliev, and A. B. Batdalov, Zh. Éksp. Teor. Fiz. **123**, 857 (2003) [JETP **96**, 757 (2003)].

15. A. B. Beznosov, B. I. Belevtsev, E. L. Fertman, *et al.*, Fiz. Nizk. Temp. **28**, 774 (2002) [Low Temp. Phys. **28**, 556 (2002)].

Translated by K. Chamorovskiĭ

Elastic Properties of D₂O Ices in Solid-State Amorphization and Transformations between Amorphous Phases

E. L. Gromnitskaya, O. V. Stal'gorova, A. G. Lyapin,
V. V. Brazhkin, and O. B. Tarutin

Institute of High-Pressure Physics, Russian Academy of Sciences, Troitsk, Moscow region, 142190 Russia

Received September 12, 2003

Nonequilibrium phase transformations in D₂O ices, including the solid-state amorphization of ice $1h$ ($1h$–hda) and the heating-induced transition cascade hda–lda–$1c$–$1h$ from high-density amorphous (hda) ice to low-density amorphous (lda) ice followed by crystallization in cubic ice $1c$ and phase transition to ordinary hexagonal ice $1h$, were studied using an ultrasonic technique. It has been shown that, as in H₂O ice, the softening of a crystal lattice or an amorphous network precedes nonequilibrium transformations. However, noticeable isotopic differences in the behavior of the elastic properties of H₂O and D₂O, in particular, their $1h$ and hda modifications, call for a more detailed study of the structural features of these H₂O and D₂O phases. © *2003 MAIK "Nauka/Interperiodica".*

PACS numbers: 62.20.Dc; 62.50.+p; 64.70.Kb

1. H₂O and D₂O ices can be considered as model systems for the study of pressure effects on hydrogen-bonded substances. The phase diagram of H₂O, as well as that of its isotope analogue D₂O, is interesting for the fact that at least 12 crystalline ice phases are observable in the attainable pressure and temperature ranges [1–3]. At temperatures below the ice crystallization point ($T_{cr} \approx 150$ K), ice offers a unique opportunity to study nonequilibrium phase transformations in solids, such as solid-state amorphization (SSA) [4, 5] and transformations between amorphous ice phases [6, 7]. Many investigations into the structure and phase transformations in water phases and ice modifications are dealing with the properties of D₂O. Elastic [8–10] and inelastic [11, 12] neutron scattering studies of D₂O amorphous ice phases are a demonstrative example.

Currently, a significant progress has been achieved in the understanding of the nature of SSA [5, 13–16] and transformations between amorphous phases [7, 17–19]. However, the details of the transformation scenario are as yet unclear. New information on the dynamics of metastable transformations and the character of metastable phases can be gained from a comparitative study of structural isotope analogues, in particular, H₂O and D₂O ice phases.

The thermodynamic characteristics of H₂O and D₂O modifications differ from one another only by several percent; equilibrium lines between phases are very close to one another [1]. Previously [22], it was found that the SSA pressure for D₂O is about 0.05 GPa higher than for H₂O. However, dynamic properties, such as

some vibrational frequencies, can differ appreciably. For example, intramolecular (to within the accuracy of intracrystal interactions) Raman modes for ices $1h$ H₂O and $1h$ D₂O differ by $\approx 35\%$ [20]. Noteworthy is a significant effect of isotope substitution on the value and behavior of the shear modulus in a solid [21]. The nonequilibrium transformations considered here are determined by both thermodynamic relations between phases and the atomic dynamics [13–19]; therefore, the role of isotope effects in such transitions is not clear a priori. In fact, isotope effects on nonequilibrium transitions, including those in ices, have not yet been studied systematically.

Here, we employed ultrasound to study nonequilibrium transformations in D₂O ice under pressure and measured elastic moduli for D₂O ice phases. The elastic properties were studied during pressure-induced SSA in hexagonal $1h$ D₂O ice and during heating-induced transition between high-density and low-density amorphous ices $hda \longrightarrow lda$. Many of our inferences made in this work for D₂O coincide with those made previously for H₂O. Nonetheless, significant isotopic differences observed in the behavior of H₂O and D₂O call for a more detailed structural comparison of H₂O and D₂O phases, especially under pressure.

2. Ultrasonic experiments for D₂O ices were carried out in the pressure range 0–1.7 GPa at temperatures from the nitrogen boiling point to 180 K. The experimental procedure was similar to the one we employed previously to study H₂O ices [5, 7, 16, 18]. Polycrystalline samples (16 mm in diameter, 8 mm high) were pre-
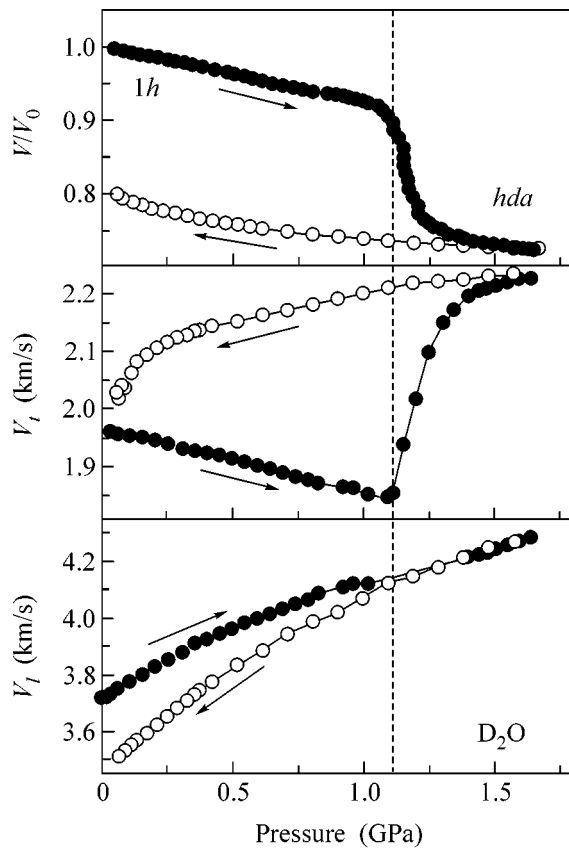
Fig. 1. Experimentally observed variations in the relative volume and the transverse and longitudinal ultrasonic wave velocities upon pressure-induced SSA in ice 1*h* D$_2$O at 78 K. Arrowed lines show the directions of pressure change. The dashed vertical marks the SSA onset.

Fig. 2. Calculated variations in the shear modulus and bulk modulus during SSA in ice 1*h* D$_2$O. Crosses show *G* variation during SSA in ice 1*h* H$_2$O given for comparison. The other notations are the same as in Fig. 1.

pared by rapid cooling of heavy water in liquid nitrogen. *x*-Cut and *y*-cut quartz plates with the carrier frequency 5 MHz were used as piezometric gages. In the experiments, the velocities of longitudinal (V_l) and transverse (V_t) ultrasonic waves were measured as a function of either pressure or temperature.

3. The 1*h* ⟶ *hda* SSA phenomenon at *T* = 78 K in D$_2$O was observed as abrupt changes in the travel time of ultrasonic waves and in the sample length in the pressure range 1.14–1.51 GPa. Experimental plots of the relative volume and ultrasound velocity versus pressure are given in Fig. 1. The density jump in SSA was ≈18%, which is smaller than the density change in H$_2$O (≈20%). Interestingly, despite the significant changes in the volume of the sample and the travel time of a longitudinal ultrasonic signal, SSA is, in fact, not detected as a change in the longitudinal wave velocity; in H$_2$O, in contrast, a clear-cut irregularity was observed in the V_l(*T*) trend [5, 16, 18]. The SSA in hexagonal 1*h* D$_2$O ice is preceded by a near-linear decrease in the shear wave velocity.
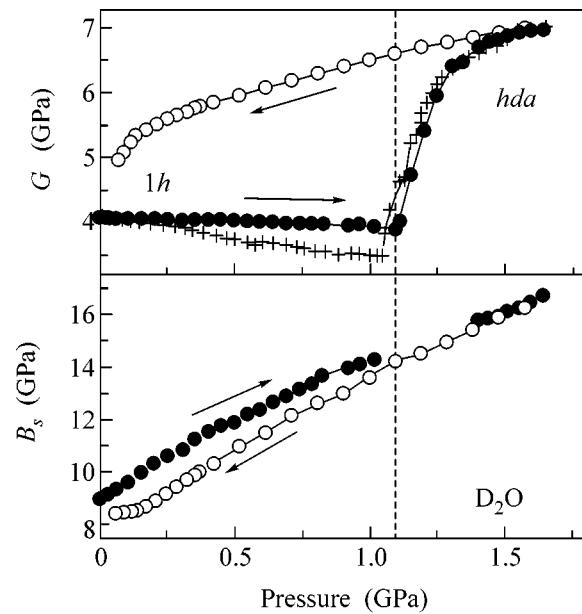
The calculated variations in the adiabatic bulk modulus B_s and shear modulus *G* upon the transition 1*h* ⟶ *hda* in D$_2$O are plotted in Fig. 2. As in H$_2$O, the trend of the shear elasticity is evidence that the crystal-structure instability of ice 1*h* develops before SSA in D$_2$O. At the same time, the negative pressure derivatives of V_t (Fig. 1) and *G* (Fig. 2) for phase 1*h* D$_2$O are far smaller than the respective values for 1*h* H$_2$O ices [5, 16, 18].

To study transformations between amorphous D$_2$O ice phases, we measured the longitudinal and transverse ultrasonic wave velocities as a function of temperature in the regime of natural heating of ice *hda* from *T* = 78 K at a fixed pressure *P* = 0.05 GPa. The experimental results are presented in Fig. 3. Phase transition *hda* ⟶ *lda* is preceded by the decreases in both wave velocities, which is evidence of softening of the amorphous network of ice *hda*. Transition *hda* ⟶ *lda* is accompanied by a dramatic change in volume; the magnitude of the jump in D$_2$O (≈18%) is again slightly smaller than in H$_2$O [16, 18]. Note that the densities of phases *lda*, 1*c*, and 1*h* are practically identical, whereas the features observed in the V_l(*T*) and V_t(*T*) plots in the range 100–180 K show the transition sequence *hda* ⟶ *lda* ⟶ 1*c* ⟶ 1*h* (Fig. 3). We assume that the temperature range in the case of D$_2$O, as for H$_2$O [18], can be divided in segments as follows: 78–130 K is the domain of existence of phase *hda*; 130–140 K is the transition *hda* ⟶ *lda*; 140–148 K is the domain of existence
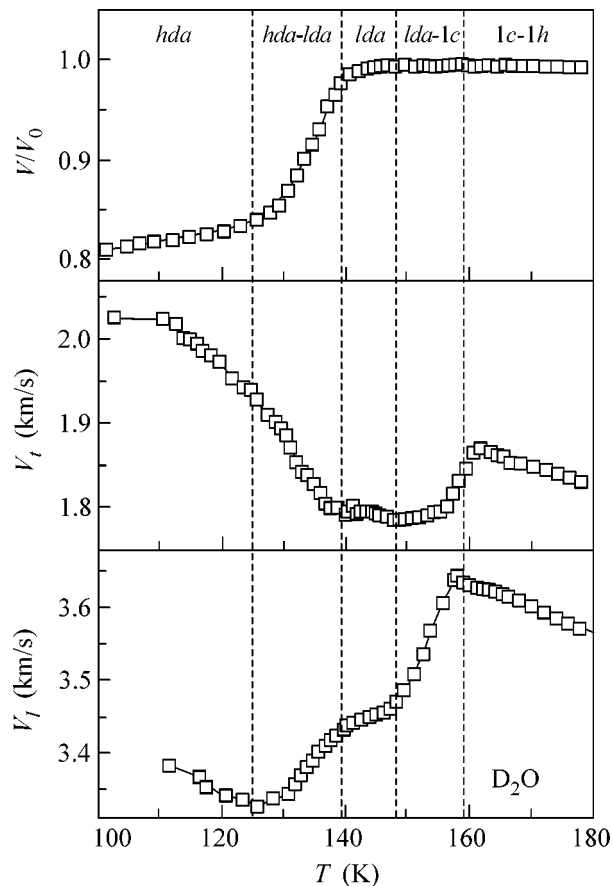
Fig. 3. Experimentally observed variations in the relative volume and the transverse and longitudinal ultrasonic velocities upon heating ice *hda* D_2O under 0.05 GPa. Dashed verticals mark structure-transformation stages.
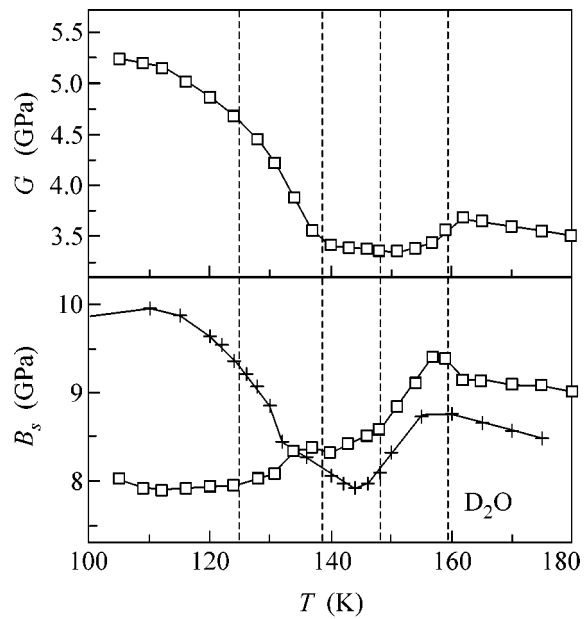

Fig. 4. Calculated variations in the shear modulus and bulk modulus upon heating ice *hda* D_2O. The structure-transformation stages marked with dashed verticals correspond to Fig. 3. Crosses show B_s variation upon heating ice *hda* H_2O for comparison.

of phase *lda*; and 148–160 K is the phase transition from *lda* to cubic ice *1c*, the latter subsequently transforming to hexagonal phase *1h*.

The calculated values of the elastic moduli for this transformation cascade are presented in Fig. 4. Here, as in the case of H_2O [18], *G* softening precedes transition *hda* $\longrightarrow$ *lda*. A further decrease in *G* is a consequence of this transition. In the case of D_2O, however, we do not observe softening of the bulk modulus associated with transition *hda* $\longrightarrow$ *lda* (Fig. 4); in H_2O, B_s decreases from about 10 to 8.5 GPa in the range 78–130 K.

4. Thus, our data indicate that, as in H_2O, the elastic softening of the structure (the crystal lattice in ice *1h* or amorphous network in ice *hda*) precedes the nonequilibrium transformations under discussion; this fully confirms the general inferences made previously about the nature and mechanisms of such transformations [13–19]. Nonetheless, H_2O and D_2O significantly differ in their behavior. Let us consider these differences.

To understand the reasons for which the absolute value of the negative pressure derivative of *G* for D_2O is notably smaller than for H_2O, one evidently must know the whole tensor of elastic constants for ice *1h* and the pressure derivatives of its components. Unfortunately, such information is available only for H_2O at $T = 238$ K [23, 24]. Nonetheless, we can assume that lattice softening and instability of ice *1h* D_2O is governed by the same shear constant as for H_2O, namely, $\mu_1 = 1/2(c_{11} - c_{12})$; for details, see [16, 18]. From the microscopic viewpoint, the higher degree of ordering in ice *1h* D_2O [25] can be responsible for the different behaviors of elastic properties for phases *1h* H_2O and *1h* D_2O; this is seen, in particular, from the smaller mean-square displacements of atoms in the *1h* D_2O lattice.

The isotope shift of the SSA pressure for ice D_2O to higher values (see also [22]) can be interpreted in terms of a model that considers the dynamic lattice instability as the driving force of SSA [13, 14], if we assume that the instability criterion for the soft mode is an analogue of the Lindemann criterion for melting. The vibrational amplitude is inversely proportional to the effective mass. In the case of D_2O, both the intramolecular and the intermolecular vibrations are associated with smaller mean-square atomic displacements; in this case, therefore, the isotope effect in ice amorphization can be explained both qualitatively and quantitatively.

Another intriguing feature of SSA in D$_2$O is a weak decrease in B_s upon amorphization, unlike H$_2$O, where B_s increases in accordance with the fact that the transition results in a denser phase. For amorphous ice *hda* D$_2$O, modulus B_s for all pressures has a lower value than for ice 1*h* (Fig. 2); in the case of H$_2$O, an opposite situation is observed [16, 18]. Moreover, the results of studying the transformation cascade *hda* ⟶ *lda* ⟶ 1*c* ⟶ 1*h* show that the bulk modulus for phase *hda* D$_2$O is lower than the respective values for all tetrahedral D$_2$O phases, namely, *lda*, 1*c*, and 1*h* (here, tetrahedral phases mean phases in which oxygen atoms are surrounded by near-regular tetrahedral neighboring O atoms). For H$_2$O ices, phase *hda* has a B_s value slightly greater than any of the three aforementioned tetrahedral phases [16, 18]. This is natural, since the ice *hda* density is appreciably higher than the densities of these phases. Note that the ratio of the bulk moduli of the tetrahedral phases is the same for H$_2$O [16, 18] and D$_2$O (Fig. 4): $B_{lda} < B_{1h} < B_{1c}$; this might be associated with a decrease in the disorder of the tetrahedral packing of oxygen atoms.

The quantitative and qualitative differences in the B_s values for phases *hda* H$_2$O and D$_2$O must be related to the different behaviors of the 1st and 2nd coordination spheres under pressure. Recent neutron studies of ice *hda* D$_2$O under pressure showed [10] that, under pressure, the 2nd oxygen coordination sphere in phase *hda* D$_2$O is severely contracted (the 1st coordination sphere is virtually incompressible); under about 2 GPa, the 2nd sphere approaches the 1st sphere. Note that the 1st and 2nd spheres are not hydrogen-bonded [9, 10]. In fact, various parts of a network formed from hydrogen-bonded oxygen atoms penetrate each other under pressure [10]; this analogy is exemplified by the clathrate structure of ice VI (see [12]). To our knowledge, no similar data exist for phase *hda* H$_2$O; however, the dynamics of the interpenetration of the 1st and 2nd oxygen coordination spheres in this case can be different. Indeed, the motion dynamics of H and D atoms in similar ice phases are substantially different from both classical and quantum viewpoints.

Quantum calculations for phases *hda* H$_2$O and D$_2$O [26] showed a significantly higher extent of quantum (tunneling) delocalization of H atoms. The lower mobility of D$_2$O molecules in the course of structure ordering (in particular, in the classical meaning of this word) manifests itself as the slower kinetics of molecular reorientation during structure ordering [27] or as a wider pressure range of O–D optical mode softening compared to the O–H mode [28, 29]. Thus, in ice *hda* H$_2$O, extra relaxation mechanisms can exist for the softer nanodomains that appear upon the compression of an amorphous network, such as the reorientation of molecules or the quicker dynamics of interpenetration of the 1st and 2nd oxygen coordination spheres.

To summarize, we must stress the unexpectedly high isotope effects observed for the elastic properties of H$_2$O and D$_2$O ices. Evidently, the interpretation of these effects calls for the more detailed experimental and theoretical comparison of the structure, dynamic properties, and elastic properties of H$_2$O and D$_2$O phases.

REFERENCES

1. E. Yu. Tonkov, *High Pressure Phase Transformations. A Handbook* (Metallurgiya, Moscow, 1988; Gordon and Breach, Philadelphia, 1992), Vol. 2.

2. C. Lobban, J. L. Finney, and W. F. Kuhs, Nature **391**, 268 (1998).

3. M. Koza, H. Schober, A. Tölle, *et al.*, Nature **397**, 660 (1999).

4. O. Mishima, L. D. Calvert, and E. Whalley, Nature **310**, 393 (1984).

5. O. V. Stal'gorova, E. L. Gromnitskaya, and V. V. Brazhkin, Pis'ma Zh. Éksp. Teor. Fiz. **62**, 334 (1995) [JETP Lett. **62**, 356 (1995)].

6. O. Mishima, L. D. Calvert, and E. Whalley, Nature **314**, 76 (1985).

7. O. V. Stal'gorova, E. L. Gromnitskaya, V. V. Brazhkin, and A. G. Lyapin, Pis'ma Zh. Éksp. Teor. Fiz. **69**, 653 (1999) [JETP Lett. **69**, 694 (1999)].

8. M. A. Floriano, E. Whalley, E. C. Svenson, and V. S. Sears, Phys. Rev. Lett. **57**, 3062 (1986).

9. J. L. Finney, A. Hallbrucker, I. Kohl, *et al.*, Phys. Rev. Lett. **88**, 225503 (2002).

10. S. Klotz, G. Hamel, J. S. Loveday, *et al.*, Phys. Rev. Lett. **89**, 285502 (2002).

11. H. Schober, M. Koza, A. Tölle, *et al.*, Physica B (Amsterdam) **241–243**, 897 (1998).

12. A. I. Kolesnikov, J. Li, S. F. Parker, *et al.*, Phys. Rev. B **59**, 3569 (1999).

13. V. V. Brazhkin and A. G. Lyapin, High Press. Res. **15**, 9 (1996).

14. A. G. Lyapin and V. V. Brazhkin, Phys. Rev. B **54**, 12036 (1996).

15. V. V. Brazhkin, A. G. Lyapin, O. V. Stalgorova, *et al.*, J. Non-Cryst. Solids **212**, 49 (1997).

16. A. G. Lyapin, O. V. Stal'gorova, E. L. Gromnitskaya, and V. V. Brazhkin, Zh. Éksp. Teor. Fiz. **121**, 335 (2002) [JETP **94**, 283 (2002)].

17. O. Mishima and H. E. Stanley, Nature **396**, 329 (1998).

18. E. L. Gromnitskaya, O. V. Stal'gorova, V. V. Brazhkin, and A. G. Lyapin, Phys. Rev. B **64**, 94205 (2001).

19. A. G. Lyapin, V. V. Brazhkin, E. L. Gromnitskaya, *et al.*, in *New Kinds of Phase Transitions: Transformations in Disordered Substances*, Ed. by V. V. Brazhkin *et al.* (Kluwer, Dordrecht, 2002), p. 449.

20. T. C. Sivakumar, S. A. Rice, and M. G. Sceats, J. Chem. Phys. **69**, 3468 (1978).

21. L. Gromnitskaya, O. V. Stal'gorova, and S. M. Stishov, Pis'ma Zh. Éksp. Teor. Fiz. **69**, 36 (1999) [JETP Lett. **69**, 38 (1999)].

22. M. A. Floriano, Y. P. Handa, D. D. Klug, and E. Whalley, J. Chem. Phys. **91**, 7187 (1989).

23. R. E. Gagnon, H. Kiefte, M. J. Clouter, and E. Whalley, J. Phys. (Paris) **48**, C1-29 (1987).

24. R. E. Gagnon, H. Kiefte, M. J. Clouter, and E. Whalley, J. Chem. Phys. **92**, 1909 (1990).

25. W. F. Kuhs and M. S. Lehmann, J. Phys. (Paris) **48**, C1-3 (1987).

26. H. Gai, G. K. Schenter, and B. C. Garrett, Phys. Rev. B **54**, 14873 (1996).

27. G. P. Johari and E. Whalley, J. Chem. Phys. **70**, 2094 (1979).

28. P. Pruzan, J. Mol. Struct. **322**, 279 (1993).

29. H. Yamawaki, M. Sakashita, H. Fujihisa, and K. Aoki, Rev. High Pressure Sci. Technol. **7**, 1135 (1998).

Translator O. Fedorova

Appearance of Anomalous Phase in ⁴He Crystal in the Presence of Small ³He Impurity

V. L. Tsymbalenko

Institute of Superconductivity and Solid-State Physics, Russian Research Centre Kurchatov Institute,
pl. Akademika Kurchatova 1, Moscow, 123182 Russia
e-mail: vlt@isssph.kiae.ru
Received September 18, 2003

The kinetics of formation of an anomalous phase from a solution with a small ³He impurity was studied in the temperature range 0.2–0.7 K up to a supersaturation of ~30 mbar. The phase diagram was determined for normal and anomalous growths. It is found that, in the presence of impurities, the formation of a fast-growing state is retarded. This experimental fact indicates that the dissipative processes in fluids have an appreciable effect on the phase formation kinetics. The retardation is, possibly, caused by the direct interaction of an impurity with the crystal surface. © 2003 MAIK "Nauka/Interperiodica".

PACS numbers: 67.80.Mg

1. INTRODUCTION

To date, a sharp transition of helium crystal from the state with slow growth kinetics to the phase with rates several orders higher has not been explained theoretically [1–8]. It is even unclear whether this transition is associated with the bulk or surface crystal properties. On the one hand, simultaneous increase in the rates of all facets, below both the second [2] and the third roughening transitions [8], counts in favor of the bulk mechanism. It would be logical to expect that the facets of different crystallographic orientations with different roughening transition temperatures and surface parameters (e.g., linear step energies or interplanar spacings) undergo transition to the anomalous state at different degrees of supersaturation. On the other hand, the bulk thermodynamic parameters (including those indicated above) of fluid and crystal have no singularities in this temperature range and depend weakly on temperature. This cannot explain the observed appreciable temperature-induced increase in the critical supersaturation Dp_0 corresponding to the onset of transition [5]. The general form of this dependence is the same as for the concentration growth of the normal component that determines the step kinetics at the facet surface. This, in turn, favors the surface formation mechanism for the anomalous state.

The introduction of a small ³He impurity sizably affects the kinetics of surface defects [9], but it has only a little (measured by concentration) effect on the bulk thermodynamic parameters. The experiment with impurities allows additional arguments to be gained in favor of one or another of hypotheses. Moreover, the effect of even a low impurity concentration can be quite substantial at low temperatures. According to the theoretical estimates [10] and experimental data [11, 12], the impurity is adsorbed at the liquid–crystal interface in a potential well with a depth of ~4 K. For our concentrations, the population of the adsorbed layer below ~0.4 K is on the order of unity, so that a layer of two-dimensional Fermi liquid forms at the surface. The appearance of such a layer, generally, can change substantially the formation kinetics for the anomalous state.

Earlier, it has been reported that the introduction of a small ³He impurity increases the critical supersaturation at 0.68 K [8] and in the range 2 mK – 0.2 K [3]. In this work, the results of measurements in a solution with atomic concentration $x = 180$ ppm and temperatures 0.2–0.7 K are reported.

2. MEASUREMENTS AND EXPERIMENTAL RESULTS

The measurement technique and the container design were described in detail in [5, 7]. We present here only the key experimental details. Helium crystal was nucleated at the center of a cylindrical container of volume 1.8 cm³ by an electrostatic field pulse. With this method, the initial supersaturation Dp_0 could be established in the interval from zero (phase-equilibrium pressure) to its maximal value that was determined by the spontaneous nucleation at the inner container wall. A change in pressure in the course of growth was measured by a capacitive transducer with a time resolution of 35 μs. A temperature of 0.48 K was achieved by the evacuation of ³He vapor and served as a starting point for the magnetic cooling by paramagnetic salt (chrome–potassium alum). Temperature was measured by a Matsushita thermometer placed inside the container in contact with the superfluid helium.
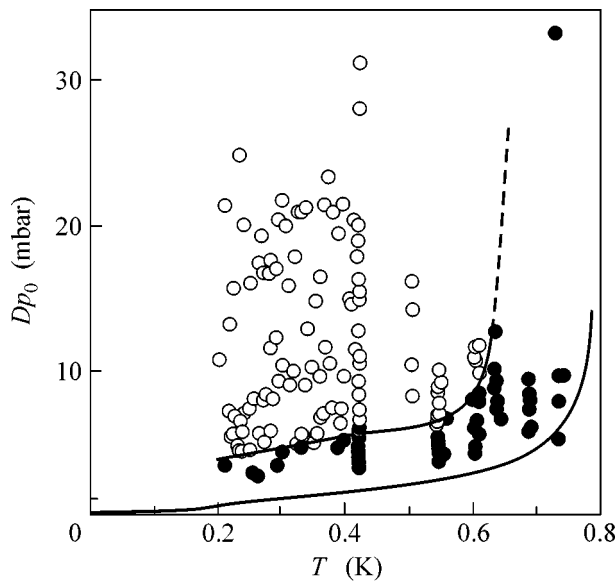
Fig. 1. Phase diagram of the anomalous state in a solution with a concentration of 180 ppm. Light circles correspond to the points of transition to the anomalous state, and black circles are for the normal growth. The lower curve is a boundary between these two regions in pure helium.
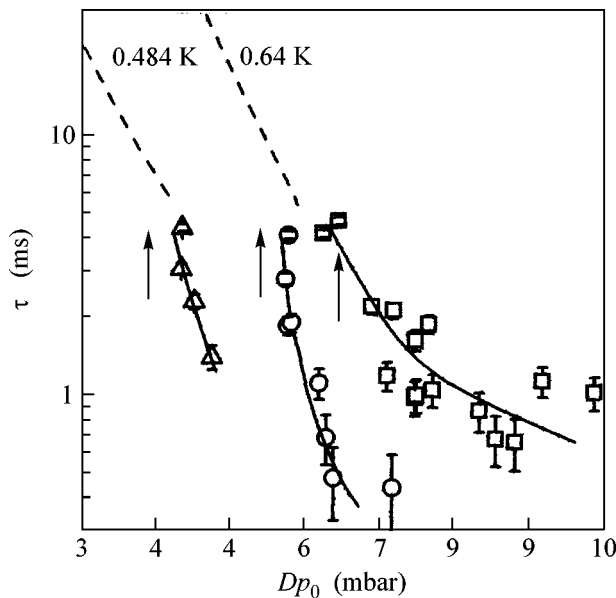

Fig. 2. Delay time as a function of initial supersaturation at three temperatures: T = (triangles) 0.24, (circles) 0.42, and (squares) 0.545 K. The dashed curves correspond to pure helium. The solid lines are drawn for clarity. The arrows to the left of the points indicate the values of critical supersaturation for these temperatures in the diagram of the anomalous state (see Fig. 1).

The introduction of an impurity noticeably affected the crystal growth kinetics, as can well be seen from the record of a pressure drop in the container during the growth. The overall trend consisted of growth deceler-

ation, but the pressure curves had a more complicated character and were not described by the growth coefficient alone, as in pure helium [13]. In this case, analysis of kinetics requires the solution of a rather complex problem of heat and impurity flows in fluid. For this reason, only those results which did not change qualitatively upon the inclusion of impurities are presented in this work. Among these is the transition to the anomalous state, which, as in pure helium, is detected from the abrupt pressure drop due to a change in the growth kinetics [4]. Therefore, the growth rate in solutions also increases jumpwise by several orders of magnitude. After the transition, the crystal growth time decreases to ~0.2 ms. As shown in [6, 7], this time is determined by the oscillating growth mode. Due to a qualitative similarity of the processes of anomalous state formation in pure helium and in solution, one can construct a phase diagram for the anomalous state and determine its formation kinetics by measuring the delay time from the instant of crystal nucleation to the pressure jump.

The measured phase diagram is shown in Fig. 1. One can see that the boundary separating the anomalous and normal growths is shifted from its position in pure helium to higher supersaturations [5]. A sharp increase in the critical supersaturation observed in pure helium above ~0.75 K shifts to ~0.6 K. Thus, a small ^{3}He impurity retards the formation of the anomalous state. In Fig. 2, the same fact is seen from the plot of delay time against supersaturation. As in pure helium, the delay time (time interval between the crystal formation and the transition to the anomalous state) shortens with lowering temperature. As before, the delay time strongly depends on the supersaturation. Note that no long delay times were detected in this experimental run, contrary to pure helium, where this time was as long as 200 ms. The possible reason is that the curve for the delay time $\tau(Dp_0)$ is steeper than in pure helium. Then, the desired segment of the curve could be missed merely because of relatively poor statistics. This conclusion is confirmed by the direct delay measurements (Fig. 2). The delay times in the solution are longer than in pure helium, in accordance with the fact that the boundary of anomalous region is shifted upward (Fig. 1). Note that, in this method, the transition is detected only during the crystal growth time (20–200 ms), so that the boundary in Fig. 1 is drawn for the delay times shorter than the indicated times.

The influence of impurities on the formation of the anomalous phase was studied in [3], where the cumulative probability distribution for its appearance was measured in the 10- and 50-ppm solutions. The normalized distribution $N(Dp)$ is related to the probability w of anomalous state formation by

$$N = 1 - \exp\left(-\frac{1}{c}\int_0^{Dp} w(x)\,dx\right), \quad Dp(t) = ct, \quad (1)$$

(see Eq. (38) in [3]). By taking the inverse of this expression, one finds the mean delay time for the formation of the anomalous state:

$$\frac{1}{w} = \left\{ -c\frac{d[\ln(1-N)]}{d(Dp)} \right\}^{-1}. \qquad (2)$$

The result of processing for a temperature of ~0.25 K is shown in Fig. 3. The data presented in [3], as well as our results, demonstrate that the delay time increases upon the introduction of impurities in helium. Although it makes no sense to compare the numerical values because of a too large data scatter (three orders of magnitude for the delay time), the overall trend (acceleration of the anomalous state formation with an increase in supersaturation) is the same in both measurement regions. Based on the tendency demonstrated by the results of work [3], one can assume that the $\tau(Dp_0)$ curve should pass to the right of and above the points measured for a solution with $x = 50$ ppm. In this case, the overall $\tau(Dp_0)$ dependence will exhibit a fast increase within a delay time range of 10–1000 ms, as was assumed previously (see above).

3. DISCUSSION

Measurements in the solution gave additional evidence that the anomalous transition observed in this work is identical with the burstlike growth observed in [3]. This was conjectured in [4] and confirmed for pure helium after measurements at temperatures down to 0.2 K [8].

The first measurements of the impurity effect on the formation kinetics of an anomalous state were performed in the temperature range 2–250 mK [3]. At these temperatures, the ^{3}He solubility in crystal is exponentially small, and the action of impurities amounts to the scattering of their atoms from the surface and the formation of an adsorbed layer. Experiments on the facet growth under these conditions [9] for the concentrations $x = 40$–220 ppm showed that the growth kinetics can adequately be described solely by the quasiparticle scattering from the steps; i.e., the saturated adsorbed layer has no noticeable effect on the kinetics. Above 0.2 K, the influence of impurities of this concentration on the step motion is negligible. In our temperature range, there are two singular points corresponding to (a) the same concentrations of both phases at $T_x \approx 0.6$ K and (b) the onset of the formation of a saturated adsorbed layer at $T_{ad} \approx 0.45$ K. Above T_x, the equilibrium impurity concentration is higher in the solid phase, and, below this temperature, it is higher in the liquid (cf. [14] and references cited therein). Exactly at this point, the concentrations are identical, so that the crystal growth does not initiate the impurity diffusion flows in the bulk and additional growth-decelerating dissipation [15]. If the role of impurity flows consisted only in the deceleration of growth kinetics, then the sin-
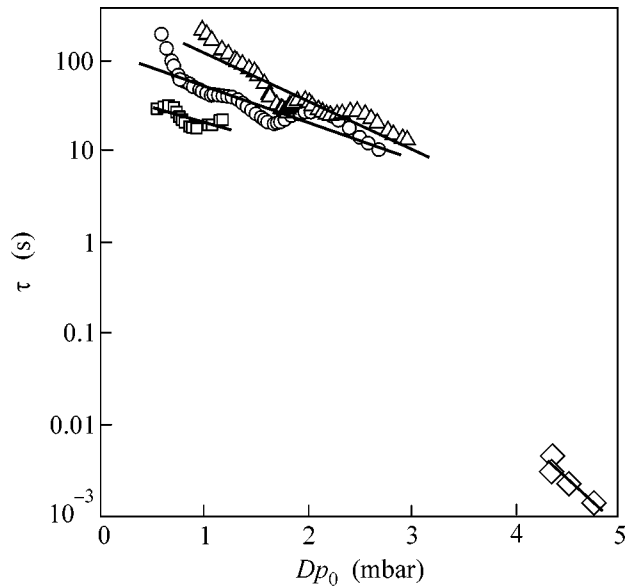

Fig. 3. Delay time as a function of initial supersaturation. Rhombi are the data of this work ($T = 0.24$ K and $x = 180$ ppm); squares, circles, and triangles are the results of work [3] recalculated using Eq. (2) for $T = 0.25$ K and concentrations $x = $ (squares) 0.1, (circles) 10, and (triangles) 50 ppm. Straight lines are drawn using the least-squares method.

gularity (decrease in the critical supersaturation) would be observed at the T_x point. However, one can see in Fig. 1 that this singularity does not occur. This signifies that the deceleration of the formation of an anomalous state is caused not only by a change in the growth kinetics. This is indirectly confirmed by a weak temperature dependence of the critical supersaturation below 0.6 K. Indeed, the impurity concentration below this temperature starts to rapidly (exponentially) decrease. When growing, the crystal "gathers" impurities, so that the characteristic time of reducing the excessive near-surface concentration also influences the growth kinetics. However, one can see in Figs. 1 and 2 that this phenomenon is reflected neither in the phase diagram nor in the delay time curves.

The second temperature point corresponds to the transition of the adsorbed layer from the rarefied two-dimensional gas state to the degenerate two-dimensional Fermi gas state. The influence of the adsorbed layer on the formation kinetics of the anomalous state is now unknown. For this reason, we restrict ourselves only to stating the fact that, at temperature T_{ad}, no anomalies are observed in the phase diagram and the state formation rate (Figs. 1, 2).

We note in conclusion that the introduction of impurities has retarded the formation of an anomalous state. This effect, however, cannot be understood only in terms of surface growth kinetics, i.e., explained by a change in the step mobility. Nevertheless, such a character of impurity action on the anomalous state is evi-

dence of the decisive role of the surface in the formation of the fast-growing phase.

REFERENCES

1. V. L. Tsymbalenko, Phys. Lett. A **211**, 177 (1996).
2. V. L. Tsymbalenko, Phys. Lett. A **248**, 267 (1998).
3. A. V. Babkin, P. J. Hakonen, A. Ya. Parshin, *et al.*, J. Low Temp. Phys. **112**, 117 (1998).
4. V. L. Tsymbalenko, Phys. Lett. A **257**, 209 (1999).
5. V. L. Tsymbalenko, J. Low Temp. Phys. **121**, 53 (2000).
6. V. L. Tsymbalenko, Phys. Lett. A **274**, 223 (2000).
7. V. L. Tsymbalenko, Zh. Éksp. Teor. Fiz. **119**, 1182 (2001) [JETP **92**, 1024 (2001)].
8. V. L. Tsymbalenko, Pis'ma Zh. Éksp. Teor. Fiz. **77**, 288 (2003) [JETP Lett. **77**, 243 (2003)].
9. V. Tsepelin, J. P. Saramaki, A. V. Babkin, *et al.*, Phys. Rev. Lett. **83**, 4804 (1999).
10. J. Treiner, J. Low Temp. Phys. **92**, 1 (1993).
11. E. Rolley, S. Balibar, C. Guthmann, and P. Nozieres, Physica B (Amsterdam) **210**, 397 (1995).
12. V. L. Tsymbalenko, Zh. Éksp. Teor. Fiz. **108**, 686 (1995) [JETP **81**, 373 (1995)].
13. L. A. Maksimov and V. L. Tsymbalenko, Zh. Éksp. Teor. Fiz. **114**, 1313 (1998) [JETP **87**, 714 (1998)].
14. S. Balibar and D. O. Edwards, Phys. Rev. B **39**, 4083 (1989).
15. S. N. Burmistrov and L. B. Dubovskii, Europhys. Lett. **24**, 749 (1993).

Translated by V. Sakun

Dephasing of Qubits by Transverse Low-Frequency Noise[¶]

Yu. Makhlin[1, 2] and A. Shnirman[1]

[1] *Institut für Theoretische Festkörperphysic, Universität Karlsruhe, D-76128 Karlsruhe, Germany*
[2] *Landau Institute for Theoretical Physics, Russian Academy of Sciences, Moscow, 117940 Russia*
e-mail: makhlin@tfp.uni-karlsruhe.de, shnirman@tfp.uni-karlsruhe.de
Received September 23, 2003

We analyze the dissipative dynamics of a two-level quantum system subject to low-frequency, e.g., $1/f$ noise, motivated by recent experiments with superconducting quantum circuits. We show that the effect of transverse linear coupling of the system to low-frequency noise is equivalent to that of quadratic longitudinal coupling. We further find the decay law of quantum coherent oscillations under the influence of both low- and high-frequency fluctuations, in particular, for the case of comparable rates of relaxation and pure dephasing. © 2003 MAIK "Nauka/Interperiodica".

PACS numbers: 03.65.Yz; 75.10.Jm; 74.50.+r; 85.25.Cp

Recent experiments with superconducting Josephson-junction circuits [1, 2] demonstrated quantum coherent oscillations with a long decay time and a quality factor up to ~10^4. These experiments, on one hand, probe coherent properties of Josephson qubits (quantum bits) and demonstrate their potential for applications in quantum computing and quantum communication. On the other hand, they may be viewed as a probe of the noise mechanisms in the devices studied.

For the description of the dynamics of a two-level system (qubit, spin) subject to weak short-correlated noise, one may use the Bloch equation, known from NMR studies, which describes exponential relaxation of the longitudinal spin component and dephasing of the precessing transverse spin component (here and below, we use the spin-1/2 language to discuss the dynamics). This description is valid as long as the correlation time of the noise is short compared to the typical dissipative times T_1, T_2. However, in Josephson-junction qubits, the low-frequency noise is strong. These low-frequency fluctuations are correlated over distant times, and special treatment of their influence on a qubit is needed. They could lead to complicated decay laws [3–6]. In [7], the influence of low-frequency fluctuations nonlinearly coupled to a qubit was analyzed; this analysis is relevant for operation at the so-called optimal operation points [1]. Here, we extend this analysis to account for the effect of transverse fluctuations also present at optimal points. While our discussion applies to an arbitrary dissipative two-level system, for illustration we consider the Josephson charge qubit, similar to that studied in the experiment [1]. We begin by discussing this system and the relevant noise sources, and then proceed to the analysis of dephasing in general and at optimal points.

Dissipative dynamics of a Josephson charge qubit. The simplest Josephson charge qubit is the Cooper-pair box shown in Fig. 1 [8]. It consists of a superconducting island connected by a dc-SQUID (effectively, a Josephson junction with the coupling $E_J(\Phi_x) = 2E_J^0 \cos(\pi\Phi_x/\Phi_0)$ tunable via magnetic flux Φ_x; here, $\Phi_0 = hc/2e$) to a superconducting lead and biased by a gate voltage V_g via a gate capacitor C_g. The Josephson energy of the junctions in the SQUID loop is E_J^0, and their capacitance C_J^0 sets the charging-energy scale $E_C \equiv e^2/2(C_g + C_J)$, $C_J = 2C_J^0$. At low enough temperatures, single-electron tunneling is suppressed and only even-parity states are involved. Here, we consider low-capacitance junctions with high charging energy $E_C \gg E_J^0$. Then, the number n of Cooper pairs on the island (relative to a neutral state) is a good quantum number; at certain values of the bias $V_g \approx V_{\text{deg}} = (2n + 1)e/C$, two lowest charge states n and $n + 1$ are near-degenerate, and even a weak E_J mixes them strongly. At low temperatures and operation frequencies, higher
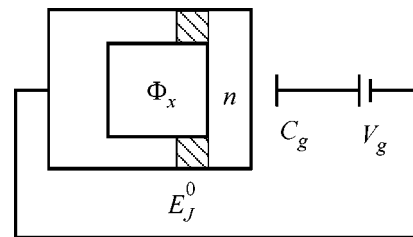

Fig. 1. The simplest Josephson charge qubit.

charge states do not play a role. The Hamiltonian reduces to a two-state model,

$$\mathcal{H} = -\frac{1}{2}[E_{ch}(V_g)\hat{\sigma}_z + E_J(\Phi_x)\hat{\sigma}_x], \qquad (1)$$

in the basis $|\downarrow\rangle = |n\rangle$, $|\uparrow\rangle = |n + 1\rangle$; here, $E_{ch}(V_g) = 2e(V_g - V_{deg})C_g/(C_J + C_g)$. The Hamiltonian (1) can be controlled via the gate voltage V_g and the applied flux Φ_x; this allows one to manipulate the qubit's state and perform quantum logic operations. To read out the final quantum state, one has to couple the qubit to a quantum detector, e.g., a single-electron transistor [8].

Quantum bits are inevitably coupled to fluctuations in the environment (bath). This destroys the coherence of the qubits' dynamics. To slow down the dephasing, the coupling should be made as weak as possible. In solid-state systems, decoherence is potentially strong due to numerous microscopic modes. In Josephson qubits, the noise is dominated by material-dependent sources, such as background-charge fluctuations or variations of magnetic fields and critical currents, with power spectrum peaked at low frequencies, often $1/f$. A further relevant contribution is the electromagnetic noise of the control circuit, typically ohmic at low frequencies. The $1/f$ noise appears difficult to suppress and, since the dephasing is dominated by low-frequency noise, it is particularly destructive. On the other hand, Vion *et al.* [1] showed that the effect of this noise can be substantially reduced by tuning the linear longitudinal qubit-noise coupling to zero (in a modified design; they also suppressed the coupling to the quantum detector to minimize its effect on the qubit before the readout). This increased the coherence time by two–three orders of magnitude compared to earlier experiments.

Of special interest is the analysis of the slow dephasing at such an optimal point. On one hand, comparison of theory and experiment may verify our understanding of the physics of the device studied as a dissipative two-level system. Further, from the analysis of the dephasing time scale and the decay law, one may extract additional information about the statistical properties of the noise. On the other hand, understanding of the dissipative processes should allow their further suppression in future qubit designs.

Part of the noise (including the background-charge fluctuations) can be thought of as fluctuations of the gate voltage, and another part, as fluctuations of the control flux Φ_x. It is convenient to discuss the effect of, e.g., the voltage noise $V_g = V_g^0 + Y(t)$ in the qubit's eigenbasis:

$$\mathcal{H} = -\frac{1}{2}[\Delta E\hat{\sigma}_z + \zeta\hat{Y}(t)(-\sin\eta\,\hat{\sigma}_x + \cos\eta\,\hat{\sigma}_z)], \quad (2)$$

where the level splitting $\Delta E = (E_{ch}(V_g^0)^2 + E_J^2)^{1/2}$ and the angle between the static and fluctuating "magnetic"

fields is given by $\tan\eta = E_J/E_{ch}(V_g^0)$. We expanded the variation of E_{ch} in Y to the linear order. Consider first the effect of weak short-correlated noise (with correlation time shorter than the dissipative times; this includes the finite-temperature ohmic noise). In this case, one can use the lowest-order perturbation theory and finds that the spin dynamics is described by the Bloch equations, known from NMR. The interlevel transitions are induced by the *transverse* fluctuations $\propto\sin\eta$ and give the relaxation time $1/T_1 = \zeta^2\sin^2\eta\,S_Y(\omega = \Delta E)/2$; the dephasing time is $1/T_2 = 1/2T_1 + 1/T_2^*$, where the pure dephasing is induced by the *longitudinal* noise $\propto\cos\eta$ and gives $1/T_2^* = \zeta^2\cos^2\eta\,S_Y(\omega = 0)/2$ (here, the noise power $S_Y(t) = (1/2)\langle[Y(t), Y(0)]_+\rangle$; we set $\hbar = 1$). The effect of the magnetic-flux noise can be analyzed similarly. For Josephson qubits, these expressions give good estimates for the measured relaxation times but do not suffice to describe the dephasing. Indeed, the expression for T_2^* cannot be used for strong longitudinal low-frequency, e.g., $1/f$ noise; still, it indicates that dephasing is strong. In early experiments [4, 9], dephasing times in the range of fractions to a few nanoseconds were achieved. Tuning to an optimal point extended the coherence time to ~ 1 μs [1].

Dephasing at an optimal point. We illustrate our discussion of decoherence at an optimal point by considering a qubit deep in the charge limit, although in the device of [1] E_C and E_J were comparable (in which case two lowest eigenstates, which form the qubit, are no longer charge states). Using two control parameters V_g and Φ_x, one can tune the longitudinal linear couplings to the charge and flux noise to zero. For instance, for the system (2), tuning the gate voltage to the degeneracy point $E_{ch}(V_g^0) = 0$ yields $\cos\eta = 0$. Further, tuning Φ_x to the point of maximal $E_J(\Phi_x)$ also suppresses the linear coupling to the flux fluctuations $\Phi_x = \Phi_x^0 + X(t)$. Thus, at this optimal point, the Hamiltonian reads:

$$\mathcal{H} = -\frac{1}{2}[\Delta E\hat{\sigma}_z + \lambda X^2\hat{\sigma}_z + \zeta Y\hat{\sigma}_x], \qquad (3)$$

where we left only the leading fluctuating terms.

The quadratic longitudinal low-frequency noise $\lambda X^2\hat{\sigma}_z$ may result in an unusual dephasing law (with a power law crossing over to exponential decay) due to strong higher-order contributions [7]. Here, we discuss the effect of the transverse noise $\zeta Y\hat{\sigma}_x$. It can lead to relaxation processes and contribute to pure dephasing in higher orders. Thus, in the analysis of dephasing, one needs to account for both λX^2 and ζY terms.

The effect of the low-frequency ($\omega \ll \Delta E$) transverse noise can be treated in the adiabatic approximation: we

diagonalize (3) to $-\hat{\sigma}_z\sqrt{(\Delta E + \lambda X^2)^2 + (\zeta Y)^2}/2 \approx$ $-\hat{\sigma}_z[\Delta E + \lambda X^2 + \zeta^2 X^2/(2\Delta E)]/2$, thus the low-$\omega$ transverse noise contributes to pure dephasing. In general, higher-frequency fluctuations are also present and induce relaxation. If the relaxation is much slower than the pure dephasing, one may neglect its contribution to the total dephasing. If the relaxation is much faster, it dominates the decoherence; in this limit, its rate $\zeta^2 S_Y(\Delta E)/2$ is given by the golden rule. However, of special experimental interest [1] is the situation with comparable relaxation and pure-dephasing time scales. We analyze whether evaluation of each of them is influenced by the other in this case, that is whether the low- and high-ω contributions interfere. In particular, we expect [7] strong higher-order contributions to the pure dephasing due to strong low-ω noise. Does it also contribute to relaxation? In the lowest order, the relaxation is due to transitions with emission of a single resonant bath excitation; can instead a near-resonant excitation be emitted accompanied by low-frequency excitations? Here, we show how the dephasing and relaxation laws and time scales can be obtained.

Dephasing by transverse noise. We begin with a discussion of purely transverse noise, $\lambda = 0$. We focus on the long-correlated noise (slow decay of $\langle Y(0)Y(t)\rangle$), i.e., on the noise power peaked at low and smooth at high frequencies. In our analysis, below we assume weak dissipation: pure dephasing and relaxation slower than the oscillations $\Gamma \ll \Delta E$, where Γ represents the total-dephasing time scale. This limit is of primary interest for the circuits that realize qubits. In addition, for illustration below we consider a source of Gaussian noise $Y(t)$, which can be characterized by its second correlator, but our major conclusions persist in more general situations.

Our discussion is based on the analysis of the evolution operator of the qubit dynamics using the "real-time" Keldysh diagrammatic expansion in the qubit-bath coupling (this approach [10] is useful, since the spin degree of freedom does not satisfy the Wick theorem; it reminds the approach of [11]). We begin by showing that the subleading-order effects of the low-frequency transverse noise reduce to the lowest-order contribution of longitudinal quadratic noise (this can also be seen from the adiabatic approximation, but our derivation indicates the diagrams important in the discussion below).

In the diagrams, the horizontal direction explicitly represents the time axis. The solid lines describe the unperturbed (here, coherent) evolution of the qubit's 2×2 density matrix $\hat{\rho}$, $\exp(-iL_0 t)\theta(t)$, where L_0 is the bare Liouville operator (this translates to $1/(\omega - iL_0)$ in the frequency domain). The vertices are explicitly time-ordered; each of them contributes the term $\zeta Y \sigma_x \tau_z/2$, with the bath operator $Y(t)$ and the Keldysh matrix $\tau_z = \pm 1$ for vertices on the upper/lower time branch.
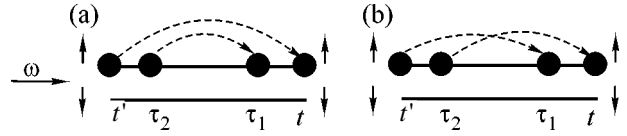
Fig. 2. Second-order contributions to the self-energy $\Sigma_{\uparrow\downarrow\leftarrow\uparrow\downarrow}$. Other terms are obtained by shifting an even number of the vertices in (a) or (b) to the lower branch.

Averaging over the fluctuations should be performed; for Gaussian correlations, it pairs the vertices as indicated by dashed lines in Fig. 2, each of the lines corresponding to a correlator $\langle YY\rangle$. Figure 2 shows contributions to the second-order self-energy $\Sigma_{\uparrow\downarrow\leftarrow\uparrow\downarrow}^{(2)}$ (here, $ij = \uparrow\downarrow$ label four entries of the qubit's density matrix). The term in Fig. 2a gives

$$\left(\frac{\zeta}{2}\right)^4 \int d\tau_1 d\tau_2 \langle Y(t)Y(t')\rangle \langle Y(\tau_1)Y(\tau_2)\rangle e^{i\Delta E(\tau_1 - \tau_2)}, \quad (4)$$

with integration over the domain $t' < \tau_2 < \tau_1 < t$.

After the summation over vertex positions on the lower/upper branches in Figs. 2a and 2b, we evaluate the behavior of the Fourier-transformed self-energy in the vicinity of the level splitting, at $\omega = -\Delta E - \omega' + i0$, where $\omega' \ll \Delta E$. If the integral is dominated by low frequencies, we find:

$$\mathrm{Re}\Sigma_{\uparrow\downarrow\leftarrow\uparrow\downarrow}^{(2)}(\omega = -\Delta E - \omega' + i0) \approx -\frac{\zeta^4}{8\Delta E^2}\int\frac{d\nu}{2\pi}$$
$$\times [\langle Y_{\nu+\omega'}^2\rangle\langle Y_{-\nu}^2\rangle + \langle Y_{\nu-\omega'}^2\rangle\langle Y_{-\nu}^2\rangle] = -\frac{1}{2}S_{Y_2}(\omega'), \quad (5)$$

where S_{Y_2} is the noise of

$$Y_2 \equiv \zeta^2 Y^2/(2\Delta E). \quad (6)$$

The result (5) coincides, as expected, with the lowest-order contribution of the term $-Y_2\sigma_z/2$; note that the left and right vertex pairs in Fig. 2 can be viewed as composite vertices corresponding to $-Y_2\sigma_z/2$. Below, we demonstrate that similar reduction occurs in every order of the perturbative expansion. Specifically, we show that the decay of the off-diagonal entry of the density matrix is $\rho_{\uparrow\downarrow}(t) = \rho_{\uparrow\downarrow}(0)\exp(-t/2T_1)\gamma_\varphi(t)$, where the relaxation time is given by the golden rule and the pure dephasing term $\gamma_\varphi(t)$ is the same as for the longitudinal fluctuations $-Y_2\sigma_z/2$ (analyzed in [7]).

To demonstrate this, we consider the diagrammatic calculation of the evolution operator for the density matrix. We begin by evaluating the evolution of the off-diagonal entry $\rho_\downarrow^\uparrow$ (the phase dynamics and dephasing), and then discuss relaxation (evolution of $\rho_\uparrow^\uparrow$, $\rho_\downarrow^\downarrow$).
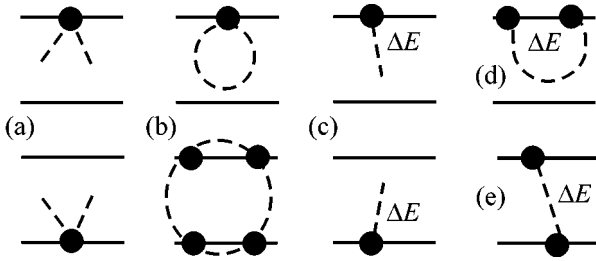
Fig. 3. (a) Double vertices with low-ω tails, which appear in the evaluation of dephasing. (b) Examples of clusters built out of them [7]. (c) A low-ω object with a high-frequency dashed line. The relaxation process in (e) also contributes to dephasing as shown in (d).

The expansion of the propagator contains vertices on the horizontal solid lines representing the Keldysh contour. For a given number and ordering of the vertices, one is to integrate over their time positions, and then add up all diagrams. Consider the dependence of the integrand on the time position of a vertex. This dependence includes fast oscillations with frequency $\pm\Delta E$, since the vertex flips the spin and changes the energy of the bare Hamiltonian $-\Delta E \sigma_z/2$, and a much slower dependence of the dashed line. Thus, the integrand is a fast oscillating function of the time positions of each vertex. Since integration is typically performed over a time range much wider than the period of oscillations (at all times of interest for the analysis of dephasing; this range is $\sim 1/\Gamma$ at $t \sim 1/\Gamma$), the contribution for the most part of the integration space (with vertices' time positions as coordinates) is strongly suppressed by fast oscillations. However, in certain directions in this space, in which pairs of vertices with opposite oscillation frequencies $\pm\Delta E$ move together, the variation is slow, and the respective domains dominate the integral. One can arrive at this conclusion, and determine the dominant domains, by considering the evaluation of a particular diagram: the integral over the time t of a vertex $\int_a^b g(t) \exp(i\Delta Et)dt$ is taken between the positions a and b of the neighboring vertices. Since $g(t)$ is slow on scale $1/\Delta E$, the oscillatory integral is dominated by the boundary terms, $g(t)\exp(i\Delta Et)|_a^b / i\Delta E$. One can say that the vertex t joins one of its neighbors, and later one integrates over the vertex-pair position, a or b.

One can continue this process, integrating at each step over time positions of unpaired vertices (or clusters with an odd number of vertices and, hence, oscillatory behavior), if any are still present. Finally, one arrives at a situation where all vertices are paired, and the dependence of the integrand on pair time positions is slow (the exponentials $\exp(\pm i\Delta Et)$ for two paired vertices compensate each other). The integral in each domain with a fixed time ordering is dominated by the bound-

ary terms, that is, the terms with paired vertices. Thus, we eliminate the high-frequency ($\sim\Delta E$) behavior, and now can evaluate the propagators using the diagram technique with ingredients that are slow (without oscillatory dependence on their time position): "double" vertices with two dashed tails in Fig. 3a and dashed lines connecting these tails (cf. the examples in Fig. 3b). Although four-, six-, and, further, $2n$-fold clusters also form slow objects—their creation requires additional constraints on the vertex times (compared to building n pairs) and the respective integration domain is much smaller; thus, the contribution of such clusters is of higher order in $\Gamma/\Delta E$.

A closer inspection of the spin dependence and the Keldysh two-branch structure reveals that, in each pair, the vertices are located either both on the upper or on the lower branch (for vertices located on different branches, two terms with different time orderings cancel each other unless the vertices are linked by a dashed line; such a term appears in the analysis of relaxation but not of dephasing), and they indeed effectively correspond to the term $-Y_2\sigma_z/2$ in the Hamiltonian.

So far, we have constructed slow composite objects paying attention only to the oscillations of the solid lines in the diagrams and assuming very slow dashed lines, i.e., neglected the higher-frequency noise. In fact, one can construct another slow object shown in Fig. 3c, if the respective oscillations of the solid lines are compensated by the dashed line from this vertex. In other words, in the frequency domain, one constrains the frequency of the dashed line to be ΔE (or $-\Delta E$, depending on the direction of the spin flip at the vertex). The dashed lines from such objects pair up, and the integral with respect to their relative position is dominated by small separations, $\delta t \sim 1/\Delta E$. Thus, one finds the slow object of Fig. 3d: two vertices linked by a dashed line at frequency ΔE, which describes the relaxational contribution to dephasing $\exp(-t/2T_1)$, where

$$1/T_1 = \zeta^2 S_Y(\Delta E)/2. \qquad (7)$$

In similar clusters of higher order additional constraints strongly limit the integration domain. Note that the object in Fig. 3d involves weak noise at a high frequency ΔE, unlike those in Fig. 3a, but it is still relevant since the lowest-order term in the upper part of Fig. 3b is imaginary and does not contribute to dephasing.

Similarly, we analyze the relaxation of the diagonal entries $\rho_\uparrow^\uparrow$, $\rho_\downarrow^\downarrow$. The new slow ingredient in this analysis is shown in Fig. 3e. As for the composite objects in Fig. 3a, the terms with these objects located on the upper and lower branches cancel each other, due to different signs ascribed to them in the Keldysh formalism (in contrast, in the analysis of the evolution of $\rho_\downarrow^\uparrow$, displacing a vertex from one branch to the other flips the spin thus yielding an additional sign change rather than cancellation). Hence, the relaxation is given by the terms in Figs. 3d and 3e and Eq. (7). We find that the

strong low-frequency noise does not influence the relaxation rate.

Discussion. We focused on the effect of the purely transverse noise. One can verify that, in the presence of the longitudinal fluctuations $-\lambda X^2 \sigma_z/2$, the reduction persists: the relaxation is still given by Eq. (7), and the dephasing can be found by considering the longitudinal noise $-[\lambda X^2 + \zeta^2 Y^2/2\Delta E]\sigma_z/2$. For uncorrelated fluctuations $X(t)$ and $Y(t)$, their effects just add up (this would happen in the charge limit $E_C \gg E_J$ for the qubit in Fig. 1 at the degeneracy point, where the charge noise is transverse, and at the proper flux bias, where the flux noise is quadratic longitudinal). In the experiment [1], E_C and E_J were comparable; hence, both charge and flux noise contributed to longitudinal and transverse fluctuations making them correlated. This should be taken into account but does not complicate the analysis.

We considered slow fluctuations. For short-correlated noise, the double vertices of Fig. 3a do not contribute, and one recovers the Bloch equations.

Furthermore, we illustrated our analysis by an example of Gaussian noise. Such fluctuations are indeed encountered: The low-frequency noise, e.g., the background-charge fluctuations in Josephson circuits, is possibly produced by a collection of bistable fluctuators (or a discrete system with more states). With a proper wide distribution of their parameters (couplings to the qubit, switching rates), they produce a smooth $1/f$ noise power. If the qubit is affected by many fluctuators, with a dense distribution in the parameter space, due to the central limit theorem, one expects Gaussian noise. In some Josephson devices, sharp noise features indicate that a few fluctuators dominate and the resulting noise is non-Gaussian (dephasing by such fluctuators was studied, e.g., in [6]). We emphasize that our reduction applies also to the analysis of these systems. Indeed, our derivation used only the fact that the fluctuations are slow. Thus, one can still build the diagrams from the slow objects constructed above, but for non-Gaussian fluctuations, the dashed tails of the vertices may join not in pairs but also in larger bunches. After

the reduction to quadratic longitudinal noise, one may use other, nondiagrammatic, ways to analyze its effect.

Our results are relevant for the analysis of the experiment of [1], in which the measured relaxation and dephasing times were comparable. The prediction of a specific decay law requires a detailed knowledge of the noise power of charge and flux fluctuations. It can be acquired via measurements away from the optimal point, as indicated in [1].

REFERENCES

1. D. Vion, A. Aassime, A. Cottet, *et al.*, Science **296**, 886 (2002).
2. I. Chiorescu, Y. Nakamura, C. J. P. M. Harmans, and J. E. Mooij, Science **299**, 1869 (2003); Y. Yu, S. Han, X. Chu, *et al.*, Science **296**, 889 (2002); J. M. Martinis, S. Nam, J. Aumentado, and C. Urbina, Phys. Rev. Lett. **89**, 117901 (2002); Yu. A. Pashkin, T. Yamamoto, O. Astafiev, *et al.*, Nature **421**, 823 (2003).
3. A. Cottet, A. Steinbach, P. Joyez, *et al.*, in *Macroscopic Quantum Coherence and Quantum Computing*, Ed. by D. V. Averin *et al.* (Kluwer/Plenum, New York, 2001), p. 111.
4. Y. Nakamura, Yu. A. Pashkin, T. Yamamoto, and J. S. Tsai, Phys. Rev. Lett. **88**, 047901 (2002).
5. A. Shnirman, Yu. Makhlin, and G. Schön, Phys. Scr. T **102**, 147 (2002).
6. E. Paladino, L. Faoro, G. Falci, and R. Fazio, Phys. Rev. Lett. **88**, 228304 (2002).
7. Yu. Makhlin and A. Shnirman, cond-mat/0308297.
8. Yu. Makhlin, G. Schön, and A. Shnirman, Rev. Mod. Phys. **73**, 357 (2001), and references therein.
9. Y. Nakamura, Yu. A. Pashkin, and J. S. Tsai, Nature **398**, 786 (1999).
10. H. Schoeller and G. Schön, Phys. Rev. B **50**, 18436 (1994).
11. O. V. Konstantinov and V. I. Perel, Zh. Éksp. Teor. Fiz. **39**, 197 (1961) [Sov. Phys. JETP **12**, 142 (1961)].

Low-Frequency Structural Plasma Turbulence in the L-2M Stellarator

G. M. Batanov*, V. E. Bening**, V. Yu. Korolev**, A. E. Petrov*, A. A. Pshenichnikov*,
K. A. Sarksyan*, N. N. Skvortsova*, N. K. Kharchev*, and Yu. V. Kholnov*

**Prokhorov Institute of General Physics, Russian Academy of Sciences, ul. Vavilova 38, Moscow, 119991 Russia*
e-mail: nina@fpl.gpi.ru
***Moscow State University, Vorob'evy gory, Moscow, 119899 Russia*
Received September 17, 2003

Experiments on the L-2M stellarator have shown the occurrence of steady-state low-frequency strong structural (LFSS) turbulence throughout the entire plasma column. A key feature of LFSS turbulence is the presence of stochastic plasma structures. It is shown that different types of LFSS turbulence are correlated throughout the entire plasma volume. Stable non-Gaussian probability density distributions of all of the fluctuating plasma parameters are measured. The characteristic spatial and time scales of LFSS turbulence, which is responsible for non-Brownian diffusion in plasma, are determined. © *2003 MAIK "Nauka/Interperiodica".*

PACS numbers: 52.35.Ra; 52.55.Hc

1. INTRODUCTION

In recent years, low-frequency (LF) plasma turbulence in closed magnetic confinement systems has attracted considerable interest of plasma physicists. The 2003 EPS conference has demonstrated that experimental research of this kind is presently being carried out in all of the existing tokamaks and stellarators: T-10, LHD, TJ-II, DIII-D, JET, etc. (see [1], report nos. P-2.56, P-3.121, P-4.5, O-2.1A, and P-120). A reason for increased interest in LF turbulence is that many experimental facts directly indicate its influence on the macroscopic plasma parameters in closed magnetic confinement systems. For example, LF turbulence governs anomalous transport in the edge plasma [2, 3], a change in the parameters of turbulence correlates with observations of internal and peripheral transport barriers in plasma [4, 5], and the statistical parameters of the edge turbulent flux serve as indicators of the state of the chamber wall [6]. Another reason for a particular interest in the nature of LF turbulence is the problem of evaluating the frequency with which rare large-amplitude events (of a "catastrophic" type) occur in devices with long-duration or steady-state discharges [7]. The last reason, in our opinion, is that modern, computerized data acquisition systems made it possible to process long data arrays (temporal and spatial samples) of the fluctuating parameters, which are then used to calculate the transient and steady-state spectral, correlation, probabilistic, dimensional, and other characteristics of LF plasma turbulence.

The L-2M stellarator was among the first toroidal magnetic confinement systems in which LF turbulence in a steady-state phase of the discharge was proposed to be studied by the methods of numerical data analysis.

In 1989, a report on the general characteristics of two types of LF turbulence was presented [8]. These types of turbulence were initiated by different plasma instabilities in the L-2M stellarator and the TAU-1 model linear device. Further studies of LF plasma turbulence resulted in the fact that a specific turbulent state was identified by analyzing the characteristics of turbulence in the TAU-1 device. In [9], this state was called LF structural turbulence. This is a determinate–chaotic turbulent state in which ensembles of stochastic plasma structures are present. These structures determine a number of spectral, correlation, and probabilistic parameters of turbulence. In the present paper, we describe LF structural plasma turbulence observed in the L-2M stellarator.

2. DESCRIPTION OF THE DEVICE AND DIAGNOSTIC TECHNIQUES

The L-2M stellarator is an $l = 2$ stellarator [10]. The major radius of the torus is $R = 100$ cm, and the mean plasma radius is $\langle r \rangle = 11.5$ cm. The plasma was created and heated by one or two gyrotrons under electron-cyclotron resonance conditions at the second harmonic of the electron gyrofrequency (the magnetic field at the plasma center was $B = 1.3$–1.4 T). The gyrotron radiation power was $P_0 = 150$–300 kW, and the duration of the microwave pulse was up to 15 ms. Measurements were carried out in a hydrogen plasma with an average density of $\langle n \rangle = (0.8$–$2.0) \times 10^{13}$ cm^{-3} and a central temperature of $T_e(0) = 0.6$–1.0 keV. In the edge plasma (at a radius of $r/r_s = 0.9$, where r_s is the mean separatrix radius), the density was $n = (1$–$2) \times 10^{12}$ cm^{-3}, and the electron temperature was $T_e = 30$–40 eV. The duration

Table

Diagnostics	Location of the measuring region	Measured fluctuations	Number of channels	Wavenumber k of fluctuations
Gyrotron radiation scattering	Heating region (high-temperature plasma)	Plasma density	2	$20\ cm^{-1}$ $40\ cm^{-1}$
2-mm scattering	High-temperature plasma outside the heating region	Plasma density	3	$6\ cm^{-1}$ $9\ cm^{-1}$ $13\ cm^{-1}$
Langmuir probes	Edge plasma	1. Plasma density 2. Potential 3. Particle flux	up to 15	Broad spectrum
Magnetic probes	Outside the plasma	Magnetic field	up to 9	Broad spectrum

of the steady-state phase of the L-2M discharge was 10 ms.

It is well known that, in a thermodynamic sense, a toroidal magnetic confinement device is an open plasma system. All of the various types of steady-state plasma fluctuations that are studied under the conditions of dynamical equilibrium have an energy source and energy sink. There can also exist plasma regions in which energy is redistributed between different turbulent states. For this reason, when experimentally studying plasma fluctuations, it is important that these constituents of plasma turbulence could be changed by varying some parameters of the device: the heating power, the magnetic configuration (the rotational transform), and the state of the chamber wall (the intensity of gas flux from the wall). The L-2M stellarator meets these requirements. The plasma heating power can be varied by varying the gyrotron power. Five different configurations of the magnetic field (with a rotational transform at the axes of 0.175, 0.119, 0.082, 0.064, and 0.043) can be created in the device. In addition, by applying a weak magnetic field transverse to the stellarator plane ($B_v = \pm 20$, 40, or 70 G), it is possible to shift the magnetic axis along the major radius of the torus [11]. The properties of the first wall depend on the method of its cleaning. Along with the baking of the vacuum chamber, an inductive discharge in hydrogen, a glow discharge in helium, or the boronization of the chamber are employed. A graphite limiter can also be used.

In L-2M, fluctuations were measured in several poloidal sections throughout the entire plasma column (from the heating region to the separatrix). All the diagnostics used to measure fluctuations are listed in the table. As an illustration, Fig. 1 schematically shows the arrangement of the diagnostics in one poloidal section. Plasma density fluctuations in the heating region were measured by the scattering of the heating gyrotron radiation [12, 13]. Density fluctuations of the high-temperature plasma in the region shifted in the radial and toroidal directions from the heating region were measured by the scattering of 2-mm probing microwaves [14, 15].

Fluctuations of the density, potential, electric field, and particle flux in the edge plasma were measured by Langmuir probes of different design in several sections along the torus [10]. Fluctuations of the magnetic field outside the separatrix were measured by magnetic probes [17]. The results of measurements from all the diagnostics were unified arrays of the fluctuating amplitudes in the form of time samples to which the same program package for the numerical evaluation could be applied. The length of some samples was up to 256 thousands of readings, the number of simultaneously taken samples was up to 20, and the sampling rate was from 0.1 to 40 MHz. The program package included the multidimensional spectral Fourier analysis; the correlation analysis [18, 19]; the spectral and coherent wavelet analysis [20–23]; the drawing of histograms; the calculation of the moments of random values; and other supplementary programs for smoothing, filtering, and averaging the signals.
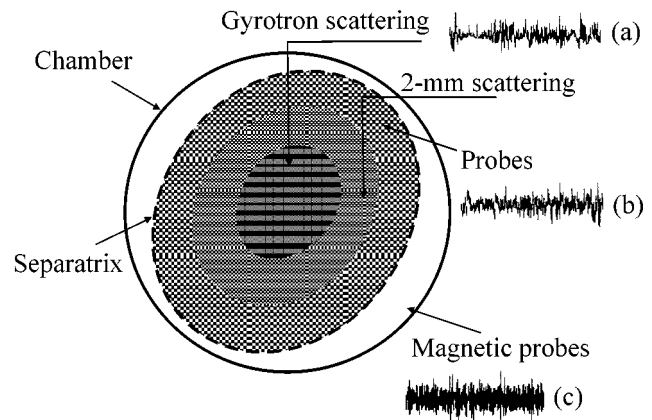

Fig. 1. Arrangement of diagnostics and time samples of the magnitudes of (a) density fluctuations in the high-temperature plasma, (b) potential fluctuations in the low-temperature edge plasma, and (c) magnetic-field fluctuations outside the plasma. The frequencies below 1 kHz are filtered.
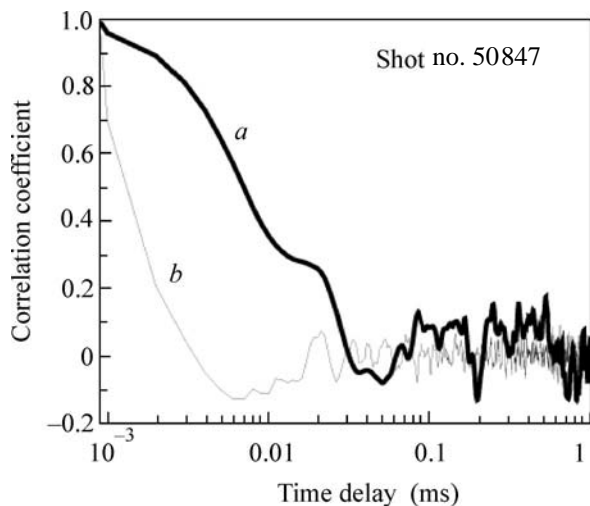
Fig. 2. ACFs of density fluctuations (a) in the central region and (b) near the plasma edge.

3. RESULTS OF STUDIES

LF fluctuations are naturally present throughout the entire plasma column of the L-2M stellarator—from the center to the boundary. In this paper, we only consider the general features of fluctuations regardless of their localization in the plasma column. Figure 1 shows the time samples of the magnitudes of (a) density fluctuations in the high-temperature plasma in the heating region, (b) potential fluctuations in the low-temperature edge plasma, and (c) fluctuations of the magnetic field outside the plasma. In all three samples, frequencies below 1 kHz are filtered out. We note that the time behavior of other signals that were measured in the experiment and are listed in the table is similar to the signals presented in Fig. 1 [10, 13, 16]. The time samples consist of bursts of different durations and pauses between them. Observations showed that both the signal frequency within the bursts and the rise and decay times of the signals in the bursts varied.[1] The level of fluctuations was fairly large as compared to the average values of the corresponding parameters. The minimum relative fluctuation level was observed for the magnetic field $\tilde{B}/B \sim 5 \times 10^{-5}$. The level of density fluctuations inside the plasma column was substantially higher: from 20–30% ($\tilde{n}/n \sim 0.2$–0.3) in the edge plasma to 10% ($\tilde{n}/n \sim 0.1$) in the central region. The level of potential and electric field fluctuations in the edge plasma was 10–20% ($\tilde{\varphi}/\varphi \sim 0.1$–0.2).

The autocorrelation functions (ACFs) of time samples of LF turbulent fluctuations in the L-2M consist of two components: a finite-width (rather than a δ-shaped) maximum and a slowly decreasing tail with repetitive bursts [8, 13–15, 23]. Figure 2 shows ACFs of density fluctuations in the central and edge plasmas. The long-

term components of the ACF usually comprise up to 10–30% of the energy of the density, potential, magnetic-field, and electric-field fluctuations (the noise level in these measurements usually does not exceed 1–2%). Correlation analysis of weak-turbulence signals shows that they are characterized by a slowly decreasing ACF, so that the characteristic autocorrelation time is much longer than the oscillation period. In the case of strong turbulence, fluctuation signals are characterized by a rapid decrease in the ACF and the autocorrelation time does not exceed the oscillation period. In experiments, these two turbulent states can easily be distinguished by the ACF shape. Hence, the measured ACFs indicate, on the one hand, a strongly turbulent character of fluctuations and, on the other hand, the presence of long-term correlated components in this turbulence.

However, the Fourier spectra of the same fluctuations are uniform and, as a rule, do not contain harmonics [10, 14, 24]. Figure 3a shows a Fourier spectrum of plasma density fluctuations in the central region of the plasma column. It can be seen that the spectrum is noisy in character. Only for certain magnetic configurations, diffuse harmonics can be observed in the Fourier spectra of magnetic-field fluctuations outside the plasma column (Fig. 3b). Therefore, Fourier analysis is inadequate for describing bursty signals because long-term correlations do not manifest themselves in continuous Fourier spectra and the fine structure of the spectra remains unresolved.

A more adequate description of the frequency spectra of bursty signals is provided by wavelet analysis, in which a signal under study is represented as a superposition of finite-duration wavelets.[2] Wavelet analysis turns out to be very convenient when analyzing signals containing bursts, fast frequency variations, and short-term events. Therefore, this analysis can be useful when examining signals from strongly turbulent plasma. In our experiments, fluctuations were analyzed using Gaussian wavelets [22, 23]. A wavelet spectrum of density fluctuations in the edge plasma is shown in Fig. 3c. In this spectrum, quasi-harmonics corresponding to long-term ACF components are clearly seen. Similar wavelet spectra with quasi-harmonics were obtained for all of the measured fluctuations in L-2M. Using wavelet spectra (instead of Fourier spectra), we could study the spatial-coherence parameters of turbulence on short time intervals and trace the behavior of individual bursts or their ensembles. This allowed us to determine the spatial scales of turbulent fluctuations. Figure 4a shows the wavelet-coherence coefficient between density fluctuations measured at two points separated by 2 mm in the radial (solid line) and poloidal (dashed line) directions [10]. It can be seen that the wavelet-coherence coefficient is anisotropic. In the poloidal direction, this is about 60% for wavelets of any

---

[1] At present, such signals are referred to as "burst-type" signals.

[2] We recall that the wavelet frequency ω is related to the wavelet duration Δ by the formula $\omega = 2\pi/\Delta$.

duration. In the radial direction, this coefficient reaches such a level only for short wavelets and decreases sharply for long wavelets. As the distance between the probes increases, the coherence coefficient decreases more rapidly in the radial direction. In such a way, we measured the characteristic spatial scale of individual pulsations. It turned out to be up to 4 mm in the radial direction (the minimum spatial scale in this direction could not be determined because the probe diameter was 1 mm) and varied from 4–7 mm to 12–20 cm in the poloidal direction. The radial velocity of some structures attained 4×10^6 cm/s. The toroidal coherence coefficient could be reliably measured only in the regime with a boronized chamber wall, when the gas flux from the wall (this flux is also stochastic in character) was minimum.[3] Figure 4b shows the time behavior of the toroidal wavelet-coherence coefficient, which reached a level of 30–70% in some time intervals for density fluctuations in the frequency range 25–150 kHz. The amplitude of the wavelet-coherence coefficient is shown by gray shading. The observation time is plotted on the abscissa, and the wavelet frequency is plotted on the ordinate. In this figure, the intermittent character of the wavelet coherence is clearly seen. Irregularly emerging structures with a large poloidal size are extended in the toroidal direction. Thus, we can conclude that stochastic poloidal structures are present in the edge plasma [6, 24].

The time evolution of the cross-coherence spectrum of density fluctuations in the central (heating) region and in the edge plasma is shown in Fig. 5a (in the same figure, a noise spectrum is also shown).[4] The time evolution of the cross-coherence spectrum is obtained by interpolating individual spectra calculated on 0.5-ms intervals. The amplitude of the cross-coherence coefficient is shown by gray shading. The observation time is plotted on the abscissa, and the wavelet frequency is plotted on the ordinate. For frequencies below 100–200 kHz, the cross-correlation coefficient attains 50% [13, 26]. These measurements can be supplemented by the cross-coherence wavelet spectra of potential fluctuations in the edge plasma and magnetic-field fluctuations outside the plasma column (Fig. 5b). It can be seen that, in this case, the cross-coherence coefficient reaches fairly high values for the same frequencies. This result, however, does not imply that the stochastic structures existing in the central region are of the same nature as the extended poloidal structures in the edge plasma. Various plasma instabilities can be responsible for the onset of LF turbulent fluctuations in the plasma: in the central region of the plasma column, this may be due to instability driven by trapped electrons and drift-

---

[3] In [25], it was demonstrated that, as the gas flux from the chamber wall increases, the radial electric field E_r in the edge plasma under study ($0.75 < r/r_s < 1$) decreases. At the same time, the probability of the formation (and, consequently, observation) of stochastic structures decreases.

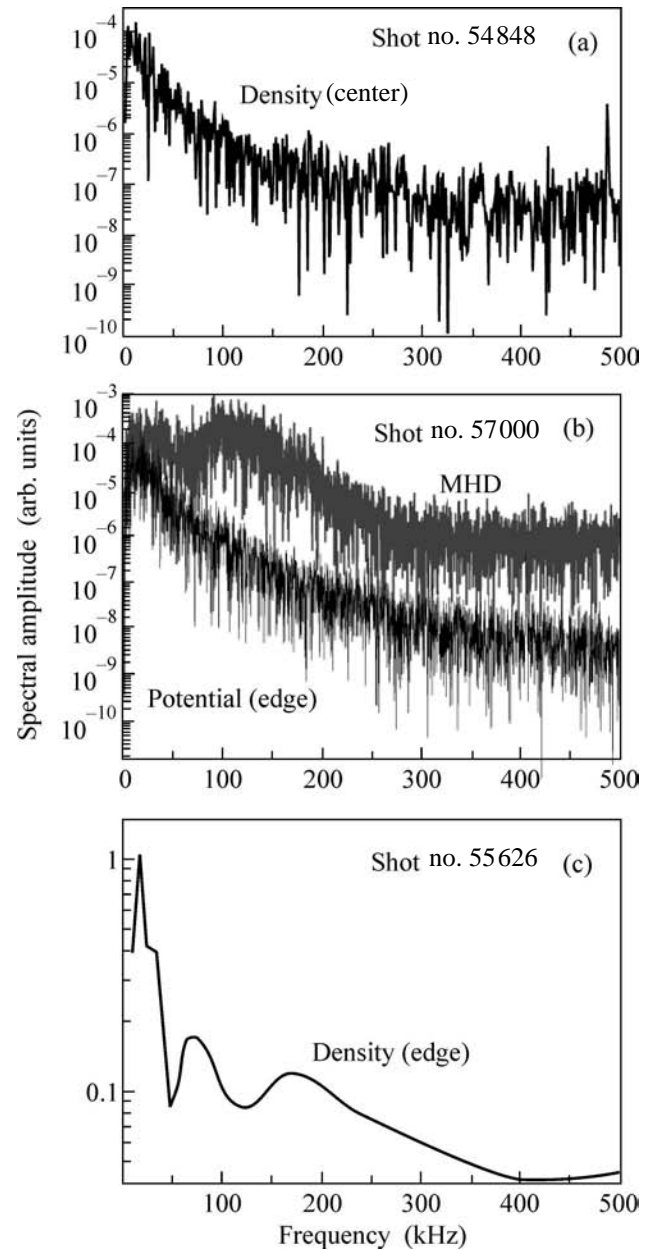[4] The background wavelet spectrum is obtained using two signals measured in different shots.

Fig. 3. (a) Fourier spectrum of density fluctuations in the central region, (b) Fourier spectra of potential fluctuations in the edge plasma and magnetic-field fluctuations outside the plasma (in a discharge with a graphite limiter and a vertical field of $B = -20$ G), and (c) wavelet spectrum of density fluctuations in the edge plasma.

dissipative instability related to the difference in the relative radial density and temperature gradients [13, 27, 28], whereas in the edge plasma, this may be due to the onset of unstable resistive ballooning MHD modes [10, 29]. MHD structures can arise in the edge plasma, whereas drift vortices can appear deeper in the plasma [15, 24]. In the heating region, the nature of the structures cannot yet be identified even hypothetically. Previously, it was shown that interrelations between turbu-
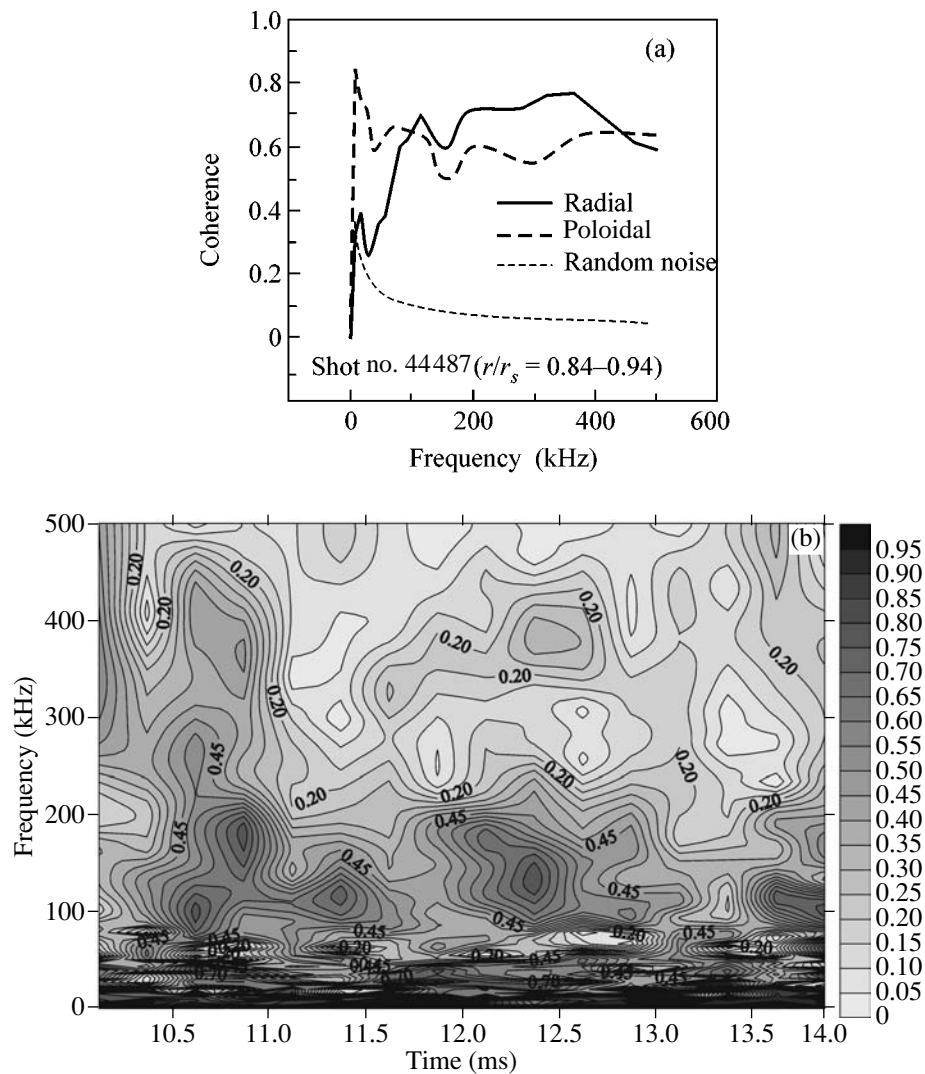
Fig. 4. (a) Wavelet-coherence coefficient between plasma density fluctuations measured at two points separated by 2 mm in the poloidal and radial directions in the edge plasma. (b) Time evolution of the toroidal coherence coefficient of fluctuations in the edge plasma.

lent fluctuations in different types of LF structural turbulence are due to the mutual influence of ensembles of various stochastic structures [30]. The high cross-correlation coefficient of LF fluctuations, which is probably attributed to ensembles of the corresponding stochastic structures, shows that these structures occupy the entire plasma column.

Important characteristics of LF turbulent fluctuations are the probability density function (PDF) of the measured random values [6, 10–13, 24, 31–34]. Figure 6 shows the PDFs of the magnitudes of density fluctuations in the central region (*a*) and near the plasma edge (*b*). The signal magnitude is plotted on the abscissa, and the number of counts is plotted on the ordinate. In each case, the total number of counts is 2000. For plasma density fluctuations in the central region, the shape of the histogram differs markedly from Gaussian by a

sharper vertex and heavier tails (the third and fourth moments are $m_3 = 0.9$ and $m_4 = 8.2$, respectively) and is consistent with the shape of an ACF with a long-term component. The probability of events with large signal magnitudes in this type of turbulence far exceeds the probability of the occurrence of such events for fluctuations described by a Gaussian PDF. As a rule, in toroidal magnetic systems, the PDFs of fluctuations measured far from the energy source and sink differ from a Gaussian PDF by heavier self-similar tails only [34]. To study the self-similar tails of these PDFs, it is necessary that the time sample consist of more than 10^4 points. However, the duration of the steady-state phase of the L-2M discharge is insufficiently long for such an analysis. The question of whether the PDF of density fluctuations in the edge plasma (Fig. 6, histogram *b*) can be

(a)

Fig. 6. PDFs of time samples of density fluctuations (*a*) in the central region and (*b*) near the plasma edge.
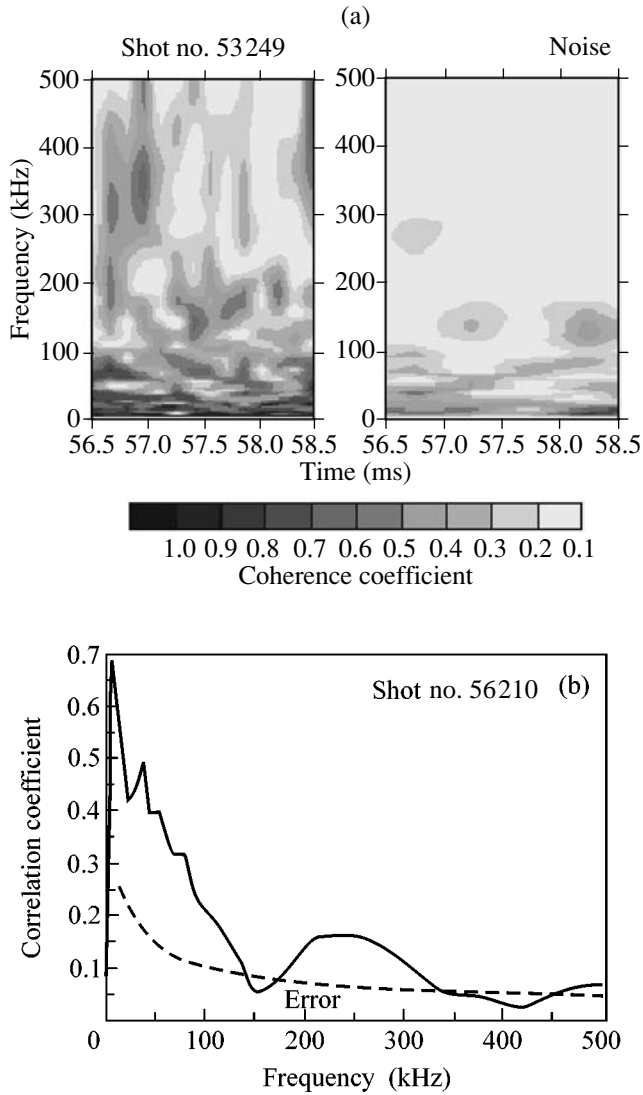

Fig. 5. (a) Time evolution of the cross-coherence spectrum between density fluctuations in the central (heating) region and near the plasma edge (a noise spectrum is also shown). (b) The coherence spectrum between potential fluctuations in the edge plasma and magnetic-field fluctuations outside the plasma.

described by a self-similar distribution with $m_3 = 0.05$ and $m_4 = 3.2$ still remains open.

The difference from a Gaussian PDF is most pronounced for PDFs of fluctuations of the local particle flux in the low-temperature edge plasma of L-2M [31–33]. In the experiment, the local particle flux $\tilde{\Gamma} = \langle \delta n_e \delta v_r \rangle$ was determined from three-pin probe measurements [10]. Here, δn_e is the fluctuating plasma density, $\delta v_r = \delta E_\Theta / B$ is the fluctuating radial velocity, $\delta E_\Theta = (\delta \varphi_1 - \delta \varphi_2)/r \Delta \Theta$ is the fluctuating poloidal electric field, $\delta \varphi$ is the fluctuating plasma floating potential, and Θ is the poloidal angle. Figure 7a shows the ACFs
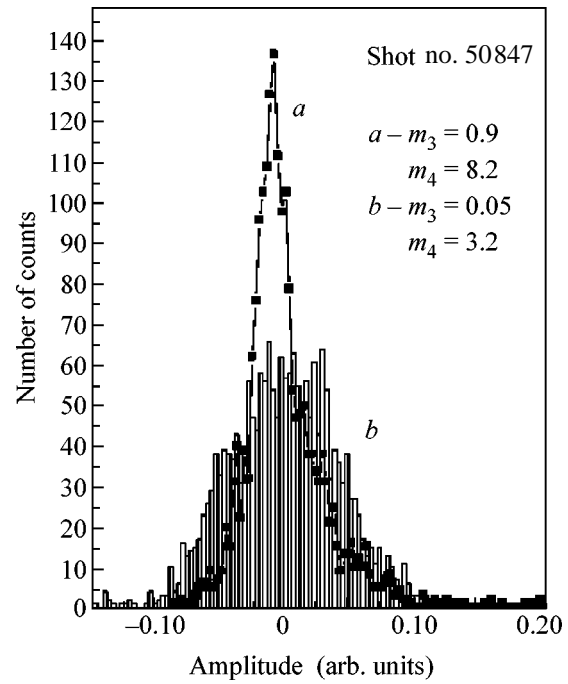
of time samples of the flux and its increments.[5] The first step in studying the PDF of the local flux magnitudes in L-2M is the analysis of the PDF of the flux increments. The point is that the magnitudes of the original process at successive instants of time do not make up a homogeneous and independent sample because of the specific shape of the ACF. From such samples, it is very difficult to draw inference about the probabilistic–statistical properties of the process under study. At the same time, the statistical analysis of the increments of the fluctuating flux on disjoint time intervals shows that their PDFs are identical. Figures 7b and 7c show the PDFs of the flux and its increments in the edge plasma of L-2M. One can see that the PDFs of both the magnitudes and increments of turbulent fluxes differ from normal distributions. The local turbulent flux in L-2M was shown to be a doubly stochastic diffusion process (or, what is formally the same, a diffusion process with random time).[6] The probability density distributions of the increments of these processes are scale mixtures of Gaussian distributions; in our case, this is confirmed by the statistical analysis of time samples of the flux incre-

---

[5] The time sample of the increments $\Delta \tilde{\Gamma}_j = \tilde{\Gamma}_j (t_j) - \tilde{\Gamma}_{j-1} (t_{j-1})$ is calculated from the time sample of the flux $\tilde{\Gamma}_j (t_j)$.

[6] The processes of this kind result from the passage to the limit in a generalized Cox process [35]: the doubly stochastic Poisson process has the form $N^{(k)}(t) = N_1(\Lambda_k(t))$, where N_1 is a homogeneous Poisson process with a unit intensity and Λ_k are random processes independent of N_1.
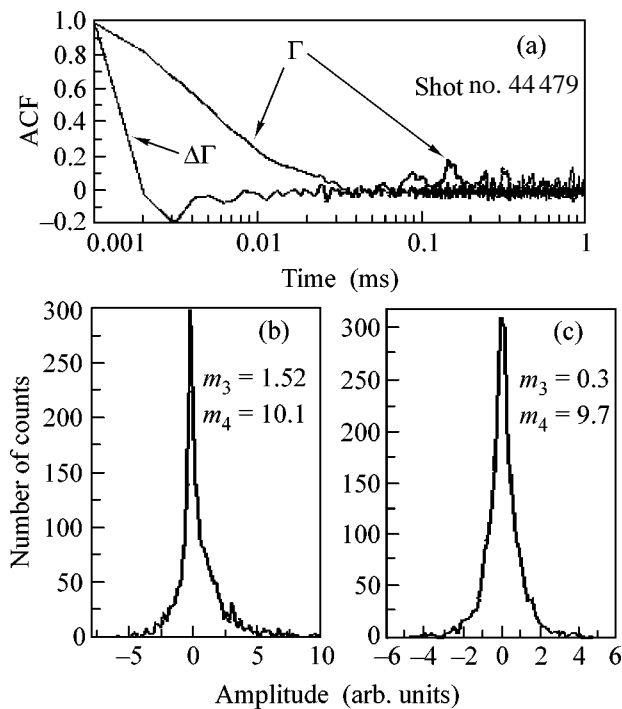
Fig. 7. (a) ACF of the flux and its increments and the PDFs of time samples of (b) the flux and (c) its increments.

ments [32, 36].[7] All of the measured probability density distributions of the density, potential, and flux fluctuations in L-2M can be classified as stable distributions [37].[8] Although the problem of analyzing the PDFs of time samples of random processes in the L-2M stellarator still remains unsolved, the determination of these PDFs can be useful. For example, it was established that the third moment (skewness) of a time sample of the turbulent flux (which characterizes the PDF asymmetry) is an indicator of the state of the stellarator chamber wall. Measurements showed that, after boronization, when the gas flux from the wall was reduced, the third moment differed from zero and did not change its sign during the discharge and the fluctuating flux was directed from the center toward the periphery throughout the entire edge plasma.

In our opinion, the analysis of the PDFs is very important for the correct interpretation of diffusion phenomena associated with turbulent fluctuations in

---

[7] The introduction of [32] is devoted to non-Gaussian probability models of random plasma-turbulence processes. It is pointed out there that, if the system under consideration is closed, then the observed PDF for a time sample of a random value is normal. In an open system affected by external factors, this is not the case; instead of a normal distribution, one can obtain a mixture of normal distributions with mixing distributions determined by the external factors.

[8] Stable distributions represent the class of the possible limiting distributions of normalized sums formed by sequences of independent and uniformly distributed random values. Note that Gaussian, Levy, Cauchy, and many other distributions can be classified as distributions of this kind.

toroidal magnetic systems. To correctly estimate the diffusion coefficient, it is necessary to analyze the stochastic differential equation including the stochastic summand described by the measured non-Gaussian PDF [38, 39]. For this purpose, it is expedient to analyze the increments of the magnitudes of turbulent fluctuations. Note that the correlation ("dynamic") time of increments is nearly one order of magnitude shorter than the correlation time of the fluctuating variables themselves. This dynamic correlation time of increments is related to the characteristic time of a stochastic plasma process. This means that the formation and decay of a stochastic plasma structure occurs nonadiabatically and is characterized by an abrupt dephasing of the fluctuating electric field and the local plasma density. It is well known that, to estimate the diffusion coefficient, it is necessary to know the characteristic decorrelation time τ_{decorr} and the characteristic spatial length Δl of the random process. Then, the diffusion coefficient can be estimated as $D \sim (\Delta l)^2/\tau_{\text{decorr}}$. Thus, the problem of estimating these quantities arises. We can assume that the decorrelation time is the time over which the cross-correlation coefficient between the fluctuations of the plasma density and the poloidal field varies and, consequently, the flux changes. In other words, this is the correlation time of the flux increments, which is a minimum characteristic time for the flux. As a characteristic spatial scale length, we can choose the maximum characteristic length, i.e., the radial scale length of the structures. Then, it can be supposed that the dynamic time and the characteristic scale length of structures determine the transport velocity across the magnetic field. Let us estimate this time for the L-2M stellarator. Assuming the characteristic length of fluctuations to be $\Delta l \sim 0.4$ cm and the dynamic time to be $\tau_{\text{decorr}} \sim 1$–2 μs, we find that the transport velocity is $(2$–$4) \times 10^5$ cm/s (which is consistent with probe measurements in the edge plasma).

4. CONCLUSIONS

(i) Steady-state low-frequency strong structural (LFSS) turbulence has been observed in a magnetized plasma of the L-2M stellarator.

(ii) Time samples of any fluctuating plasma parameters over the entire plasma volume in L-2M are bursty in character. Such time samples are more adequately described by finite-duration oscillating wavelets rapidly decaying in time (rather than infinitely long harmonic oscillations). LFSS turbulence in both the high-temperature plasma and the low-temperature edge plasma is characterized by the same spectral and correlation characteristics: wavelet spectra with quasi-harmonics and correlation functions with pulsating tails.

(iii) LFSS turbulence was observed in the L-2M stellarator throughout the plasma volume, although different mechanisms are responsible for the excitation of turbulence in different plasma regions because of the

onset of various instabilities: drift-dissipative instability, MHD resistive ballooning instability, and instability driven by trapped electrons.

(iv) A key characteristic feature of LFSS turbulence is the presence of stochastic plasma structures. The nonlinear structures comprise a considerable fraction (from 10% to 30% in different plasma regions) of the turbulence energy. The following stochastic plasma structures have been identified in LFSS turbulence observed in the L-2M stellarator: extended radial and poloidal MHD structures in the edge plasma and drift vortices at the mid-radius of the plasma column. Stochastic structures at the center of the plasma column have not been identified.

(v) High wavelet coherence (up to 50% for frequencies below 150 kHz) between time samples of the magnitudes of density fluctuations in the central region and near the plasma edge has been observed in L-2M. Turbulent fluctuations in LFSS turbulence are correlated throughout the entire plasma volume, which, probably, indicates the presence of ensembles of stochastic plasma structures.

(vi) Another characteristic feature of LFSS turbulence is that the PDF of fluctuations differs from a normal distribution by heavier tails and a larger peakedness. Stable non-Gaussian PDFs were measured for plasma density fluctuations in the central region and for the local turbulent flux in the edge plasma.

(vii) An analysis of the increments of fluctuating plasma parameters (density, potential, and turbulent flux) have allowed us to measure the dynamic times of LFSS turbulence in the L-2M stellarator.

From the aforementioned, several problems can be formulated for future investigations. How do the PDF and the characteristic correlation time of the increments of fluctuations change when one state characterized by its own macroscopic plasma parameters changes to another? What are the probabilistic parameters of local turbulence in transport barriers in toroidal magnetic systems? Do the turbulent states under study belong to systems with dynamic chaos, in which transitions can be controlled by means of weak regular waves, as is the case of a stochastic resonance regime [40]? For example, in [41], it became possible to both provoke a transformation of a wide drift-wave spectrum into a single mode and suppress the noise spectrum by applying a weak control signal. In this case, it turned out that the phase of the control signal should be adjusted in a special fashion. The problem of non-Brownian particle motion in random non-Gaussian fields is one of the very interesting and still unsolved problems of the transport theory. The same is also true of the necessity of taking into account random events when evaluating diffusion in steady-state plasmas. Finally, it should be noted that, although we considered here the features of random processes in the L-2M stellarator, similar processes are also observed in other toroidal and linear devices.

REFERENCES

1. *Proceedings of the 30th EPS Conference on Controlled Fusion and Plasma Physics, St. Petersburg, 2003*; http://eps2003.ioffe.ru/public/pdfs/.

2. J. W. Connor, P. Burraffi, J. G. Cordey, *et al.*, Plasma Phys. Controlled Fusion **41**, 693 (1999).

3. A. Yoshizawa, S.-I. Itoh, K. Itoh, and N. Yokoi, Plasma Phys. Controlled Fusion **43**, R1 (2001).

4. U. Stroth, K. Itoh, S.-I. Itoh, *et al.*, Phys. Rev. Lett. **86**, 5910 (2001).

5. A. Fujisawa, H. Iguchi, T. Minami, *et al.*, Phys. Rev. Lett. **82**, 2669 (1999).

6. N. K. Khartchev, G. M. Batanov, A. E. Petrov, *et al.*, in *Proceedings of the 30th EPS Conference on Controlled Fusion and Plasma Physics, St. Petersburg, 2003*, Paper P-3.176.

7. B. Saotic, Plasma Phys. Controlled Fusion **44**, B11 (2002).

8. G. M. Batanov, K. A. Sarksyan, A. V. Sapoznikov, *et al.*, in *Proceedings of IV International Conference on Nonlinear and Turbulent Processes in Physics, Kiev, 1989*, Vol. 1, p. 231.

9. V. V. Abrakov, A. E. Petrov, K. A. Sarksyan, and N. N. Skvortsova, Fiz. Plazmy **20**, 1069 (1994) [Plasma Phys. Rep. **20**, 959 (1994)].

10. G. M. Batanov, K. A. Sarksyan, A. E. Petrov, *et al.*, Plasma Phys. Controlled Fusion **40**, 1241 (1998).

11. D. K. Akulina *et al.*, Pis'ma Zh. Éksp. Teor. Fiz. **69**, 407 (1999) [JETP Lett. **69**, 441 (1999)].

12. N. N. Skvortsova, G. M. Batanov, L. V. Kolik, *et al.*, J. Plasma Fusion Res. **5**, 328 (2002).

13. G. M. Batanov, A. E. Petrov, K. A. Sarksyan, *et al.*, Fiz. Plazmy **29**, 395 (2003) [Plasma Phys. Rep. **29**, 363 (2003)].

14. G. M. Batanov, A. V. Sapozhnikov, K. A. Sarksyan, *et al.*, Fiz. Plazmy **12**, 1027 (1986) [Sov. J. Plasma Phys. **12**, 587 (1986)].

15. G. M. Batanov, K. M. Likin, K. A. Sarksyan, and M. G. Shats, Fiz. Plazmy **19**, 1199 (1993) [Plasma Phys. Rep. **19**, 628 (1993)].

16. G. M. Batanov, A. E. Petrov, K. A. Sarksyan, *et al.*, Pis'ma Zh. Éksp. Teor. Fiz. **67**, 634 (1998) [JETP Lett. **67**, 662 (1998)].

17. *Plasma Diagnostic Techniques*, Ed. by R. H. Huddlestone and S. L. Leonard (Academic, New York, 1965; Mir, Moscow, 1967).

18. J. Max, *Methodes et Techniques de Traitement du Signal et Applications aux Mesures Physigues* (Masson, New York, 1981; Mir, Moscow, 1983), Vols. 1, 2.

19. W. H. Press, B. P. Flannary, S. A. Teukolsky, and W. T. Vetterling, *Numerical Recipes in Pascal* (Cambridge Univ. Press, Cambridge, 1989).

20. I. Daubechies, *Ten Lectures on Wavelets* (Society for Industrial and Applied Mathematics, Philadelphia, 1992; RKhD, Moscow–Izhevsk, 2001).

21. N. M. Astaf'eva, Usp. Fiz. Nauk **166**, 1145 (1996) [Phys. Usp. **39**, 1085 (1996)].

22. B. Ph. van Milligen, E. Sanchez, T. Estrada, *et al.*, Phys. Plasmas **2**, 3017 (1995).

23. K. A. Sarksyan, N. N. Skvortsova, N. K. Kharchev, and B. F. Milligen, Fiz. Plazmy **25**, 346 (1999) [Plasma Phys. Rep. **25**, 312 (1999)].

24. N. K. Kharchev, N. N. Skvortsova, and K. A. Sarksyan, J. Math. Sci. **106**, 2691 (2001).

25. G. M. Batanov, A. E. Petrov, K. A. Sarksyan, *et al.*, Pis'ma Zh. Éksp. Teor. Fiz. **68**, 585 (1998) [JETP Lett. **68**, 585 (1998)].

26. G. M. Batanov, A. E. Petrov, K. A. Sarksyan, *et al.*, Pis'ma Zh. Éksp. Teor. Fiz. **72**, 250 (2000) [JETP Lett. **72**, 174 (2000)].

27. A. F. Aleksandrov, L. S. Bogdankevich, and A. A. Ru-khadze, *Principles of Plasma Electrodynamics* (Vysshaya Shkola, Moscow, 1978; Springer-Verlag, Berlin, 1984).

28. B. B. Kadomtsev and O. P. Pogutse, Dokl. Akad. Nauk SSSR **18**, 553 (1969).

29. L. M. Kovrizhnykh and S. V. Shchepetov, Fiz. Plazmy **7**, 419 (1981) [Sov. J. Plasma Phys. **7**, 229 (1981)].

30. A. E. Petrov, K. A. Sarksyan, N. N. Skvortsova, and N. K. Kharchev, Fiz. Plazmy **27**, 58 (2001) [Plasma Phys. Rep. **27**, 56 (2001)].

31. G. M. Batanov, V. E. Bening, V. Yu. Kordev, *et al.*, Pis'ma Zh. Éksp. Teor. Fiz. **73**, 143 (2001) [JETP Lett. **73**, 126 (2001)].

32. G. M. Batanov, A. E. Petrov, K. A. Sarksyan, *et al.*, Fiz. Plazmy **28**, 128 (2002) [Plasma Phys. Rep. **28**, 111 (2002)].

33. N. N. Skvortsova, G. M. Batanov, A. E. Petrov, *et al.*, J. Math. Sci. **112**, 4205 (2002).

34. N. N. Skvortsova, K. A. Sarksyan, and N. K. Kharchev, Pis'ma Zh. Éksp. Teor. Fiz. **70**, 203 (1999) [JETP Lett. **70**, 201 (1999)].

35. V. M. Kruglov and V. Yu. Korolev, *Limit Theorems for Random Sums* (Moscow State Univ., Moscow, 1990).

36. B. V. Gnedenko and V. Yu. Korolev, *Random Summation: Limit Theorems and Applications* (CRC, Boca Raton, 1996).

37. V. M. Zolotarev, *One-Dimensional Stable Distributions* (Nauka, Moscow, 1983).

38. M. I. Gikhman and A. V. Skorokhod, *Stochastic Differential Equations* (Naukova Dumka, Kiev, 1968; Springer-Verlag, Berlin, 1972).

39. V. I. Klyatskin, *Stochastic Equations from the Viewpoint of a Physicist* (Fizmatlit, Moscow, 2001).

40. V. S. Anishchenko, T. E. Vladislavov, and V. V. Astakhov, *Nonlinear Dynamics of Chaotic and Stochastic Systems* (Saratov State Univ., Saratov, 1999).

41. A. E. Petrov, K. A. Sarksyan, N. N. Skvortsova, and N. K. Kharchev, Fiz. Plazmy **23**, 654 (1997) [Plasma Phys. Rep. **23**, 606 (1997)].

Translated by N. Larionova

Electron Transport in Carbynes Modified under High Pressure

S. V. Demishev[1, 2], A. A. Pronin[1], V. V. Glushkov[1, 2], N. E. Sluchanko[1],
N. A. Samarin[1], M. V. Kondrin[3], A. G. Lyapin[3], V. V. Brazhkin[3],
T. D. Varfolomeeva[3], and S. V. Popova[3]

[1] *Institute of General Physics, Russian Academy of Sciences, Moscow, 119991 Russia*
e-mail: demis@lt.gpi.ru
[2] *Moscow Institute of Physics and Technology, Dolgoprudnyĭ, Moscow region, 141700 Russia*
[3] *Institute of High-Pressure Physics, Russian Academy of Sciences, Troitsk, Moscow region, 142190 Russia*
Received June 5, 2003; in final form, September 18, 2003

The studies of hopping conductivity in carbynes modified under high pressure are reviewed. Experimental data are presented on the dc and ac conductivities, thermopower, magnetoresistance, and Hall effect. The results obtained are discussed within the framework of a model that takes into account the substantially nonuniform distribution and clusterization of sp^2 bonds in the carbyne sp matrix. © 2003 MAIK "Nauka/Interperiodica".

PACS numbers: 72.20.Ee; 72.80.Le

1. INTRODUCTION

Interest in basic and applied studies of new carbon materials is, to a large extent, due to the possibility of obtaining experimental low-dimensionality systems. The boom in the field of studies of fullerenes and nanotubes, which can be considered as zero-dimensional (0D) and one-dimensional (1D) objects, respectively, serves as a striking example of this interest. Because carbon atoms in these materials are in states close to sp^2 hybridization, they are generically related to such an allotropic form of carbon as graphite. However, sp^2-bonded carbon systems are not the only possible 1D systems. An alternative approach to their creation can be based on the use of linear carbon (carbyne), which represents one of the three basic modifications of carbon and is characterized by the sp hybridization of valence electrons.

Because linear polymer chains of the polyyne $(…–C≡C–C≡C–…)$ or cumulene $(…=C=C=C=C=…)$ type constitute the basis of carbyne structure [1, 2], carbyne can be considered, at first glance, as a 1D object. However, in fact, the situation turns out to be substantially more complicated, because, as distinct from the other allotropic modifications of graphite (sp^2 hybridization) and diamond (sp^3 hybridization), carbyne cannot be obtained in the form of an ordered crystalline material. This presents evident problems in the identification of its structure. The historical difficulties in the studies of carbyne structures were so serious [1, 2] that some authors denied the very possibility of the existence of the carbyne modification of carbon. At present, however, it is established that carbyne has a "right to exist," because, at least, three theoretically and experi-

mentally justified methods for obtaining the linear form of carbon have been found to give carbynes with identical physical and chemical properties [2].

Nevertheless, the structure of carbynes remains, to a large extent, a matter of discussion. It is suggested that the disorder in carbynes is associated with the instability of large linear carbon clusters [2], as a result of which linear sp sections alternate with carbon atoms in the sp^2 state [1, 2]. The appearance of sp^2 centers first leads to a break in carbon chains and, second, creates dangling bonds that can join the neighboring chains (in the absence of sp^2 centers, the sp chains are bound to each other only by the van der Waals forces) [1, 2]. As a result, carbyne samples acquire a quasi-amorphous structure, and a complicated topology of the random network of atoms can be expected *a priori* in these materials.

Because the conventional methods of structural analysis proved to be inadequate for studying the structure of carbynes, it is of interest to use different approaches that gain information on the "interior arrangement" of these materials. In this work, this problem was solved by studying hopping transport, which is sensitive to the specific feature of the topology of the random network.

It was stated in the literature (see review [1] and references therein) that hopping conduction was observed in pure carbyne samples. Note that these statements were based on the conductivity measurements made in the temperature range $300 \, \text{K} \leq T \leq 600 \, \text{K}$, where certain activation behavior of conductivity $\sigma \sim \exp(-E_a/k_B T)$ was related to hopping [1]. It is evident that, in this case, we are dealing at best with hopping conduction
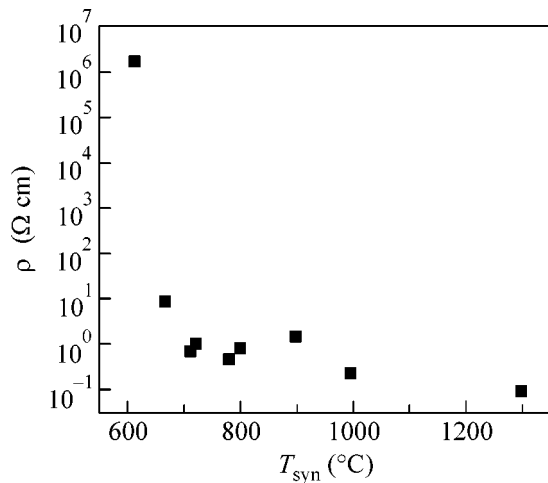
Fig. 1. Resistivity of carbine samples obtained at different T_{syn} measured at $T = 90$ K. The synthesis pressure in all cases was the same and equal to 77 GPa (according to [5]).

with a constant hopping distance [3, 4] due to tunneling between the nearest neighboring localization centers. Unfortunately, this conduction mechanism is insensitive to the topology of the random network and, therefore, is hardly suitable for obtaining independent data on the "internal arrangement" of carbynes. Moreover, an advance into the low-temperature region (where it would be possible to observe variable-range hopping conduction, which carries information on the topology of the random network) in pure carbyne samples proved to be impossible because of an extremely high resistance of the samples [1, 5].

Reliable data on variable-range hopping conduction were obtained in [5], where additional possibilities associated with exposure to high pressures and temperatures were used to control the structure and properties of carbynes. It has been found that an increase in the temperature of synthesis under pressure T_{syn} induces a growth of the concentrations of sp^2 bonds in carbyne and eventually leads to an $sp \longrightarrow sp^2$ transition, that is, to a transformation of the well-defined chainlike structure to a graphite-like disordered network [5].

An increase in the fraction of sp^2 bonds is accompanied by a decrease in the resistivity ρ of the samples. At $T \sim 90$ K, $\rho(T_{syn})$ decreases by more than seven orders of magnitude (Fig. 1), and a metal–insulator transition is observed at $T_{syn} \sim 650°C$ [5]. The samples obtained at $T_{syn} \sim 800°C$ exhibit temperature dependences of the form $\ln(\rho) \sim (T_0/T)^n$, with the exponent n close to 1/3, which is characteristic of variable-range hopping conduction.

A more detailed investigation of the hopping conduction of high-pressure-modified carbynes (HPMCs) was performed in [6–8]. In these papers, an attempt was made to connect the specific features of hopping transport with the data of structural studies. This approach

proved to be very fruitful. Not only was new information on the structure of carbynes gained with this approach, but it also provided an insight into nontrivial regimes of the hopping conduction mechanisms. In particular, it turned out that HPMCs can be presumably considered as a model system in which the conduction dimensionality could be varied experimentally from one to three (3D).

The goal of this review is to present the fullest account of the problem of hopping conduction in carbynes. At present, the list of publications on this problem is exhausted by the papers [5–9]. We supplemented the results of these papers by new data on the Hall effect and magnetoresistance. Along with the properties of HPMCs, which can be interpreted within the framework of the existing theories of hopping conduction, we will consider phenomena that have not been explained adequately so far. We will not analyze in detail the general problematics of the $sp \longrightarrow sp^2$ transition as well as other physical characteristics of carbynes not related to hopping transport. Those who are interested in this problem are referred to the reviews [1, 2, 9] and to the paper [5]. The data on the $sp \longrightarrow sp^2$ transition will be used exclusively from the viewpoint of constructing a qualitative structural model of carbynes that would be able to explain the majority of the experimental data obtained by now.

2. HOPPING CONDUCTION

In this work, as the starting material, we used carbyne with chains of the cumulene type synthesized at the Nesmeyanov Institute of Organoelement Compounds, Russian Academy of Sciences. The carbyne samples were modified according to the procedure described in [5, 9].

The temperature dependences of the resistivity obtained for HPMCs at various T_{syn} are presented in Fig. 2a in the Mott coordinates $\log(\rho) = f(T^{-n})$ [6]. It is evident that HPMCs in the range $T \leq 40$ K are characterized by variable-range hopping conduction, for which

$$\rho(T) = \rho_0 \exp[(T_0/T)^n]. \qquad (1)$$

An increase in the temperature of synthesis under pressure leads to a decrease in the hopping-conduction exponent n from $n = 1/2$ to $n = 1/4$, and $n = 1/3$ in the intermediate region of T_{syn}. In the theory of hopping conduction for a disordered system with a constant density of states $g(E_F) \approx$ const at the Fermi level, the following equation is fulfilled [3, 4, 6]:

$$n = 1/(1 + d), \qquad (2)$$

where d is the spatial dimensionality. Therefore, the result obtained can signify that the modification under pressure induced a transition from 1D ($n = 1/2$) to 2D ($n = 1/3$) and then finally to 3D ($n = 1/4$) hopping con-

duction (a detailed discussion of the applicability of Eq. 1 to the 1D case is given in [6]).

In the light of the subsequent analysis of the data, it is appropriate to raise the question of the reliability of determining the parameter n from experimental data. In the history of studying hopping conduction, this problem arose repeatedly [3, 4, 10, 11], for example, in connection with the Shklovskiĭ–Efros Coulomb gap model, for which $n = 1/2$, whereas $n = 1/4$ according to Mott. In order to solve the 1/2–1/4 dilemma, Zabrodskiĭ proposed a procedure of differentiating the $\rho(T)$ curves [10]. However, this approach is not free of criticism, because the numerical differentiation of experimental $\rho(T)$ curves requires the application of a regularization procedure, which in its turn affects the calculated value of n [10, 11]. As an alternative, it was proposed in [11] to use a procedure of the reconstruction of the temperature dependence of the resistivity $\rho(T)$ in the coordinates $\ln\ln\rho = f(\ln T)$, which is also not free from shortcomings.

At present, the controversy of the late 1970s–early 1980s on the problem of determining index n is presumably of only historical interest. With the new computational facilities and modern mathematical packages of data processing, n can be considered as a fitting parameter. For example, a direct approximation of the $\rho(T)$ data by the Levenberg–Marquardt method in the range $1.5\ \mathrm{K} \le T \le 40\ \mathrm{K}$ with the use of Eq. (1) gives the values $n = 0.49 \pm 0.05$, $n = 0.33 \pm 0.03$, and $n = 0.24 \pm 0.02$ for curves 1, 2, and 3, respectively (Fig. 2a). It is interesting that a decrease in the range limit down to $T \sim 20\ \mathrm{K}$ did not change the obtained values of n but only led to an increase in the error by 30–40%.

Because the theory of hopping conduction represents n as a rational fraction (Eq. (2)), in order to compare the theory with the experiment, the $\rho(T)$ data for HPMCs were subsequently analyzed in the coordinates $\ln\rho = f(T^{-n})$, where $n = 1/2, 1/3, 1/4$ (Fig. 2a). In order to additionally verify the accuracy of fitting index n, the values of n were fixed in the range $0.1 \le n \le 0.9$ and the dependence $\chi^2(n)$ was constructed, where χ^2 is the standard deviation of the low-temperature section of the experimental dependence $\rho(T)$ from the theoretical curve $\ln\rho = f(T^{-n})$ calculated by the least-squares method. As was to be expected, the values of n at which a minimum of $\chi^2(n)$ was reached exactly coincided with the results obtained by the Levenberg–Marquardt method. Thus, for the subsequent analysis of experimental data, the theoretical value of index n was selected in such a way that it was most close to the value obtained by numerical methods.

When the problem of accurate determination of index n is discussed, one sometimes has to deal with the statement [4] that this parameter can be determined correctly only if the temperature dependence of the prefactor ρ_0 in Eq. (1) is taken into account; in this case, it is suggested that this dependence is of power type. Note that the R–ε percolation problem or, in other words, of
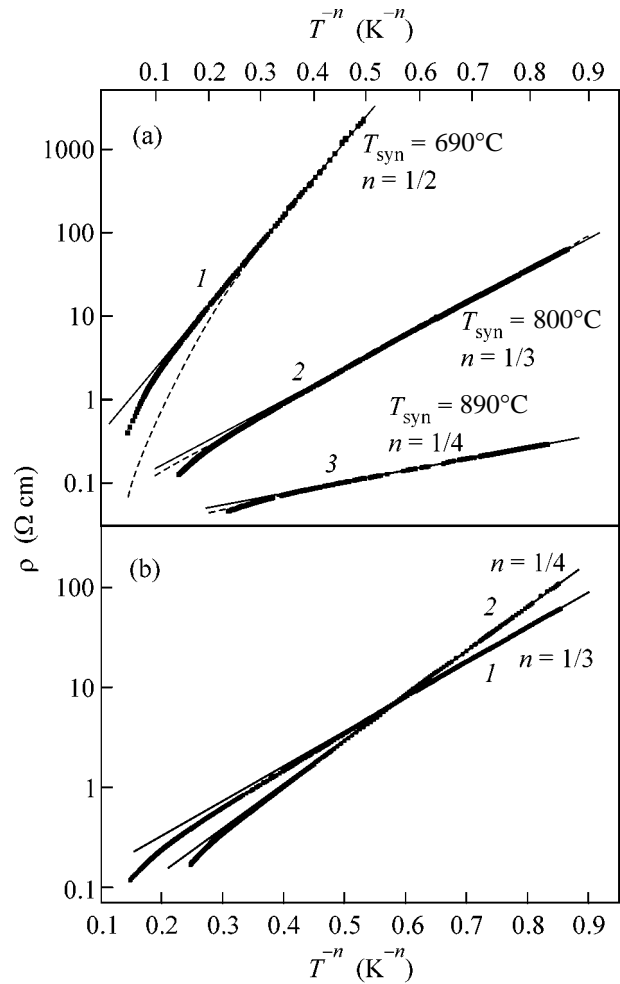

Fig. 2. (a) Temperature dependences of the resistivity of carbyne samples obtained at different synthesis temperatures (according to [6]). Points are experimental; solid lines represent the fitting of the $\rho(T)$ data for $T \le 40\ \mathrm{K}$ by Eq. (1) in the approximation $\rho_0(T) = \mathrm{const}$; dashed lines represent the fitting with regard to the power dependence of the preexponential factor $\rho_0(T) = bT^m$. (b) Relaxation of the carbyne conductivity: (1) starting sample and (2) the same sample after a yearly hold at room temperature.

variable-range hopping conduction, is solved in the theory with an exponential accuracy [4]. Therefore, the percolation approach gives no definite answer to the question of the temperature dependence of ρ_0, and, strictly speaking, it should be considered that $\rho_0 = \mathrm{const}$ in the theoretical solution to the R–ε problem (Eq. (1)). Nevertheless, several estimates are known for the possible functions $\rho_0(T)$ [3, 12, 13], including those based on the scaling theory of the metal–insulator transition [4, 13]. All these estimates give differing results that depend on additional a priori assumptions. Moreover, in the case of amorphous and quasi-amorphous materials (carbynes are among them), as distinct from doped semiconductors, it is presumably impossible to obtain a reasonable estimate for $\rho_0(T)$ from first principles [4].
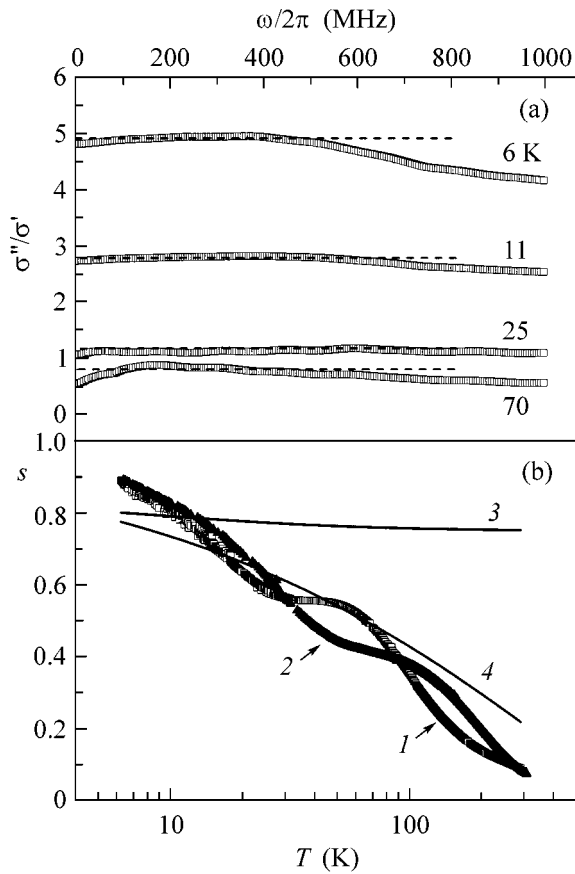
Fig. 3. AC conductivity of carbyne with $n = 1/2$. (a) Frequency dependence of σ'/σ'' at different temperatures. (b) Temperature dependence of the exponent s: (*1*), (*2*) experiment at a frequency of 100 and 500 MHz, respectively; (*3*) Coulomb gap model; (*4*) Hunt model of 1D ac conductivity (according to [6]).

The determination of n at sufficiently low temperatures for which one may neglect the possible temperature dependence of the prefactor and consider that $\rho_0 = $ const remains the only approach in this situation [4]. As follows from the above analysis, this situation arises in carbynes at $T < 40$ K.

Power corrections could be substantial at $T > 40$ K; however, in this temperature region, an additional activation contribution to the conductivity of HPMCs comes into effect (see below); this dependence is stronger than a power one. Hence, taking into account $\rho_0(T)$ in the materials under consideration goes beyond the possible accuracy.

As an illustration, along with the approximation of the $\rho(T)$ data under the assumption that $\rho_0 = $ const (solid lines), Fig. 2a displays the result of fitting with the use of Eq. (1), in which ρ_0 is given by the equation $\rho_0 = bT^m$ [3, 4, 12, 13] and index n takes the values $n = 1/2$, $n = 1/3$, and $n = 1/4$ for curves *1*, *2*, and *3*, respectively (dashed lines). It is evident that, in the cases of $n = 1/3$ and $n = 1/4$, both approaches are virtually

equivalent; however, the best agreement with the experiment is achieved only at low values of the exponent $m = -(0.01–0.08)$. These values have no physical meaning within the framework of the calculations performed in [3, 4, 12, 13]. In the case of $n = 1/2$ (Fig. 2a, curve *1*), taking into account the temperature dependence $\rho_0(T)$ considerably deteriorates the quality of the approximation of the low-temperature section of $\rho(T)$, and m increases up to $m \sim -0.6$.

Emphasize that the values of the slope of T_0^n that were determined for each curve $\rho(T)$ by different methods coincided with each other in all cases within the error of the numerical procedure (5–15%). Hence, from the viewpoint of the problems of this work, the approximation $\rho_0 = $ const proves to be sufficient. It is essential that the number of fitting parameters decreases in this case, which improves reliability of the determination of parameters n and T_0.

Thus, it may be argued that index n in HPMCs can be reliably determined, and the quality of the experimental data is sufficient for the cases of $n = 1/2$, $n = 1/3$, and $n = 1/4$ to be distinguished with confidence.

Let us return to the discussion of the value $n = 1/2$ in connection with the possibility of the experimental observation of 1D hopping conduction (Eq. (2)). This explanation of values $n > 1/2$ is not the only possible one, because a similar increase of index n can be obtained in the model of a correlation gap in the density of states [8, 9]. For example, for the case of a Coulomb gap, $n = 1/2$ in both the 2D and 3D cases. Then, based on Fig. 2a, it may be suggested that a decrease in T_{syn} from $T_{syn} \sim 800°C$ to $T_{syn} \sim 690°C$ induced the opening of a Coulomb gap at the Fermi level in the 2D system, as a result of which the parameter n increases to the value $n = 1/2$.

The choice between the two alternative approaches was made on the basis on an analysis of the frequency and temperature dependences of the ac conductivity [6]. In the hopping region, the real and imaginary parts of the conductivity, σ' and σ'', depend on the frequency as a power function $\sigma', \sigma'' \sim \omega^s$, where the exponent s can be found from the condition [4, 6]

$$s = \frac{2}{\pi}\arctan\frac{\sigma''}{\sigma'}. \qquad (3)$$

The data in Fig. 3 indicate that the ratio σ''/σ' for a sample with $n = 1/2$ is independent of the frequency over the wide range of frequencies $\omega/2\pi \leq 500$ MHz and is determined only by the sample temperature (Fig. 3a). In this case, the experimental parameter s calculated by Eq. (3) is characterized by a strong temperature dependence (Fig. 3b, curves *1* and *2*). The theoretical curve $s(T)$ can be calculated for the Coulomb gap model [4, 14] and in the Hunt model of 1D ac conduction [15–17]. It can be shown [6] that, in the first case, the exponent s weakly depends on temperature (Fig. 3b, curve *3*),

whereas the 1D model agrees well with the experimental data (Fig. 3b, curve *4*).

Based on the outline above, the conclusion was made in [6] that a change in the temperature of synthesis under pressure leads to a 1D–3D crossover in the hopping conductivity of carbynes and that the system is two-dimensional in the intermediate region.

It is natural to expect that the 2D case will be the least stable, because HPMC in this state must represent a set of 2D carbon layers that do not interact with each other. The diffusion of atoms must break such a distinctive situation, causing 2D HPMC to relax to the 3D state. The assumption made agrees well with the experiment (see Fig. 2b, which presents the temperature dependences $\rho(T)$ of the freshly prepared sample (curve *1*) and the same sample after being kept for a year at room temperature (curve *2*)). The relaxation of the samples first leads to an increase in the ratio $\rho(1.8\ \text{K})/\rho(300\ \text{K})$ and second modifies the functional dependence $\rho(T)$, as a result of which index n decreases from $n = 1/3$ to the value $n = 1/4$. This result may serve as an additional argument in favor of the interpretation of carbyne as a system with conduction of variable dimensionality.

3. THERMOPOWER

It was possible to investigate the thermopower of carbynes in the cases of $n = 1/4$ and $n = 1/3$ [8], whereas the resistivity of the samples with $n = 1/2$ was found to be too high for obtaining reliable data. It was found [8] that, in going to the hopping-conduction region, the Seebeck coefficient $S(T)$ undergoes a sign inversion (Fig. 4a). This behavior indicates that several conduction mechanisms can exist. A quantitative analysis of the temperature dependences of the conductivity $\sigma(T)$ showed that $\sigma(T)$ over the entire studied temperature range can be represented as a sum of two terms, a hopping term and an activation term,

$$\sigma(T) = \sigma_a(T) + \sigma_h(T)$$

$$= \sigma_{0a}\exp\left(-\frac{E_a}{k_B T}\right) + \sigma_{0h}\exp\left(-\left(\frac{T_0}{T}\right)^n\right). \tag{4}$$

The procedure of separating the hopping and activation contributions in HPMCs is described in detail in [8, 18, 19]. The parameters $\sigma_h(T)$ were determined in the range $T < 40$ K, that is, in the range where the contribution of $\sigma_a(T)$ or the effect of $\sigma_{0h}(T)$ is negligibly small [8]. Then, we analyzed the possible effect of the temperature dependence $\sigma_{0h}(T)$ taken from different models (see the preceding section). It proved that taking into account this factor is insufficient for the explanation of the curve $\sigma(T)$ in the temperature range $1.5\ \text{K} \le T \le 300\ \text{K}$. In this situation, it is natural to suggest that the stronger activation dependence (Eq. (4)), whose parameters σ_{0a} and E_a are determined by the condition of the best approximation of the experimental curve $\sigma(T)$, should be taken into account at higher temperatures.
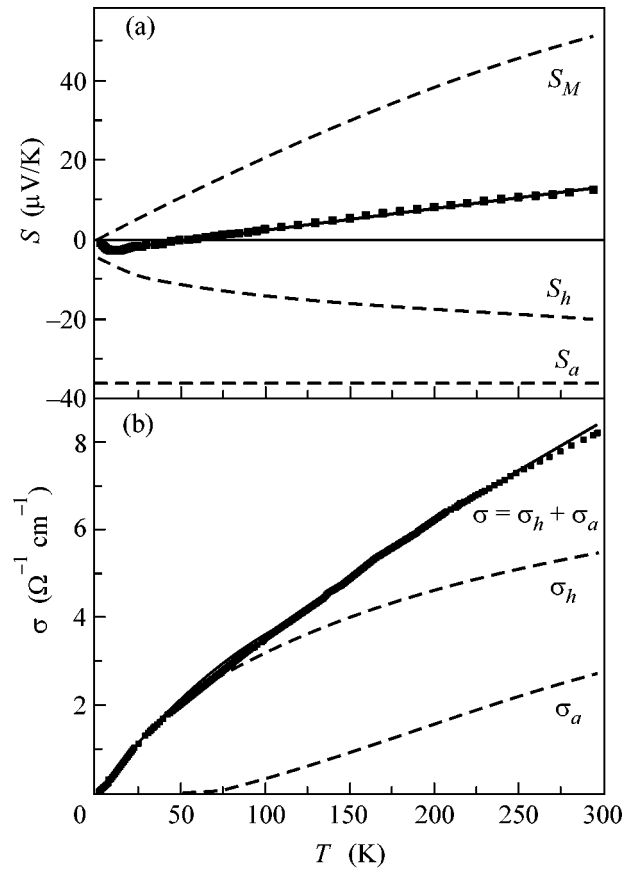
Fig. 4. (a) Carbyne thermopower with $n = 1/3$ (according to [8]). Points are experimental; line corresponds to a model calculation. Partial contributions to the integral thermopower are designated by dashed lines. (b) Separation of the carbyne conductivity into the hopping and activation contributions (designations are the same as in (a)).

The numerical procedure of approximation with two fitting parameters was stable, and the error in the determination of σ_{0a} and E_a did not exceed 5–10%.

The results of separating the contributions to the conductivity is shown in Fig. 4b. It is seen that the relationship $\sigma_a \ll \sigma_h$ is fulfilled at $T < 40$ K and that the activation contribution does not affect the determination of parameters σ_h, in particular, the exponent n. The sum $\sigma_a(T) + \sigma_h(T)$ reproduces well the shape of the curve $\sigma(T)$ over the entire investigated range of temperatures. Small deviations of the calculated curve from the experimental dependence in the range $50\ \text{K} \le T \le 100\ \text{K}$ and at $T > 250$ K can be associated with the necessity of taking into account the temperature dependences of the preexponential factors in Eq. (4).

It was found that the activation energy E_a weakly depends on the synthesis temperature T_{syn} and is of the order $E_a \sim 30$ meV [8]. Thus, the effect of T_{syn} is first reflected in the hopping conductivity σ_h, which completely agrees with the data described in the preceding section. According to these data, the temperature of
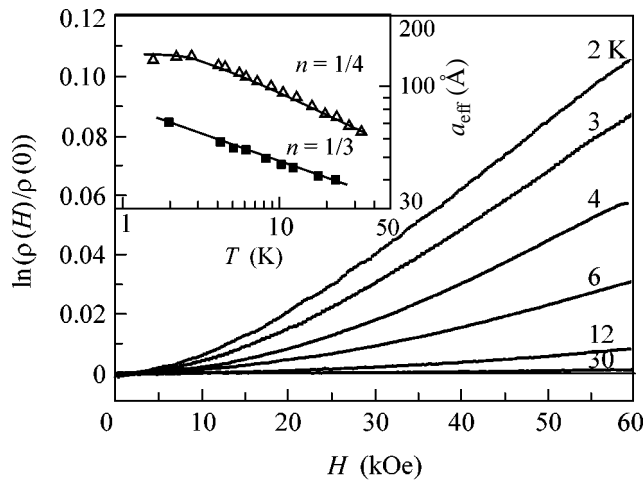
Fig. 5. Field dependences of the carbyne magnetoresistance with $n = 1/4$ at different temperatures. Inset displays the effective values of the localization radius calculated by Eq. (5).

synthesis under pressure strongly affects the topology of the random network and, hence, the character of hopping.

It can be shown [8] that the two above contributions to the conductivity are sufficient for the qualitative interpretation of the thermopower data. This problem is described in more detail in Section 6 along with the description of the corresponding model.

4. MAGNETORESISTANCE

The magnetoresistance of carbynes was reported in [7, 8], where the field dependences of the magnetoresistance were investigated at $T = 4.2$ K. It was noted that the negative magnetoresistance (NMR) is fully absent in the hopping region. In this situation, it was natural to relate the positive magnetoresistance (PMR) to the wave-function compression effect, for which the equation [3, 20]

$$\ln[\rho(H)/\rho(0)] = t_d e^2 a^4 H^2 (T_0/T)^{3n}/c^2 \hbar^2 \quad (5)$$

is fulfilled, where a is the localization radius, the parameter T_0 is the same as in Eqs. (1) and (4), and t_d is a numerical coefficient that weakly depends on the spatial dimensionality [7, 8, 20]. Using Eq. (5) and the values of T_0 determined from the $\rho(T)$ data (Fig. 2), the values of the localization radius of HPMCs $a \sim 60$–140 Å were calculated in [7, 8].

The detailed investigation of the temperature dependences of PMR in HPMCs (Fig. 5) showed that the indicated approach is only partially applicable in the hopping region. The inset in Fig. 5 displays the values of the effective localization radius calculated from Eq. (4) with the use of the relation $a_{eff} = (c^2 \hbar^2 A(T)/e^2 t_d)^{1/4} (T/T_0)^{3n/4}$, in which the coefficient $A(T) = \partial \ln \rho(H, T)/\partial H^2$ is determined by the initial quadratic section of the $\rho(H)$ curve (Fig. 5). It is clear that

the empirical localization radius obtained in this way increases by a factor of 1.5–2 with decreasing temperature from $T \sim 20$–30 K down to $T = 1.8$ K. At the same time, if Eq. (5) is true, the value of a should not depend on temperature: $a(T) \approx$ const. The latter condition was fulfilled in our experiments only for the 3D sample with $n = 1/4$ and only in the temperature region $T \le 3$ K (inset in Fig. 5). Nevertheless, if the obtained values of a are used as estimates, one should expect sufficiently large values of the localization radius in HPMCs, comprising at least several tens of angstroms (Fig. 5).

It is interesting that Eq. (5) follows from a consideration of the elementary magnetocoulombic problem in the case of a weak magnetic field [3, 20], for which the first magnetosensitive correction to the resistance of the Miller–Abrahams network is proportional to aR^3/l_H^4, where R and l_H are the hopping distance and the magnetic length, respectively. Therefore, relationship (5) must be of sufficiently general character and should not depend on a certain mechanism of jumps. In this connection, the reasons for the violation of the applicability of Eq. (5) in carbynes remain unclear and call for an additional theoretical study. A possible hypothesis of the nature of this anomalous behavior is discussed in Section 6.

5. HALL EFFECT

Measurements of the Hall effect in the hopping region represent one of the most complicated experimental tasks, which is associated with the necessity of measuring small Hall voltages across a high-resistivity sample [21]. Therefore, at present, reliable data on the Hall effect in HPMCs have been obtained only for the case $n = 1/4$. It was found that, in such samples, the Hall coefficients $R(T)$ corresponds to a p-type material and increases with decreasing temperature (Fig. 6a). It is interesting that, as distinct from thermopower, the sign inversion of the Hall coefficient does not occur in going to the hopping region. The fact that HPMCs are characterized by high values of the Hall concentration $n_H = 1/Re$, reaching $n_H \sim 3.7 \times 10^{19}$ cm^{-3} at $T \sim 200$ K (Fig. 6a), attracts attention.

It is interesting that the Hall coefficient in the hopping region $T < 40$ K varies according to the law $\ln R \sim (T_0^*/T)^{1/4}$, which is analogous to the temperature dependence of resistivity (Fig. 5b). However, the quantities T_0^* and T_0, which determine the slope of the linear portions of the curves $\log R = f(T)^{-1/4}$ and $\log \rho = f(T)^{-1/4}$, correspondingly turn out to be different (Fig. 6b), and the measured ratio of slopes equals $(T_0^*/T)^{1/4} \approx 0.8$.

It should be emphasized that we do not know any other experimental papers in which the temperature dependence of $R(T)$ is observed in the region of variable-range hopping conduction. The only publication
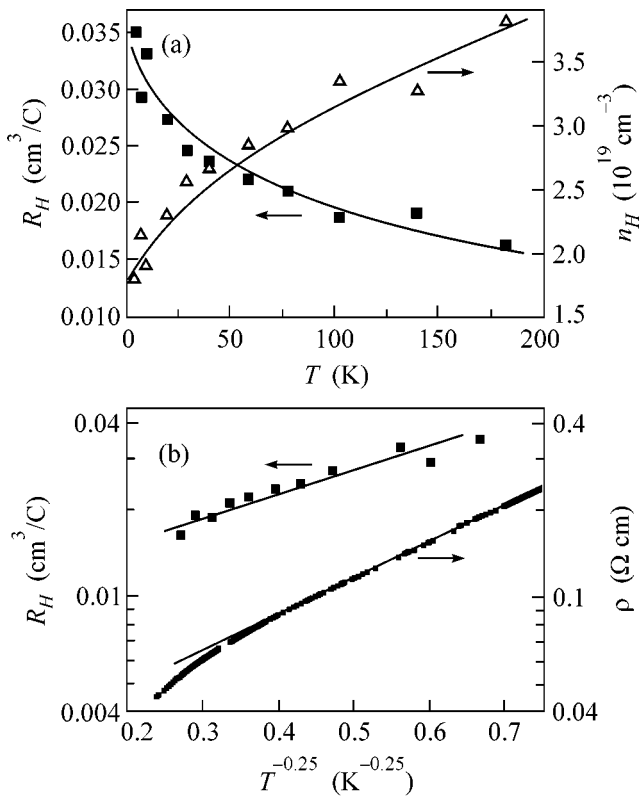
Fig. 6. (a) Temperature dependences of the Hall coefficient and Hall concentration for carbyne with $n = 1/4$. (b) Hall coefficient and resistivity in the region of Mott's hopping conduction.

Fig. 7. (a) Model of the carbyne structure; R_{ij} designates the hopping distance between the localized states of radius a; (b) effective medium model used to describe the thermopower; (c) energy diagram illustrating conduction mechanisms in carbynes. D^0 and D^- designate the lower and upper Hubbard bands, respectively.

on this question [21] reports that $R(T) \approx$ const in the region of Mott's law action.

At the same time, the temperature dependence of the Mott type was predicted for the Hall coefficient in [22, 23]. According to these papers, the parameter T_0^* must be smaller than T_0. It is expected that the quantity $(T_0^*/T_0)^{1/4}$ must comprise $5/8 = 0.625$ [22, 23], which is somewhat lower than the value observed experimentally. It is likely that this discrepancy is a consequence of the approximate character of calculations in [22, 23] and can be overcome in the course of the subsequent development of the theory of the hopping Hall effect.

6. MODEL OF THE STRUCTURE AND HOPPING CONDUCTION OF CARBYNES

As was already mentioned above, the x-ray spectra of HPMCs correspond to a quasi-amorphous material. In this situation, the most reliable structural parameter that can be determined experimentally is the correlation length L_{cor}. This correlation length determines the characteristic size of the ordered carbon chain of the cumulene type $\dots=C=C=C=\dots$. Because carbon atoms in the sp^2 state presumably play the role of the main structural defects that determine the bend of carbon chains in the
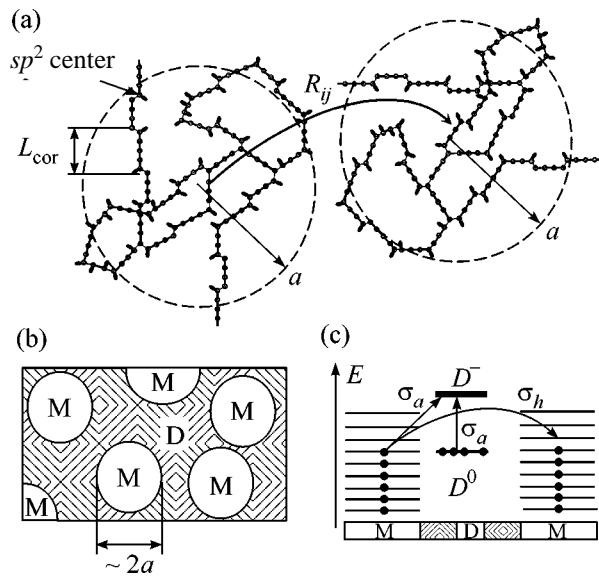
carbyne matrix [1, 2, 5, 9], the concentration of sp^2 centers can be estimated from the relation $N_{sp^2} \sim L_{cor}^{-3} \sim 10^{21}$ cm^{-3}.

It was found that the parameter L_{cor} only weakly depends on the synthesis temperature in the range $690°C \le T_{syn} \le 890°C$ and comprises $L_{cor} \sim 10–12$ Å. At the same time, from the previous investigations, it follows that an increase in T_{syn} leads to an increase in the concentration of sp^2 centers and eventually to an $sp \longrightarrow sp^2$ transition. The concept of the $sp \longrightarrow sp^2$ transition can be reconciled with the constancy of L_{cor} if it is assumed that the new sp^2 centers arising in the synthesis under pressure will be formed in the vicinity of the already present defects, for example, because of the fact that the activation energy of the creation of the second sp^2 center beside an already present one proves to be lower than the activation energy of the creation of a single sp^2 center inside an sp chain. Such pairs of neighboring sp^2 centers will lead not only to a break in certain chains but also to the formation of closed ring structures, which can effectively localize electrons (Fig. 7a). As a result, we come to the following model proposed in [8].

If the concentration of sp^2 bonds in the sample is small (low synthesis temperatures), quasi-linear chains of carbon atoms in the sp state (containing only a small number of sp^2 centers) will connect regions of more complicated topology characterized by an increased fraction of sp^2 centers (sp "string" of sp^2 "beads"). Con-

duction in such a system will be carried out by means of hops between clusters with an increased concentration of sp^2 centers (Fig. 7a). In the case when the interaction between such nonuniform chains can be neglected, the conduction of this system will be of a quasi-one-dimensional character. It is evident that an increase in the fraction of sp^2 bonds with increasing T_{syn} will lead to the appearance of interchain interaction and to an increase of the effective dimensionality of conduction first to 2D and then to 3D.

Based on the data on the Hall effect (Section 5), one more important assumption of the properties of localized states in carbynes can be made. It is evident that the consideration of the hopping mechanism loses its meaning in the high-temperature region and the sample can be described in the effective medium limit. Then, the Hall concentration can be used to estimate the volume-average electron concentration. In the case of the activation dependence of conduction of any type, the electron concentration and, hence, the Hall concentration will decrease with decreasing temperature. Therefore, the high-temperature values of n_H (Fig. 6) can be considered as the lower estimate of the total electron concentration in the sample. As a result, using estimates of the localization radius (Section 4), we come to the conclusion that the fulfillment of the condition $4/3\pi a^3 \times (N_{sp^2}, n_H) \gg 1$ should be expected in HPMCs. That is, many partially occupied electronic levels must occur inside the electron localization region (at least, this must certainly be fulfilled for the 3D samples with $n = 1/4$). An analogous result can also be obtained for 2D and 1D samples if estimates of the density of localized states are used (a detailed discussion of this question is given in [8]).

Presumably, the anomalies of magnetoresistance in the hopping region can be associated with the considered property of localized states in carbynes. It is well-known that both the wave-function compression effects and the quantum interference effects make a contribution to magnetoresistance in the general case [3, 20]. As a rule, quantum interference predominates in the region of weak magnetic fields and is responsible for NMR, and PMR associated with the shrinkage effect arises in the region of stronger magnetic fields [11, 20, 24]. In the case of HPMCs, the character of quantum interference can change substantially. Actually, the cylindrical volume connecting localized states i and j spaced at the hopping distance R_{ij} will contain $\pi a^2 R_{ij}/L_{cor}^3 \sim \pi a^3 (T_0/T)^n/L_{cor}^3$ centers at which quantum interference can arise. For $T = 4.2$ K, the number of such scattering centers will be on the order of 1.2×10^3, whereas the number of centers in usual materials that are significant from the viewpoint of interference effects does not exceed several dozen.

Suppose that the change in the interference character will lead to the fact that the interference contribution

will be quadratic in the magnetic field in the same region of magnetic fields as the contribution associated with the wave-function compression effects. Then instead of Eq. (5), we may write

$$\ln\frac{\rho(H)}{\rho(0)} = c\left[a^4\left(\frac{T_0}{T}\right)^{3n} + f(T)\right]H^2, \tag{6}$$

where c is a numerical coefficient, and function $f(T)$ takes into account the quantum interference effects. Hence, the effective localization radius (inset in Fig. 5) will be determined by the relation

$$a_{eff} = \left[a^4 + f(T)\left(\frac{T}{T_0}\right)^{3n}\right]^{1/4}. \tag{7}$$

Then, the data in Fig. 5, including the saturation of a_{eff} at $T < 3$ K, can be explained assuming that $f(T)T^{3n} \longrightarrow 0$ at $T \longrightarrow 0$ and, in addition, $f(T) < 0$. The negative sign of $f(T)$ corresponds to the NMR effect as in the usual materials with hopping conduction; however, it is necessary to admit a significant modification of the field dependence of the contribution due to quantum interference in order to explain the magnetoresistance in HPMCs. The verification of this assumption can be performed when the corresponding theoretical investigations are performed.

As an additional argument in favor of the complicated structure of localized states in HPMCs, consider a model of the quantitative analysis of the thermopower. Following [8], consider HPMC in the effective medium model (Fig. 7b), in which the "metallic" regions (M) correspond to the regions of localization with an excessive concentration of electrons and sp^2 bonds and the "dielectric" regions (D) correspond to the sp matrix. The conductivity of such a medium will be determined by the dielectric regions, whereas metallic regions can also contribute to $S(T)$. In this case, $S_M(T)$ for the "metal" will be described by the generalized Mott equation [18, 19] $S_M(T) = aT + bT^3$. As follows from Fig. 4, two contributions should be taken into account in the thermopower of a dielectric $S_D(T)$, the hopping one $S_h \sim T^{1-2n}$ [4, 8] and the activated one S_a, summed with the weights $\sigma_h/(\sigma_h + \sigma_a)$ and $\sigma_a/(\sigma_h + \sigma_a)$ [8]. The detailed analysis made in [8] showed that σ_a in HPMCs is presumably determined by activation to the upper Hubbard zone D^- (see Fig. 7c), as a result of which S_a = const. An example of the separation of contributions to the thermopower is given in Fig. 4a: it is evident that the indicated procedure reproduces well the shape of the integral $S(T)$ curve. In addition, it can be shown [8] that the "metal" thermopower is positive in all the studied samples ($S_M(T) > 0$), whereas the "dielectric" thermopower is negative, which causes the sign inversion in the dependence $S(T)$ (Fig. 4a).

It is interesting that the thermopower sign inversion in the model under consideration is not associated with the change of sign in the major current carriers, but

reflects the specific properties of the electronic states of carbynes [8]. Actually, the states inside the localization region must be almost completely occupied; therefore, it is natural to expect that conduction of "metal" would be of the hole type ($S_M(T) > 0$). The negative sign of S_D, first, arises by virtue of the condition $\partial g(E_F)/\partial \varepsilon < 0$ (the negativity of the hoping contribution, $S_h < 0$) and, second, is a consequence of the fact that the occupation numbers of localized states are of the order of unity ($S_a < 0$) [8]. As a result, it becomes possible to explain simultaneously the thermopower sign inversion and the absence of sign inversion in the Hall effect.

7. CONCLUSION

Thus, we have shown that an adequate understanding of hopping transport in carbynes can be obtained within the framework of the model that takes into account the substantially nonuniform distribution of sp^2 bonds on the nanometer scale. It is nontrivial here that the classical theory of hopping conduction adequately describes the majority of experimental data, in spite of the complicated structure of the localization region. At the same time, the existing theories of magnetoresistance and hopping Hall effect are evidently incomplete and insufficient to describe adequately experimental data. Note that attempts have been made recently to create a consistent theory of hopping transport for the case of localized states inside which there are a number of energy levels [25, 26]. It is possible that better description of the physical properties of carbynes will be obtained in the future within the framework of this approach, including the properties of PMR that have not been understood by now. However, at present, the indicated calculations have not reached the level such that the whole set of experimental data obtained in this work could be compared with theoretical predictions.

REFERENCES

1. Yu. P. Kudryavtsev, S. E. Evsyukov, B. M. Guseva, *et al.*, Izv. Ross. Akad. Nauk, Ser. Khim. **3**, 450 (1993).

2. B. M. Bulychev and I. A. Udod, Ros. Khim. Zh. **39**, 9 (1995).

3. B. I. Shklovskiĭ and A. L. Éfros, *Electronic Properties of Doped Semiconductors* (Nauka, Moscow, 1979; Springer, New York, 1984).

4. I. P. Zvyagin, *Kinetic Phenomena in Disordered Semiconductors* (Mosk. Gos. Univ., Moscow, 1984).

5. A. G. Lyapin, V. V. Brazhkin, S. G. Lyapin, *et al.*, Phys. Status Solidi B **211**, 401 (1999).

6. S. V. Demishev, A. A. Pronin, N. E. Sluchanko, *et al.*, Pis'ma Zh. Éksp. Teor. Fiz. **72**, 547 (2000) [JETP Lett. **72**, 381 (2000)].

7. S. V. Demishev, A. A. Pronin, N. E. Sluchanko, *et al.*, Fiz. Tverd. Tela (St. Petersburg) **44**, 585 (2002) [Phys. Solid State **44**, 607 (2002)].

8. S. V. Demishev, A. A. Pronin, V. V. Glushkov, *et al.*, Zh. Éksp. Teor. Fiz. **122**, 140 (2002) [JETP **95**, 123 (2002)].

9. V. V. Brazhkin, A. G. Lyapin, S. V. Popova, *et al.*, Pis'ma Zh. Éksp. Teor. Fiz. **76**, 805 (2002) [JETP Lett. **76**, 681 (2002)].

10. A. G. Zabrodskiĭ, Fiz. Tekh. Poluprovodn. (Leningrad) **14**, 1324 (1980) [Sov. Phys. Semicond. **14**, 781 (1980)].

11. N. B. Brandt, S. V. Demishev, A. A. Dmitriev, *et al.*, Zh. Éksp. Teor. Fiz. **86**, 1446 (1984) [Sov. Phys. JETP **59**, 847 (1984)].

12. N. F. Mott and E. A. Davis, *Electronic Processes in Non-Crystalline Materials*, 2nd ed. (Clarendon Press, Oxford, 1979; Mir, Moscow, 1982).

13. S. V. Demishev, Yu. V. Kosichkin, N. E. Sluchanko, and A. G. Lyapin, Usp. Fiz. Nauk **164**, 195 (1994) [Phys. Usp. **37**, 185 (1994)].

14. B. I. Shklovskiĭ and A. L. Éfros, in *Proceedings of All-Union Conference on the Physics of Semiconductors* (ÉLM, Baku, 1982), Vol. 1, p. 65.

15. A. Hunt, Solid State Commun. **86**, 765 (1993).

16. A. Hunt, in *Proceedings of the 5th International Conference on Hopping and Related Phenomena*, Ed. by C. J. Adkins, A. R. Long, and J. A. McInnes (World Sci., Singapore, 1994), p. 65.

17. A. G. Hunt, Philos. Mag. **81**, 875 (2001).

18. S. V. Demishev, M. V. Kondrin, A. A. Pronin, *et al.*, Pis'ma Zh. Éksp. Teor. Fiz. **68**, 801 (1998) [JETP Lett. **68**, 842 (1998)].

19. S. V. Demishev, A. A. Pronin, M. V. Kondrin, *et al.*, Phys. Status Solidi B **218**, 67 (2000).

20. M. E. Raikh, J. Czingon, Qiu-yi Ye, *et al.*, Phys. Rev. B **45**, 6015 (1992).

21. S. V. Demishev, in *Proceedings of the 5th International Conference on Hopping and Related Phenomena*, Ed. by C. J. Adkins, A. R. Long, and J. A. McInnes (World Sci., Singapore, 1994), p. 179.

22. M. Gruenewald, H. Mueller, P. Thomas, and D. Wuertz, Solid State Commun. **38**, 1011 (1981).

23. M. Gruenewald, H. Mueller, and D. Wuertz, Solid State Commun. **43**, 419 (1982).

24. S. V. Demishev, D. G. Lunts, A. G. Lyapin, *et al.*, Zh. Éksp. Teor. Fiz. **110**, 334 (1996) [JETP **83**, 180 (1996)].

25. I. P. Zvyagin and R. Keiper, Phys. Status Solidi B **230**, 151 (2002).

26. I. P. Zvyagin and R. Keiper, Philos. Mag. **81**, 997 (2001).

Translated by A. Bagatur'yants